Domain walls shift gears : novel ways to control magnetic domain-wall motion

Domain walls shift gears

Novel ways to control magnetic domain-wall motion

PROEFSCHRIFT

ter verkrijging van de graad van doctor aan de
Technische Universiteit Eindhoven, op gezag van de
rector magnificus prof.dr.ir. C.J. van Duijn, voor een
commissie aangewezen door het College voor
Promoties in het openbaar te verdedigen
op donderdag 20 maart 2014 om 16.00 uur

door

Jeroen Hendrik Franken

geboren te Roosendaal en Nispen

Dit proefschrift is goedgekeurd door de promotoren en de samenstelling van de promotiecommissie is als volgt:

voorzitter:	prof.dr.ir. G.M.W. Kroesen
1e promotor:	prof.dr.ir. H.J.M. Swagten
2e promotor:	prof.dr. B. Koopmans
leden:	prof.dr. S.S.P. Parkin (IBM Almaden Research Center)
	dr. A. Thiaville (Université Paris-sud)
	prof.dr.ir. B.J. van Wees (RUG)
	dr. R.A. Duine (UU)
	prof.dr.ir. O.J. Luiten

Domain walls shift gears

Novel ways to control magnetic domain-wall motion

Jeroen Franken

The cover shows an assortment of toys, to illustrate the playful experiments of this thesis. Shown on the top is a primitive digital audio storage medium by Fisher-Price® dating back to 1971. Its appearance resembles a modern-day magnetic hard-disk drive, to which a follow-up technology is investigated in this thesis. Also shown is a ratchet, quite similar to the nano-magnetic variety introduced in Chapter 3. The title and some random technical terms are laid out in Scrabble tiles, one of the favorite board games of the author.

A catalogue record is available from the Eindhoven University of Technology Library.
ISBN: 978-90-386-3572-9

This work is part of the research programme of the Foundation for Fundamental Research on Matter (FOM), which is part of the Netherlands Organisation for Scientific Research (NWO).

Printed by Ipskamp Drukkers B.V., Enschede.

Contents

1 Introduction **1**
- 1.1 Spintronics . . . 1
- 1.2 Racetrack memory . . . 2
- 1.3 Magnetic domain walls . . . 2
- 1.4 Domain-wall motion . . . 4
- 1.5 This thesis . . . 5

Part I Controlling domain-wall pinning **9**

2 Introduction to domain-wall pinning by anisotropy modification **11**
- 2.1 Introduction . . . 11
- 2.2 Basic micromagnetic theory . . . 13
- 2.3 1D model of DW pinning . . . 16
- 2.4 Experimental toolbox . . . 21
- 2.5 Manipulating the anisotropy of Pt/Co/Pt . . . 26
- 2.6 Controlling domain-wall nucleation and pinning . . . 29
- 2.7 Conclusion . . . 36
- 2.8 In this Part . . . 37

3 Field-driven domain-wall ratchet memory **39**
- 3.1 Introduction . . . 39
- 3.2 Experimental demonstration . . . 41
- 3.3 Performance statistics . . . 42
- 3.4 Conclusion . . . 44
- 3.5 Methods . . . 45

4 Tunable domain-wall oscillator at an anisotropy boundary **47**
- 4.1 Introduction . . . 47
- 4.2 1D model . . . 49
- 4.3 Micromagnetic simulations . . . 52
- 4.4 Discussion & conclusion . . . 52

5 Voltage-gated domain-wall pinning 55
5.1 Introduction . . . 55
5.2 Experimental design . . . 56
5.3 Experimental results . . . 57
5.4 Discussion . . . 58
5.5 Conclusion . . . 61

6 Beam-induced Fe nanopillars as tunable domain-wall pinning sites 63
6.1 Introduction . . . 63
6.2 Imaging stray fields of magnetic pillars . . . 64
6.3 Stray-field induced pinning . . . 65
6.4 Probing the coercive field of pillars . . . 69
6.5 Conclusion & outlook . . . 71
6.6 Methods . . . 72

Part II Current-induced effects 73

7 Introducing current-induced effects 75
7.1 Conventional spin-transfer-torques . . . 75
7.2 Spin-orbit torques . . . 79
7.3 Dzyaloshinskii-Moriya interaction . . . 85
7.4 In this Part . . . 87

8 Measuring the resistivity of individual magnetic domain walls 89
8.1 Introduction . . . 89
8.2 Experimental procedure . . . 90
8.3 Results & discussion . . . 92
8.4 Conclusion . . . 95

9 Domain-wall depinning governed by the spin Hall effect 97
9.1 Introduction . . . 97
9.2 The spin Hall effect in Pt/Co/Pt . . . 98
9.3 Spin Hall torque on domain walls . . . 99
9.4 Experimental demonstration . . . 100
9.5 Role of stack composition . . . 103
9.6 Conclusion & outlook . . . 103
9.7 Methods . . . 104

10 Tunable chiral spin texture in magnetic domain walls 105
10.1 Introduction . . . 105
10.2 Effect of chiral field on DW depinning . . . 106
10.3 Probing the DW structure by DW resistance . . . 108
10.4 Discussion & conclusion . . . 111
10.5 Methods . . . 111

Conclusion & outlook 113

A Supplementary information on Chapter 6 **115**
A.1 Stray field calculation 115
A.2 Coercive field calculation 116

B Supplementary information on Chapter 9 **119**
B.1 Predicted ϵ from the nonadiabatic torque 119
B.2 Pinning field as a function of in-plane field 119
B.3 Micromagnetic simulations 120
B.4 Magnitude of Rashba contributions 122
B.5 Magnetization reversal of $(4,2)$ and $(2,4)$ stacks 124

C Supplementary information on Chapter 10 **125**
C.1 Material parameters 125
C.2 DW resistance model 127

Summary **131**

Curriculum vitae **133**

List of publications **135**

Dankwoord **137**

Bibliography **139**

Introduction 1

This thesis describes research on the topic of magnetic domain-wall motion. Here, we will provide a motivation for the work performed. We will start with a very brief introduction to the field of spintronics, after which racetrack memory is introduced, a computer memory concept that makes use of domain-wall motion. We will identify some important challenges in this research field, and define the main aims of this thesis: to obtain a better control and understanding of domain-wall motion in perpendicularly magnetized materials.

1.1 Spintronics

During the course of the last century, people have become increasingly dependent on electronic devices. Although the incredible functionality of modern electronics sometimes looks like magic, most people will have a basic notion that it relates to the flow of electric *charge*, and some of us are aware that this charge is carried by *electrons*.

In addition to their charge, electrons have another, much lesser-known property. In 1926, Dutch scientists Uhlenbeck and Goudsmit [1] suggested the existence of a quantum-mechanical phenomenon called *spin*. It represents an intrinsic contribution to angular momentum, in addition to the orbital angular momentum that had been known before. Orbital angular momentum is easily visualized by an electron orbiting around a nucleus, but spin is a purely quantum-mechanical phenomenon that does not have a valid classical analog, although it is often visualized as the spinning motion of an electron around it own axis. It is easy to see from elementary physics that a rotating charge gives rise to a magnetic field, and spin similarly gives rise to an intrinsic magnetic moment. This is the reason why some materials show permanent magnetic behavior. Magnetic materials are ideal for storing data, since the magnetic ordering is stable enough to preserve data for a long time, but is also changeable by an external magnetic field. This has been employed for a long time in applications like audio tapes, floppy disks, and hard disk drives (HDDs).

More recently, it was realized that spin provides a very useful additional degree of freedom in electronic devices. The discovery of the Giant Magnetoresistance

(GMR) effect in 1988 [2,3], is often considered to be the birth of a new research field: *spintronics*. The GMR effect corresponds to a strong change of the electrical resistance of a magnetic bilayer, when the relative magnetizatic orientation of the two layers is changed. This resistance change occurs because the current becomes *spin-polarized* in the first magnetic layer, since the electrons with different spin orientations experience a different resistance. The polarized current subsequently experiences a higher resistance in the second layer if it is oppositely oriented. The strength of this effect turned out to be large enough for sensing magnetic bits in HDDs, and has enabled a tremendous increase of the storage density in these devices, simply because of the improved sensitivity.

The GMR effect describes how the magnetization direction influences current flow, but like in many physical phenomena, the inverse effect also exists. Berger [4,5] and Slonczewski [6] were the first to mention *spin-transfer torque* (STT), the effect in which a spin-polarized current exerts a torque on the magnetization. This leads to endless possibilities for new spintronics devices, in particular relating to data storage. Spin-transfer torque also inspired a radically new data storage mechanism that forms the motivation for this thesis: *racetrack memory*.

1.2 Racetrack memory

Racetrack memory is a device concept proposed by Parkin *et al.* at IBM research [7]. The main idea is to combine the low cost and non-volatility of the magnetic HDD that is nowadays used for bulk storage, with the speed of RAM memory, hence creating a universal memory. Additionally, the device eliminates the need for unreliable mechanical rotation which plagues current HDDs, and could even make use of the vertical dimension to store much more data on the same area. The key ingredient to this visionary idea is to store a pattern of many magnetic 'bits' in a single tiny magnetic nanostrip, as visualized in Figure 1.1(a). When this information needs to be accessed, the whole pattern is rapidly shifted through the strip past a central read/write position. This way, a single read/write element is required to process many bits, in contrast to alternatives like flash memory and MRAM. If it is possible to grow these nanostrips in the vertical dimension (Figure 1.1(b)), a multitude of the information can be stored on the same area, compared to any other storage device. By fabricating an array of such nanostrips, a large data storage volume is realized as shown in Figure 1.1(e). Of course, the crucial challenge is to shift this pattern in a fast but controllable way without loosing information, and this is where the STT effect comes in. By sending current pulses through the nanostrip, the magnetic pattern turns out to be moved. Thanks to this inspiring idea and the intriguing physics that govern it, a new and highly competitive research field has spawned, to which this thesis makes several contributions.

1.3 Magnetic domain walls

Before we elaborate on the inner workings of racetrack memory, let us describe how data is represented in a conventional HDD. Modern HDDs use thin platters of magnetic material in which the direction of the magnetization has two preferential directions: either pointing 'up' or 'down'. This bistable character makes them ideal

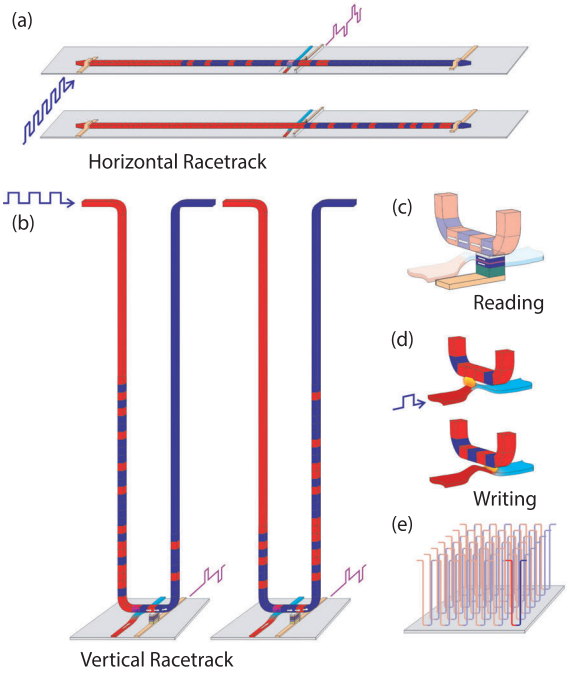

Figure 1.1 | The racetrack memory concept. (a) Horizontal racetrack. (b) Vertical racetrack. (c) Data readout using a magnetic tunnel junction. (d) A possible bit writing scheme involving the stray field of a DW moving in a secondary nanostrip. (e) An array of vertical racetracks packed on a chip. From [7].

to represent binary data. The data is represented by alternating 'up' and 'down' regions, and such regions are called *magnetic domains* and can be as small as a few tens of nanometers. It is not trivial that the magnetization points perpendicular to the plane; in fact, the magnetization in a thin film is normally oriented in-plane. However, if the film is made ultrathin ($\sim$ 1 nm), interface interactions can lead to strong *perpendicular magnetic anisotropy* (PMA), which means it is energetically favorable for the magnetization to point out-of-plane within the domains.

In racetrack memory, the crucial physics does not take place in these domains, but rather at the boundaries that separate them from each other, which are called *domain walls* (DWs). It turns out that moving these DWs is the way to transport the data through our tiny nanostrips. Although much of the early work on DW motion focused on in-plane magnetized nanostrips [8], the use of PMA materials is very promising. One of the main reasons is that a stronger anisotropy leads to smaller DWs, hence the spacing between two bits can be reduced.

DWs in PMA materials come in two shapes, the Bloch wall and the Néel wall illustrated in Figure 1.2. For now, the precise shape of the DW does not matter and the take-away message is that the magnetization rotates from the 'up' to the 'down' direction within the DW, over a length of only a few nm, which is called the *DW*

width. Interestingly, at the end of this thesis we will show that the shape of the DW crucially affects the speed at which they can be moved.

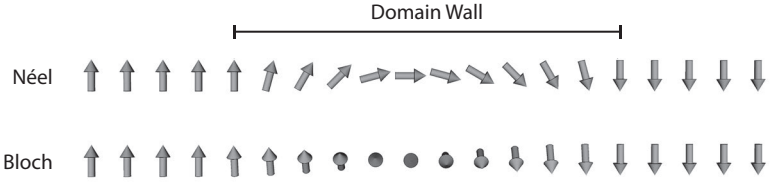

Figure 1.2 | Schematic illustration of the two relevant DW types, Néel and Bloch, which have a different internal orientation.

1.4 Domain-wall motion

Since racetrack memory relies on the motion of magnetic DWs, a reliable way to achieve this is required. The most obvious way to move DWs, is by applying a magnetic field. The field exerts a torque on the DWs such that they start to move. However, since the magnetic domains expand in order to align with the applied field, two neighboring DWs will move in opposite directions. This eventually erases all the data that is stored in the strip. Hence, a mechanism is required that moves all DWs *coherently* through the nanostrip, and the STT provides such a mechanism. Since a current becomes spin-polarized in the magnetic direction of the ferromagnet, the polarization of the current flips when a DW is encountered. Because of angular momentum conservation, this change of angular momentum of the conduction electrons leads to a reaction torque on the DWs called *adiabatic STT*. The result is that DWs are pushed coherently in the direction of electron flow, as illustrated in Figure 1.3(a). In addition to this torque, a second, *nonadiabatic* torque was identified [9,10] in order to explain early experimental results [11–16]. Although its physical origin remains controversial to this day [9,10,17], the common interpretation of this torque is that the spin polarization of the electric current cannot completely follow the local magnetization within the DW, and a misalignment between the current and DW spins occurs, which acts as an additional field-like torque on the magnetization (see Figure 1.3(b)). PMA materials have very narrow DWs, hence this misalignment and its associated torque could be larger, which is one of the reasons that these materials are promising for current-induced DW motion.
Although current-induced DW motion was indeed observed [7,13,14,16,18–20], there are still many challenges that have to be met to achieve a reliable racetrack memory. At the risk of oversimplification, the following problems can be identified:

- Very challenging *3D structuring* to make it run vertically. This is not the subject of this thesis, since we focus only on planar nanostrips. It should be noted that even a planar version of racetrack memory has numerous advantages, although it does not increase the storage density compared to a conventional HDD.

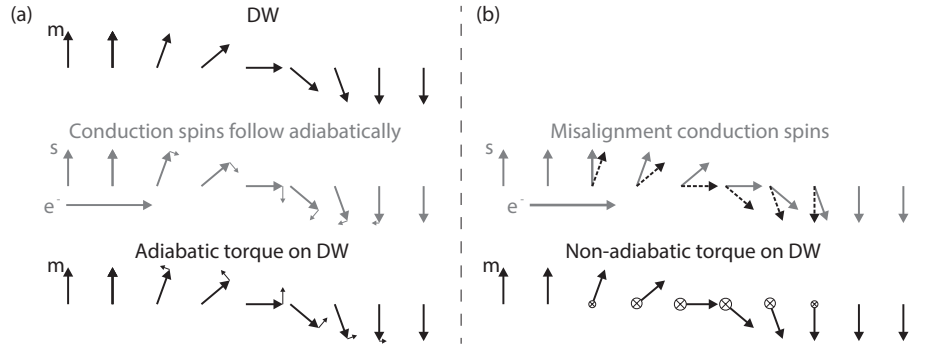

Figure 1.3 | Visualization of the adiabatic and nonadiabatic spin-transfer torque. (a) In the adiabatic case, the conduction electrons locally follow the magnetization direction, and the reaction torque on the magnetization causes the DW to move. (b) In the nonadiabatic case, the misalignment between the conduction electrons and the local magnetization causes an additional torque.

- A reliable way to *read and write* the information. Reading is possibly best achieved using a magnetic tunnel junction whose resistance changes depending on the orientation of the magnetic domain. Writing is more challenging, and in the original concept this is achieved by using a secondary racetrack containing a single DW, whose very strongly localized stray fields enable the writing of a small magnetic bit (Figure 1.1(d)). Those topics are not covered in this thesis either.
- *Reproducible* device operation. Since the motion of magnetic DWs will never be 100% reproducible, the positions of the DWs will become unpredictable after a number of pulses. This can be solved by engineering *pinning sites* at fixed intervals along the racetrack, where DWs tend to remain after being moved. In Part I of this thesis, we will explore several mechanisms to engineer such pinning sites.
- *Efficient* current-induced DW motion, by which we mean high DW velocities at reasonable power consumption. Perpendicularly magnetized materials are promising in this respect, because they have very narrow DWs which might lead to a large nonadiabatic torque. Furthermore, as we will discuss later, some very promising and surprising results have been reported recently, which point towards previously unknown mechanisms of DW motion. This is the topic of Part II of this thesis, where we aim at identifying the new mechanisms that dominate DW motion in PMA materials.

1.5 This thesis

The research performed in this thesis can be categorized into two Parts. Each of these Parts has its own introductory Chapter, providing the required context for

appreciating the other Chapters, which were originally published separately. At the end of the two respective introductory Chapters, an overview of the research in that Part is presented. At the very end of the thesis, a general conclusion and outlook is given. Below, we will provide a brief overview of the two Parts, without discussing the individual Chapters.

Part I: Controlling domain-wall pinning

In Part I, our aim is **to explore new methods for controlled pinning of magnetic DWs, and to employ these in novel device applications**.

In order to let DWs pin at well-defined positions, one needs to create *local energy minima* where DWs are trapped after their motion. In fact, a DW is an energetic frustration, and its energy cost can be tuned by making changes to the material. The conventional way to make pinning sites is by varying the geometry within the nanostrip. For example, by locally making the strip narrower, the DW is shorter hence costs less energy (see for example Figure 1.4(a)). However, this approach is not ideal for the PMA materials studied in this thesis, since shape-induced effects are largely overruled by the very high anisotropy. Therefore, several different approaches to induce pinning are explored in Part I of this thesis. Our main workhorse is the use of a focused gallium (Ga) ion beam to directly and permanently influence the PMA property on the nanometer scale[21–24] (details will follow in Chapter 2). We show that a discontinuity in the ion dose along the nanostrip creates a step in the DW energy potential, as visualized in Figure 1.4(b). It turns out that this approach is highly tunable, which inspires us to propose new device ideas in the context of racetrack memory and beyond. Some of these ideas are explored in detail, which includes the demonstration of a DW ratchet, a racetrack-like device that can be driven by a magnetic field instead of current. Furthermore, this pinning mechanism provides us with a very easy method to perform repeatable DW experiments, and therefore this technique is extensively used in the current-induced experiments in Part II, which we will discuss in the following section.

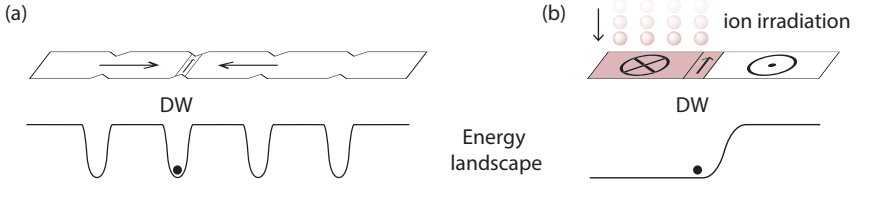

Figure 1.4 | (a) Conventional energy landscape with pinning sites induced by modifications to the shape of an in-plane nanostrip. (b) Our approach to create a pinning site in a PMA nanostrip: the DW energy is locally changed by ion irradiation. Note that the sketched energy landscape is actually an energy barrier, which is practical for the experiments in this thesis, but a profile like in (a) could also easily be made.

Part II: Current-induced effects

Part II is geared towards the fundamentals of current-induced DW motion, where the main goal is **to identify the main mechanisms that dominate the controversial current-induced DW motion in PMA materials**.

At the onset of this PhD work, there had been some highly interesting (and equally controversial) experimental results on current-induced DW motion in PMA materials. In Pt/Co multilayers, greatly varying values and even different signs for the efficiency of DW motion had been reported [25]. A particularly groundbreaking experiment was done by Moore *et al.* [26], who first reported a very high efficiency of DW motion in the system Pt/Co/AlOx, only to state in a later erratum [27] that the DWs had moved in the direction opposite to the expectation based on STT. Within our research group, Lavrijsen [28,29] also observed sign changes of the DW motion direction in Pt/Co/Pt which depended delicately on the thickness of the Pt layers, and was further influenced in unexpected ways by applying in-plane fields, for which a satisfying explanation was not found.

The second focus of this thesis, in addition to controlling the pinning, is therefore to identify the dominant transport mechanisms that are responsible for these surprising observations. During the years in which this research was conducted, various mechanisms were coined in literature that could partially explain these results. First, it was proposed that there is a significant contribution from Rashba spin-orbit coupling, which acts as an effective transverse magnetic field that stabilizes the DW structure, allowing for very fast DW motion [30]. However, it is still difficult to match this explanation with the fact that DWs in some cases move against the direction of electron flow. Later, it was shown by Liu *et al.* [31] that the so-called spin Hall effect (SHE) produces a remarkably strong vertical spin current that can be used to switch a ferromagnetic element. Inspired by this observation, we will show that the spin Hall effect also has a huge effect on DW motion, where the internal structure of the DW turns our to be of crucial importance (Bloch or Néel, see Figure 1.2). Furthermore, it turns out that by making Pt/Co structures with asymmetric top and bottom layers, not only the spin Hall effect, but also the internal structure of the DW can be tuned through an effect called the Dzyaloshinskii-Moriya interaction. The sensitivity of these effects to small details might explain the large spread in results that have been reported in recent years. All these intriguing phenomena will be introduced in more detail in the introductory Chapter 7 of Part II of this thesis, before presenting several experimental results in separate chapters.

Part I

Controlling domain-wall pinning

Introduction to domain-wall pinning by anisotropy modification

2

We theoretically and experimentally introduce the concept of domain-wall (DW) pinning at engineered anisotropy variations in Pt/Co/Pt strips with perpendicular magnetic anisotropy (PMA). First, an analytical model is derived showing that a step in the anisotropy acts as an energy barrier for the DW. Then, the fabrication techniques and methods for the experimental study of this phenomenon are introduced. Afterwards, quantitative measurements are performed showing that the anisotropy can be controlled by focused ion beam irradiation with Ga ions. This tool is then used to experimentally study the field-induced switching of nanostrips which are locally irradiated. The boundary of the irradiated area indeed acts as a pinning barrier for the DW and the pinning strength increases with the anisotropy difference. Furthermore, we demonstrate that not only the anisotropy itself, but also the width of the anisotropy barrier can be tuned on the length scale of the DW. Finally, a brief overview is given of the remainder of Part I, in which this technology is put to use. *

2.1 Introduction

Being able to control the position of DWs at will is essential for successful DW experiments or devices. One experimental issue is the initial creation of a magnetic DW. In a typical experiment, it is required to start with a single magnetic DW at a well-defined position in the nanostrip, before the motion of such a DW under influence of field and current can be investigated. However, reproducible creation of a DW in a nanostrip is not straightforward, as it requires localized control of the magnetization switching. Assuming for the moment that a DW is successfully injected, a second issue is to control the exact pinning positions where a DW stops

*Adapted from: *Domain-wall pinning by local control of anisotropy in Pt/Co/Pt strips*. J. H. Franken, M. Hoeijmakers, R. Lavrijsen, and H. J. M. Swagten, Journal of Physics: Condensed Matter **24**, 024216 (2012).

Section 2.6.5 adapted from: *Precise control of domain wall injection and pinning using helium and gallium focused ion beams*. J. H. Franken, M. Hoeijmakers, R. Lavrijsen, J. T. Kohlhepp, H. J. M. Swagten, B. Koopmans, E. van Veldhoven, and D. J. Maas, Journal of Applied Physics **109**, 07D504 (2011).

after propagation, which is needed in several memory and logic devices such as racetrack memory[7,32,33].

For the first issue of writing a domain at a controlled position, there are generally two possibilities: one should either apply a highly localized magnetic field, or locally modify the switching properties of the magnetic nanostrip to be able to write with a global field. A localized magnetic field generated by, for example, the Oersted field of a secondary nanowire[34] imposes restrictions on the experimental design and therefore writing with a global field is often more convenient. For in-plane magnetized DW devices made of permalloy, one often designs a variation in shape, such as a bend in the strip[16,35] or a large pad at the end of the strip[36–38]. Due to shape anisotropy, these lead to preferential nucleation points when an external field is applied. For PMA materials, however, there is a very strong perpendicular easy axis that dominates over shape-induced effects, by which nucleation preferably occurs at randomly distributed defects. Often, the approach is then to attach a very large area at one end of the nanostrip[39–41] to increase the chance of random DW nucleation, but this is not very reproducible. For the second issue of controlled DW pinning, similar considerations apply: geometric variations can be used for DW pinning[40,42] but these shape-induced effects are rather weak and typically lead to deformations of the DW[42], causing the DW to lose its well-defined one-dimensional (1D) character.

In a recent study[24], it was shown by us that both issues can be tackled at the same time by taking control over the parameter that governs the switching behavior: the PMA. The PMA is known to be reduced by irradiation with highly energetic ions[43–48] (see also section 2.4.2). Using a focused ion beam (FIB) of, for example, Ga[21–24] or He[49] ions, the anisotropy can be controlled very locally (at a scale of a few nanometer). By locally reducing the anisotropy, the coercivity is also reduced and a DW nucleation area is made. Furthermore, it was shown that DWs tend to pin at a discontinuity in the anisotropy, i.e. the boundary of a Ga-irradiated area, solving the second issue.

In this Chapter, we provide detailed insights into this pinning of DWs at engineered anisotropy variations. First, we outline the basic micromagnetic theory in section 2.2, followed by a derivation of the 1-dimensional DW model describing the mechanism responsible for pinning at anisotropy variations in section 2.3. Then, the experimental techniques to be used throughout this thesis are introduced in section 2.4. After introducing these theoretical and experimental tools, we show the first experimental results of this thesis. The magnetic anisotropy of Pt/Co/Pt strips is systematically measured as a function of Ga irradiation dose and Co layer thickness in section 2.5. Finally, in section 2.6, we report a detailed experimental study on DW pinning at an anisotropy boundary, showing that the DW energy landscape in a nanostrip can basically be engineered at will on a nanometer scale. After a brief conclusion in section 2.7, we will end with an outline of the remainder of Part I in section 2.8, where the described experimental and theoretical concepts will be used extensively.

2.2 Basic micromagnetic theory

We will now briefly introduce the relevant magnetic energy contributions in section 2.2.1, and provide more details on one of these contributions, the perpendicular magnetic anisotropy, in section 2.2.2.

2.2.1 Magnetic energy contributions

The spin structure of a magnetic body results from minimization of its total magnetic energy. The total magnetic energy density is generally described by [50],

$$U = \int_V \left(\underbrace{\frac{A}{|\mathbf{M}|^2}(\nabla \mathbf{M})^2}_{\text{exchange}} \underbrace{- \mu_0 \mathbf{M} \cdot \mathbf{H}_{\text{ext}}}_{\text{Zeeman}} \underbrace{- \frac{\mu_0}{2} \mathbf{H}_{\text{d}} \cdot \mathbf{M}}_{\text{demag.}} \underbrace{+ K_{\text{u}} \sin^2 \theta}_{\text{anisotropy}} \right) \mathrm{d}V. \tag{2.1}$$

Here, $\mathbf{M}$ is the (spatially varying) magnetization. The first term is the exchange interaction with A the exchange stiffness, which favors the parallel alignment of neighboring spins. The second term is the Zeeman energy, which tends to align the magnetization with the applied field $\mathbf{H}_{\text{ext}}$, where μ_0 is the vacuum permeability. The third term is the demagnetization energy[†], with $\mathbf{H}_{\text{d}}$ the demagnetizing field, which tends to organize the spins in such a way that flux closure within the magnetic structure is achieved and stray fields are minimized. The last term is the uniaxial anisotropy, which tends to align the spins along a certain easy axis, in our case perpendicular to the film plane. K_{u} is the uniaxial anisotropy constant (a material parameter) and θ the angle between the easy axis and $\mathbf{M}$. Other forms of anisotropy can also exist [50], but they are usually negligible in the class of materials that we study.

The demagnetizing field $\mathbf{H}_{\text{d}}$ relates to the geometry of the sample via

$$\mathbf{H}_{\text{d}} = -\mathcal{N}\mathbf{M} = -\begin{pmatrix} N_x & 0 & 0 \\ 0 & N_y & 0 \\ 0 & 0 & N_z \end{pmatrix} \mathbf{M}, \tag{2.2}$$

where $\mathcal{N}$ is the demagnetization tensor with $N_x + N_y + N_z = 1$. The demagnetization tensor depends on the shape; for a rectangular strip, a formula is given in [51]. A smaller dimension gives a higher demagnetization factor. Figure 2.1(a) shows the typical nanostrip geometry and defines the axes. Because the thickness t of our nanostrips is typically much smaller than both the width w and the length L, it is generally the case that $N_z \approx 1$ and $N_y > N_x \approx 0$ although they are both small. The demagnetization energy can be modeled as an effective anisotropy contribution, the *shape anisotropy*, which in the case of a nanostrip gives rise to an easy x, y-plane. For soft magnetic materials like permalloy, anisotropy contribution intrinsic to the material are very weak and the shape anisotropy is dominant. The effect of the

[†]The demagnetization energy is also known by the aliases *magnetostatic* energy and *stray field* energy.

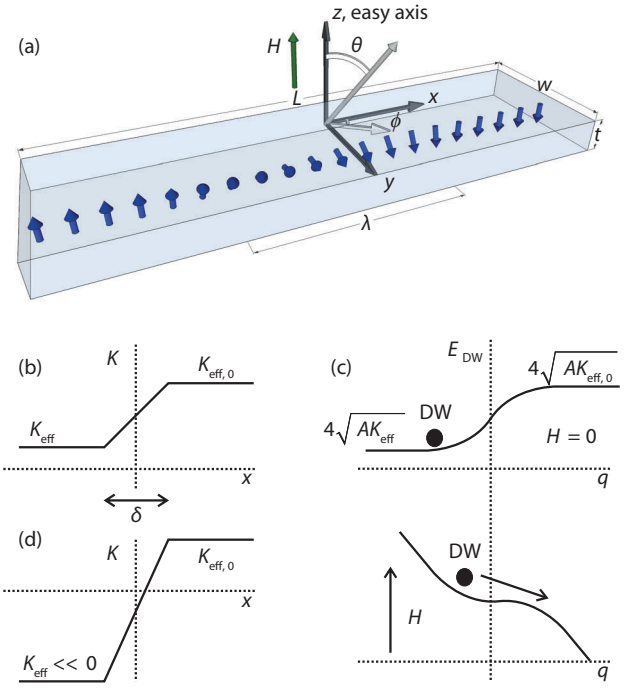

Figure 2.1 | (a) Sketch of a Bloch DW in a nanostrip and definition of the coordinate system. (b) Sketch of a step in the anisotropy along the strip direction x. Such a step leads to an energy barrier for a DW sitting to the left of the step, as sketched in (c). The barrier can be overcome by applying an external magnetic field that tilts the energy landscape. (d) Sketch of the anisotropy landscape in case the part $x \ll 0$ has in-plane magnetic anisotropy ($K_{\mathrm{eff}} < 0$).

shape anisotropy is to align the magnetization along the longest dimension of the magnetic volume.

In materials with perpendicular anisotropy, interface effects lead to a strong easy axis in the z direction which is only partly compensated by shape anisotropy. For a homogeneously magnetized thin film with perpendicular anisotropy, the effective anisotropy (terms 3 and 4 in (2.1)) is

$$K_{\mathrm{eff}} = K_{\mathrm{u}} - \frac{1}{2} N_z \mu_0 M_{\mathrm{s}}^2, \tag{2.3}$$

with $M_{\mathrm{s}} = |\mathbf{M}|$ the saturation magnetization, which is constant throughout the material.

Normally, for ultrathin PMA films, the energy is minimized by a monodomain state in which no DW is present. However, in practice, it happens often that a layer switches only partially such that a metastable state with a DW arises. For thick

layers, a state with DWs actually becomes the ground state because it reduces the demagnetization energy. If we assume the existence of a DW, the competition between the exchange energy and the effective anisotropy energy determines its width (λ in Figure 2.1(a), typically 10 nm). The exchange interaction tends to widen a DW, since a gradual transition from one magnetization direction to the other gives a smaller energy drawback than an abrupt change. The anisotropy energy favors infinitely thin DWs, because in that case none of the spins makes an angle with the easy axis and the anisotropy energy is zero. To a good approximation, the balance between exchange and anisotropy gives rise to the following expression for the DW width [50,52],

$$\lambda = \sqrt{\frac{A}{K_{\text{eff}}}}. \tag{2.4}$$

We will discuss the precise profile of the DW later in section 2.3.1. From (2.4), it is immediately seen why the anisotropy K_{eff} is such an important parameter. The higher K_{eff}, the smaller the DW, hence the more data can be stored on the same area. We will now briefly introduce what determines the strength of the uniaxial contribution K_{u} in Pt/Co multilayers.

2.2.2 Perpendicular magnetic anisotropy

Pt/Co/Pt can be considered the archetypical PMA material, and is also the reference system in this thesis. The uniaxial anisotropy in these materials is usually caused by effects at the Pt/Co interfaces and is therefore only present in ultrathin magnetic films, where interface effects can dominate over the bulk behavior. If the surface contribution from each Pt/Co interface is denoted by K_{s}, the resulting uniaxial anisotropy depends on the thickness via [53]

$$K_{\text{u}} = \frac{2K_{\text{s}}}{t}. \tag{2.5}$$

We now briefly discuss how a significant K_{s} arises at a Pt/Co interface. A more detailed account on the origin of magnetic anisotropy can be found in textbooks [54]. The main effect responsible for PMA is the *spin-orbit coupling*, which describes the coupling between the orbital angular momentum **L** and spin angular momentum **S**, via the Hamiltonian

$$\mathscr{H} = \xi \mathbf{L} \cdot \mathbf{S}, \tag{2.6}$$

where ξ is a constant depending on the material. The existence of such a coupling between the electron spin and its orbital motion is easily understood in a semiclassical picture. Consider an electron orbiting around a nucleus. In the rest frame of the electron, the positively charged nucleus rotates around the electron, thereby creating a magnetic field. The spin of the electron couples to this magnetic field via Zeeman spin splitting, lifting the degeneracy of the spin state.

From (2.6), it is clear that an anisotropy in **L** gives rise to a favorable direction of **S**, hence a magnetic anisotropy. If the atoms are arranged in a perfect crystal, such an anisotropy can arise along the axes of the crystal. However, the bulk crystal structure cannot explain the high anisotropy that is present in our films which are

grown by sputter deposition, since they are relatively disordered hence do not have a well-defined global crystal axis. In this case, an anisotropy in **L** caused by the bonding orbitals at the interfaces leads to an anisotropy in **S** via spin-orbit coupling, leading to a strong perpendicular magnetic anisotropy.

2.3 1D model of domain-wall pinning [‡]

In this section, we investigate how DWs are pinned at intended anisotropy modulations by assuming a simple model system (Figure 2.1(a)). The system consists of a PMA strip of length L, width w, and thickness t. We assume that a single 1D Bloch DW is present in the strip, centered at a certain position q along the x-axis. The strip has perpendicular magnetic anisotropy, but the anisotropy changes at $x = 0$. We assume a linear transition between two values over a gradient length δ centered at $x = 0$. The part $x < -\delta/2$ has an effective perpendicular anisotropy constant K_{eff} and the part $x > \delta/2$ has $K_{\text{eff},0} > K_{\text{eff}}$ (Figure 2.1(b)). The other relevant parameters M_s (saturation magnetization) and A (exchange constant) are kept constant.

It is very easy to get a basic understanding of why such an anisotropy step leads to pinning. Since the energy of a DW scales approximately as $\sqrt{K_{\text{eff}}}$, the anisotropy change at $x = 0$ causes an energy barrier as sketched in Figure 2.1(c). The larger the anisotropy difference, the larger this barrier. By applying an external field H, the potential landscape is tilted making it possible for the DW to escape as soon as the tilt slope cancels the maximum slope of the DW energy landscape.

In the following, we derive expressions for the pinning field H_{pin} as a function of the anisotropy of the left part of the strip, K_{eff}. We will discuss the two cases shown in Figure 2.1(c) and Figure 2.1(d). The situation of Figure 2.1(b), in the limit that the anisotropy step is small, is discussed in section 2.3.1. In section 2.3.2, we discuss the situation where the part $x < 0$ has strong in-plane (shape) anisotropy, $K_{\text{eff}} \ll 0$, as sketched in Figure 2.1(d). In section 2.3.3, we compare the analytical model with full micromagnetic simulations and find good agreement.

2.3.1 Pinning at small anisotropy step

A DW represents a rotation of the magnetization from $+z$ to $-z$, as shown in Figure 2.1(a). The absolute magnetization $|\mathbf{M}| = M_s$ is constant everywhere, but the direction characterized by the polar angle θ and the azimuthal angle ϕ is allowed to vary. The energy is minimized if the DW assumes a Bloch profile, with θ given by [55]

$$\theta(x) = \pm 2 \arctan\left[\exp\left(\frac{x-q}{\lambda}\right)\right], \tag{2.7}$$

with λ the DW width. The azimuthal angle ϕ can be assumed constant throughout the wall, and normally the Bloch wall with $\phi = \pm\pi/2$ is favorable in wide strips, since this aligns the magnetization within the DW along its longest axis ($w \gg \lambda$).

[‡]This section only treats the static energy of a DW, which suffices to explain DW depinning in a quasi-static experiment. The time-dependent dynamics of DWs are governed by the Landau-Lifshitz-Gilbert equation introduced in Chapter 7.

The standard profile (2.7) is not exactly valid in the vicinity of the anisotropy interface since the part of the DW residing in the low-K region tends to widen via (2.4), but this effect is negligible in the limit studied. Considering effective anisotropy and exchange contributions, the magnetic energy density is [55]

$$\begin{aligned} w(x) &= A\left[\left(\tfrac{\partial\theta}{\partial x}\right)^2 + \left(\sin\theta\,\tfrac{\partial\phi}{\partial x}\right)^2\right] + K(x)\sin^2\theta \\ &= \left(\tfrac{A}{\lambda^2} + K(x)\right)\operatorname{sech}^2\left(\tfrac{x-q}{\lambda}\right), \end{aligned} \tag{2.8}$$

where $K(x)$ has the profile sketched in Figure 2.1(b),

$$\begin{aligned} K(x) &= K_{\mathrm{eff}} && (x < -\delta/2), \\ K(x) &= \tfrac{K_{\mathrm{eff},0}+K_{\mathrm{eff}}}{2} + (K_{\mathrm{eff},0} - K_{\mathrm{eff}})\tfrac{x}{\delta} && (-\delta/2 \le x \le \delta/2), \\ K(x) &= K_{\mathrm{eff},0} && (x > \delta/2). \end{aligned} \tag{2.9}$$

Because the DW width can be considered constant in the limit studied, the term A/λ^2 in (2.8) can be omitted for simplicity. Furthermore, we already mentioned that ϕ is constant. The total DW energy per unit cross-sectional area E_{DW} of a DW centered at q is then (up to a constant) given by

$$\begin{aligned} E_{\mathrm{DW}}(q) = \int_{-\infty}^{\infty} w(x)\mathrm{d}x = \frac{\lambda}{\delta}\Big(&2K_{\mathrm{eff},0}\delta + (K_{\mathrm{eff},0} - K_{\mathrm{eff}})\,\lambda \\ &\times\left(\ln\left[1 + e^{-\frac{2q+\delta}{\lambda}}\right] - \ln\left[1 + e^{\frac{-2q+\delta}{\lambda}}\right]\right)\Big). \end{aligned} \tag{2.10}$$

By applying an external magnetic field H in the z-direction, the energy landscape of the DW is tilted due to the Zeeman energy, giving a total energy $E(q)$

$$E(q) = E_{\mathrm{DW}}(q) - 2\mu_0 M_{\mathrm{s}} H q. \tag{2.11}$$

For estimating the pinning field, we are interested in the derivative of the DW energy with respect to q, which should be negative at any position in order for the DW to depin,

$$\frac{\mathrm{d}E}{\mathrm{d}q} = \frac{2(K_{\mathrm{eff},0} - K_{\mathrm{eff}})\lambda \sinh\left[\frac{\delta}{\lambda}\right]}{\delta\left(\cosh\left[\frac{2q}{\lambda}\right] + \cosh\left[\frac{\delta}{\lambda}\right]\right)} - 2\mu_0 M_{\mathrm{s}} H < 0\,. \tag{2.12}$$

Hence, the maximum of $\frac{\mathrm{d}E}{\mathrm{d}q}$ should be negative,

$$\max_{-\infty<q<\infty}\frac{\mathrm{d}E}{\mathrm{d}q} = \left.\frac{\mathrm{d}E}{\mathrm{d}q}\right|_{q=0} = (K_{\mathrm{eff},0} - K_{\mathrm{eff}})\frac{2\lambda}{\delta}\tanh\frac{\delta}{2\lambda} - 2\mu_0 M_{\mathrm{s}} H < 0. \tag{2.13}$$

The DW thus depins for $H > H_{\mathrm{pin}}$, with

$$H_{\mathrm{pin}} = \frac{K_{\mathrm{eff},0} - K_{\mathrm{eff}}}{2\mu_0 M_{\mathrm{s}}} \times \frac{2\lambda}{\delta}\tanh\frac{\delta}{2\lambda}. \tag{2.14}$$

In case the length scale of the anisotropy gradient δ is much smaller than the DW width λ, the pinning field is simply given by the difference of the anisotropy values,

$$\lim_{\delta\to 0} H_{\text{pin}} = \frac{K_{\text{eff},0} - K_{\text{eff}}}{2\mu_0 M_s}. \tag{2.15}$$

The opposite limit is also interesting; it turns out that the pinning field becomes zero if $\delta \gg \lambda$,

$$\lim_{\delta\to\infty} H_{\text{pin}} = 0, \tag{2.16}$$

which means that a DW will only pin if δ is at a length scale comparable to the DW width, typically in the range of 10 nm.

2.3.2 Pinning at in-plane to out-of-plane transition

If the perpendicular uniaxial anisotropy is quenched completely, this results in an effective in-plane anisotropy. Therefore, the DW at the moment of depinning does not necessarily represent an 'up' to 'down' transition. If the effective in-plane anisotropy is small, the out-of-plane field that is applied to achieve DW injection is already enough to pull the magnetization fully out-of-plane and the origin of the DW pinning field is not physically different from the case studied in the previous section. However, if the in-plane shape anisotropy is strong, there will always be a 90° DW present at the interface, and reversal is merely initiated by nucleation of a DW at this interface that will propagate through the out-of-plane part of the strip. In the following, we will attempt to model this situation by assuming that the in-plane anisotropy is so large that the spins are completely in-plane in the irradiated area, even though a perpendicular field is applied. This in fact corresponds to infinite in-plane anisotropy. Furthermore, it is assumed that the Bloch profile is still valid, but rescaled from the domain $\theta \in [0, \pi]$ to $\theta \in [0, \frac{\pi}{2}]$. The profile then reads (notice the factor 2 difference with (2.7))

$$\theta(x) = \pm \arctan\left[\exp\left(\frac{x-q}{\lambda}\right)\right]. \tag{2.17}$$

By micromagnetic simulations of an in-plane to out-of-plane transition in a strip, we verified that this profile is reasonably precise. To simplify the calculation, we only consider the case $\delta = 0$, because the precise shape of the anisotropy profile was found not to matter in the limit studied. The DW energy density reflects the change of easy axis at $x > 0$:

$$\begin{aligned} w(x) &= \tfrac{A}{4\lambda^2} + \left|K_{\text{eff}}\right| \cos^2\theta \\ &= \tfrac{A}{4\lambda^2} + \left|K_{\text{eff}}\right| \frac{1}{\exp\left(2\frac{x-q}{\lambda}\right)+1} \qquad (x<0), \end{aligned} \tag{2.18}$$

$$\begin{aligned} w(x) &= \tfrac{A}{4\lambda^2} + K_{\text{eff},0} \sin^2\theta \\ &= \tfrac{A}{4\lambda^2} + K_{\text{eff},0} \frac{\exp\left(2\frac{x-q}{\lambda}\right)}{\exp\left(2\frac{x-q}{\lambda}\right)+1} \qquad (x>0). \end{aligned} \tag{2.19}$$

In analogy with (2.12), the derivative of E_{DW} becomes

$$\frac{\mathrm{d}E_{\mathrm{DW}}}{\mathrm{d}q} = \frac{K_{\mathrm{eff},0}\exp\left(\frac{2q}{\lambda}\right) - \left|K_{\mathrm{eff}}\right|}{\exp\left(\frac{2q}{\lambda}\right)+1}. \tag{2.20}$$

This function is monotonically increasing and is maximal at $q \to \infty$. Therefore, the maximum slope of the energy barrier is given by

$$\max_{-\infty<q<\infty} \frac{\mathrm{d}E_{\mathrm{DW}}}{\mathrm{d}q} = K_{\mathrm{eff},0}. \tag{2.21}$$

A more detailed analysis shows that at finite in-plane anisotropy, if a small z-component of magnetization is assumed for $x < 0$, the maximum derivative is not at ∞ but close to $q = 0$ (retaining the same magnitude), so that injection indeed occurs at the anisotropy interface. The derivative of total energy includes again a Zeeman term, which now has half the original magnitude, because the z-component of magnetization is zero at one end of the DW. Therefore,

$$\max_{-\infty<q<\infty} \frac{\mathrm{d}E}{\mathrm{d}q} = K_{\mathrm{eff},0} - \mu_0 M_{\mathrm{s}} H, \tag{2.22}$$

and the pinning field is found by equating this expression to zero,

$$H_{\mathrm{pin}} = \frac{K_{\mathrm{eff},0}}{\mu_0 M_{\mathrm{s}}}. \tag{2.23}$$

2.3.3 Comparison to micromagnetic simulations

To test the validity of (2.14) and (2.23), micromagnetic simulations[§] are performed on a strip with $w = 60\,\mathrm{nm}$, $t = 1\,\mathrm{nm}$, and length $L = 400\,\mathrm{nm}$. The simulation cell size is $4 \times 4 \times 1\,\mathrm{nm}^3$. Reducing the simulation cell size did not significantly change the obtained results. The saturation magnetization $M_{\mathrm{s}} = 1400\,\mathrm{kA/m}$ and the exchange constant $A = 16\,\mathrm{pJ/m}$. The uniaxial anisotropy constant of the right part of the strip was fixed at $K_0 = 1.5\,\mathrm{MJ/m}^3$, yielding an effective anisotropy $K_{\mathrm{eff},0} = K_0 - \frac{1}{2}\mu_0 N_z M_{\mathrm{s}}^2 = 0.305\,\mathrm{MJ/m}^3$. The left part of the strip has a variable effective anisotropy $K_{\mathrm{eff}} < K_{\mathrm{eff},0}$. The starting configuration is a DW that is artificially created at the boundary and then energetically relaxed at zero applied field. Then, the field is increased in small steps, and at each field step the LLG solver iterates until the torque on the magnetization is virtually zero. The result is shown in Figure 2.2.

The situation $\delta \to 0$ is shown as open circles in Figure 2.2, and H_{pin} from the 1D model (2.15) is plotted as a solid line. In the regime where the anisotropy difference is rather small, good agreement is found. We also see that as the anisotropy becomes negative (in-plane), the simulated data approaches the derived limit (2.23),

[§]Micromagnetic simulations are a standard technique, which solves the magnetization dynamics on a grid of cells which are coupled via the various magnetic energy terms. Here, we are not interested in the dynamic solution, but let the magnetization relax to find a local energy minimum. Various micromagnetic frameworks are available, and we use the LLG micromagnetics simulator by M. Scheinfein [56].

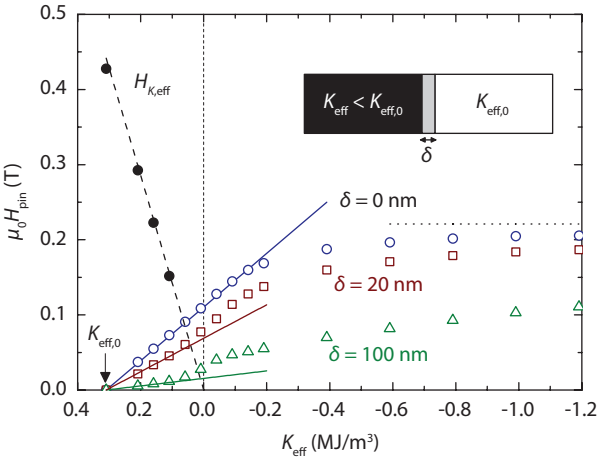

Figure 2.2 | H_{pin} obtained from micromagnetic simulations of DW depinning at a sharp anisotropy step (open circles), or a gradual anisotropy increase (open squares and triangles). The solid and dotted lines show the limiting cases of the 1D model derived in the text. The filled circles are simulated nucleation fields of the left area, which dominate the switching of the entire strip if if reversal is started from a saturated state (as in experiment).

shown as the dotted horizontal line. The situation of a finite length δ is also simulated, by changing the values of the anisotropy on the simulation cell level. For instance, to simulate a length $\delta = 20\,\text{nm}$, the anisotropy is step-wise increased over a width of 5 cells, which are each 4 nm wide. This approach is valid as long as the cell size is of the order of the exchange length. Plotting the 1D limit (2.14) in this case is slightly more complicated because it also contains the DW width λ, which in turn depends on the anisotropy at the DW position. For the plotted lines, we simply used $\lambda = \sqrt{A/K_{\text{eff},0}} \approx 7\,\text{nm}$, which again shows excellent agreement in the evaluated limit. Interestingly, for larger anisotropy differences, we see that the pinning field in the simulations bends upwards from the limit. This is simply because λ increases, as it is partially in a region with lower K_{eff}. If we take into account this increasing λ, the 1D model also predicts this upturn, demonstrating the power of the 1D approach.

In the experimental situation, starting from a saturated state, a DW does not readily exist but must first be nucleated. Therefore, simulations starting from the saturated state were also conducted, shown as the solid circles in Figure 2.2. It is consistently observed that the DW is nucleated in the left part of the strip. For relatively high K_{eff}, the nucleation field is much higher than the pinning field and therefore dominates the switching field of the entire strip. The nucleation field in the simulations matches that of a Stoner-Wohlfart particle and is in good approximation given by the anisotropy field $H_{K_{\text{eff}}} = 2K_{\text{eff}}/(\mu_0 M_s)$, plotted as the dashed line. We should note that this nucleation field has no quantitative meaning in experiments, where the switching behavior does not show coherent Stoner-Wohlfart

behavior, but is dominated by domains nucleating at random defects and their expansion by DW motion [57].

To conclude this section, we have shown by analytical modeling and micromagnetic simulations, that a DW can be pinned at an anisotropy boundary. The field strength needed for depinning depends linearly on the anisotropy difference if the boundary is not too high. Interestingly, it was shown that a DW can also be injected from a boundary between an in-plane and out-of-plane anisotropy region. Furthermore, not only the height of the anisotropy boundary, but also its spatial extent (width), is an extra parameter that tunes the pinning field, and should be at the length scale of the DW for pinning to occur. In the next sections, we study quantitatively how Ga FIB irradiation can be used to tune the anisotropy (Section 2.5), and how DW pinning and nucleation can be controlled using this tool (Section 2.6). However, we will first introduce a general experimental toolbox that is used throughout this thesis.

2.4 Experimental toolbox

In this section, we outline the most important experimental techniques that are employed throughout this thesis. We will discuss the fabrication of nanostructures by electron beam lithography in section 2.4.1, the FIB irradiation procedure in 2.4.2, and Kerr microscopy which is used as a very powerful tool to directly visualize the magnetic domain structure in 2.4.3.

2.4.1 Sample fabrication

Small structures are produced using a standard electron beam lithography (EBL), sputtering and lift-off process. A schematic picture of this process is shown in Figure 2.3. We outline the basic steps below:

- The sample substrate, usually Si with a thermally oxidized SiO_2 layer of either 100 nm or 1 μm, is cleaned in an ultrasonic bath of ammonia (25%), aceton and isoropanol, respectively.
- A bi-layer of the positive resist PMMA is spin-coated on the substrate. The bottom PMMA layer is approximately 200 nm thick and consists of polymer chains of (on average) 450k repetitions, whereas the second layer is 60 nm thick and is harder because of the longer polymer chains (950k repetitions). After each spinning step, the resist is baked for 2 minutes at 150 °C on a hot plate, to remove the solvent (anisole).
- To define the desired pattern, EBL is performed using the electron beam in a FEI Nova dualbeam system. The energy of the incident electrons (30 keV) breaks the PMMA chains and makes the material softer and dissolvable.
- The exposed structure is developed in a solution of methyl isobutyl ketone (MIBK), opening the layer where the electron beam has scanned. The gaps have an undercut because the bottom layer is softer and thus dissolves more easily.
- The entire sample is covered with the desired Pt/Co/Pt stack by DC sputtering (see e.g. [28] for more details) using a $\sim 10^{-2}$ mbar Ar plasma (system base pressure 2×10^{-8} mbar). Optionally, the surface is first cleaned in an O_2 plasma at 0.1 mbar and 150 W for 5 minutes, without breaking the vacuum.

- Lift-off in aceton removes the remaining resist and all the sputtered material on top of it, but leaves behind the sputtered layers in the gaps. Hereby, the desired structures are completed.
- The above can be repeated several times depending on the desired structure, for example one additional repeat to define electrical contacts. These contacts connect the magnetic structure to predefined Au/Pt strips on the substrate, which are in turn connected to a macroscopic chip carrier by wirebonding.

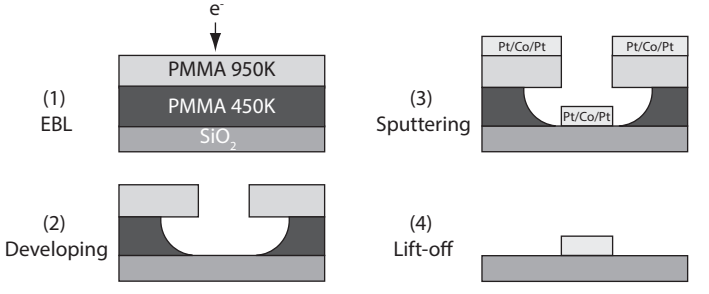

Figure 2.3 | Schematic drawing of the production process of patterned samples by EBL, sputtering and lift-off.

The main advantage of EBL/lift-off is that it is very flexible (no masks required) and has a better spatial resolution than for instance UV-lithography. The main drawback of any lift-off process is that edges tend to be rather rough and ill-defined due to shadowing by the undercut. This is not a big problem for wide structures, down to $\sim 1\,\mu$m, but for narrow strips the roughness is large relative to the strip width and this could lead to stronger DW pinning. Almost all strips used in this thesis were > 500 nm, which is quite large for applications, but this does not prevent us from performing relevant physics experiments. Furthermore, since we mostly make use of magneto-optic microscopy (which we will introduce in section 2.6.1), relatively wide strips are required to be optically resolvable.

2.4.2 Focused ion beam irradiation

For the experiments in this thesis, we will extensively use a FIB to modify the magnetic anisotropy of Pt/Co-based materials. The FIB available in our lab is part of a FEI Nova dualbeam system which combines, amongst other tools, an electron- and an ion beam. In this apparatus, a beam of Ga ions accelerated to 30 keV is focused into a tiny spot (~ 10 nm), which is scanned over the sample surface. The usual application of FIB is to locally remove materials in order to expose buried layers or to 'drill holes'. However, we use only very low doses of Ga (very short exposure times at the lowest beam current, 1.5 pA) which is not enough to actually remove material, but which does significantly alter the magnetic properties, in particular the anisotropy[21–23,43–48]. We use the same lithography framework (RAITH) as for

the EBL step in the previous section, which allows us to precisely align the irradiation pattern to the microstructures which contain alignment marks. Before starting the actual exposure, some FIB images are recorded to determine the position of the alignment marks. Care must be taken not to expose the actual structures during this procedure, because that will immediately destroy the PMA. Therefore, electron beam imaging is used to approximately navigate to the correct position, before doing the final alignment with the ion beam.

We will explain qualitatively how the perpendicular anisotropy (introduced in section 2.2.2) is reduced by FIB irradiation. Using a model taking into account ballistic recoils and by measurements on the atomic structure, it was proposed that the following mechanisms are responsible for the reduction of the anisotropy under FIB irradiation [46]:

- Due to the lattice mismatch between Pt and Co, the Co layer is under tensile stress. This leads to an additional anisotropy contribution. By FIB irradiation, the stress is relieved and therefore the anisotropy is reduced. This effect is non-linear with dose and occurs already at very low doses. It is more important for thicker Co layers, since the magnetoelastic anisotropy is a volume effect.
- Due to increased roughness of the Pt/Co interfaces after FIB irradiation, the interface anisotropy is reduced. This is the dominant contribution to anisotropy reduction for ultrathin Co layers of ~ 0.5 nm, the thickness range we use. The increased roughness after irradiation is visualized in Figure 2.4. There could arise an asymmetry between the two Pt/Co interfaces, which is mainly caused by the Co penetrating more easily into the Pt than the other way around [46]. The intermixing is thus mainly caused by the motion of the Co atoms. Co atoms moving downwards (along with the Ga ions) travel more than one interatomic distance and become isolated (Co-Pt alloying), whereas Co atoms moving in the opposite direction travel typically only one interatomic distance and contribute to roughness.

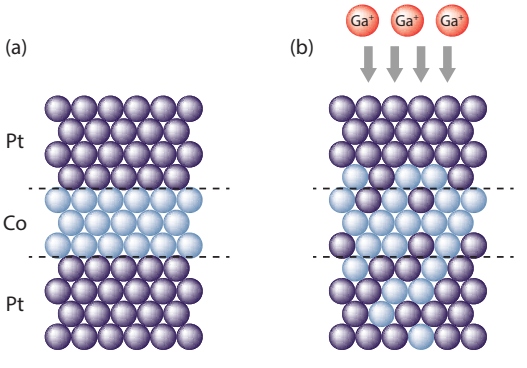

Figure 2.4 | Schematic picture of the atomic arrangement (a) before and (b) after Ga irradiation. After [46].

2.4.3 Kerr microscopy

In a typical study on DW motion, one needs to detect a local change in the magnetization direction under influence of a magnetic field or current. An easy and flexible way to do this is by the Magneto-optical Kerr effect (MOKE). This effect describes a change in the polarization of light upon reflecting from a magnetic material.

MOKE can qualitatively be described by the classical motion of free electrons in the medium [50,58]. For simplicity, consider the magnetization as a magnetic field. An incident beam of linearly polarized light causes the electrons in the material to follow the electric field, leading to an oscillation in the direction of polarization. However, due to the magnetic field that is present, a Lorentz force acts on the moving electrons giving it a velocity component perpendicular to the electric and magnetic field. This generates a secondary amplitude in the reflected light. Superimposed on the normally reflected light, this gives rise to a rotation of the polarization that depends on the magnetization. The phase shift between the two components causes the ellipticity that is experimentally observed. For a more formal explanation of the effect in ferromagnets, the spin-orbit interaction needs to be taken into account, since it couples the electron spin to its motion.

Regardless of its origin, MOKE is very useful to obtain a *relative* measure of the magnetization by measuring the polarization rotation. A typical MOKE setup uses a light source shining through a linear polarizer, which then reflects from the magnetic sample and goes through a second polarizer (called the analyzer) oriented at 90° to the first, before entering a detector. The scheme is very versatile, since the combination of angle of incidence and polarization direction determines whether the *polar*, *longitudinal*, or *transverse* component of the magnetization is measured. In this thesis, we only study the perpendicular magnetization hence *polar* MOKE is used, which simply uses normal incidence.

Often, a laser beam is used for MOKE measurements, which probes the average magnetization within the area of the laser spot. However, to obtain a spatially resolved image of the magnetization as a function of time, one would need to repeat the experiment many times and move the sample to a different position every time. This can be very slow, requires a very good focus of the laser spot, and also requires a perfect reproducibility of the magnetic switching process, which is usually not the case due to the random influence of thermal activation. A very useful way to obtain a wide view of the magnetic domain structure is by using a conventional microscope with polarizing optics. Such a microscope, optimized for MOKE measurements, is called a *Kerr microscope* [59]. Since it is easy to swap objective lenses, the field-of-view can range from a cm to $\sim 10\,\mu$m. The resolution is limited only by the diffraction limit, such that 500 nm wide strips are easily resolved, and even smaller domains can be observed using oil-immersion techniques. The time resolution is limited by the CCD camera that is used, and typically a rate of 16 frames per second is achieved, which can be increased at the expense of a lower intensity or a smaller pixel grid. A Kerr microscope from Evico magnetics [60] was used throughout this thesis, and is schematically shown in Figure 2.5.

Figure 2.5(a) shows the ray diagrams from the lamp to the sample, and Figure 2.5(b) shows the path from sample to detector. Light emitted from a stable high-intensity Xenon arc lamp is focused onto the plane of the aperture diaphragm,

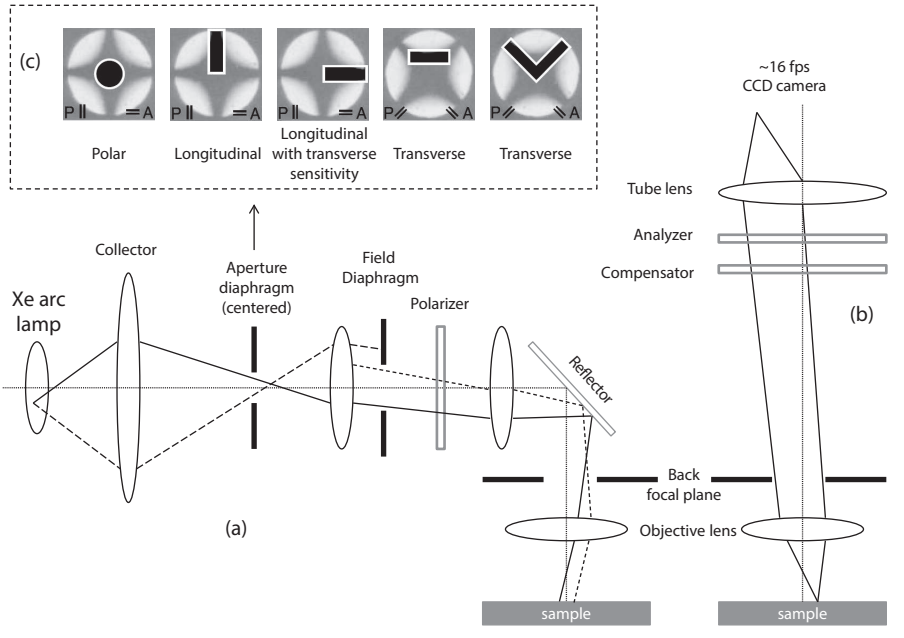

Figure 2.5 | Wide-field Kerr microscopy. (a) Illumination path for perpendicular incidence. The angle of incidence is controlled by the aperture diaphragm, which can be positioned with respect to the center as visualized in (c) (black areas), to change from polar (perpendicular) to longitudinal or transverse (in-plane) sensitivity. The light is linearly polarized before reaching the sample. (b) Image-forming path from sample to detector. The Kerr rotation is measured by an analyzer, optionally with a compensator to transform Kerr ellipticity to Kerr rotation. The obtained image is projected on a CCD detector. After [28, 59].

passes through a linear polarizer, is deflected into the objective lens, and finally reaches the sample. High quality stress-free lenses are used to allow for polarization analysis. The aperture diaphragm is a rectangular opening whose width, height, and position can be changed by the user, in order to select the angle of incidence of the light on the sample. This is crucial, since it determines the probed magnetization direction as indicated in Figure 2.5(c). For polar MOKE, the aperture diaphragm is simply centered to obtain normal incidence of light. After reflection, the light passes through an optional compensator, which can remove the ellipticity by phase-shifting the two components of the light, and an analyzer that is crossed with the initial polarizer. In this way, the transmitted intensity is in large part due to the rotation induced by the sample, providing a measure of the magnetization. The image recorded by the CCD can be enhanced in real-time by digital image processing software, containing features like contrast enhancement and background subtraction, such that changes to the domain structure really stand out.

For the current-induced experiments in Part II of this thesis, a sample holder with electrical contacts was built in-house, in order to apply currents and measure voltages while monitoring the domain structure in real-time. To control the magnetic field, various electromagnets are available. For simple out-of-plane measurements like in this Chapter, an uncooled, coreless solenoid is employed, which allows for perpendicular fields up to 100 mT. For experiments with both in-plane and out-of-plane fields (Chapters 9 and 10), a water-cooled 3D magnet was fabricated so that x, y, and z fields up to 40 mT can be independently applied. The currents through the electromagnets are computer-controlled via a bipolar Kepco power supply. Specific LabView programs were developed to automate most of the Kerr microscopy experiments in this thesis.

2.5 Manipulating the anisotropy of Pt/Co/Pt

Whereas it is widely accepted that Ga and He irradiation reduces the PMA of sputtered Pt/Co/Pt films, the evidence is usually indirect, i.e. through measurement of the coercive field. The anisotropy has been systematically measured as a function of He irradiation dose [46], but to our knowledge, a systematic data set of anisotropy as a function of Ga dose is lacking. Performing a quantitative measurement of the anisotropy as a function of Ga dose is therefore interesting in its own right, as well as insightful for the interpretation of DW pinning and nucleation in section 2.6 and the remainder of this thesis.

Common methods to quantitatively measure the anisotropy of magnetic samples make use of Stoner-Wohlfarth theory [61]. Typically, an external field H is applied under an angle α with the easy axis of magnetization. The magnetization is pulled away from its favored direction, toward the field direction. The ease by which the magnetization can be pulled is a measure of the anisotropy. We use the anomalous Hall effect (AHE) to measure $M_z(H, \alpha)$ on Hall crosses that have been irradiated with varying Ga doses, and obtain quantitative values for K_{eff} by fitting to the theoretical model [62].

2.5.1 Experimental details

Fabrication of Hall crosses

For this particular experiment, samples containing four Hall crosses of 5 μm wide Pt(4 nm) / Co(t nm) / Pt(2 nm) are deposited on a Si / SiO_2(100 nm) substrate. The thickness of the Co layer is varied from 0.4 to 0.6 nm. On top of the branches of the Hall crosses, 20 nm thick Pt contacts are deposited using a second EBL step for electrical contact. A micrograph of the resulting sample is shown in Figure 2.6(a).

After the deposition of the Pt contacts, the Hall crosses are irradiated with different Ga doses. The ions have an energy of 30 keV and a beam current of ~ 1.5 pA is used. The dose is varied from 0.07×10^{13} ions/cm^2 to 1.3×10^{13} ions/cm^2. This dose range does not lead to significant etching, but only affects the Pt/Co interfaces [21,44]. The irradiated region for each Hall cross is indicated in Figure 2.6(a).

Anomalous Hall effect measurements

Phenomenologically, the AHE is comparable to the ordinary Hall effect (OHE), where the perpendicular magnetization takes the role of a perpendicular magnetic field. However, the effect is *not* due to the contribution of the magnetization to the total magnetic field, but has a totally different origin. Although there still is a lot of debate on the exact origin of the AHE, it is generally accepted as a probe of the magnetization component perpendicular to the plane and widely used in published results.[¶] A review of the various theories can be found in [63].

In experiments, the measured Hall resistivity ρ_{H} is a superposition of the OHE and the AHE,

$$\rho_{\mathrm{H}} = R_{\mathrm{OHE}} H_z + R_{\mathrm{AHE}} M_z, \tag{2.24}$$

where R_{OHE} and R_{AHE} are constants that characterize the strength of the respective effects. The AHE is usually much larger than the OHE in perpendicularly magnetized materials. The OHE is a small contribution that is linear in the applied field, which is easy to correct for.

After fabrication of the Hall crosses, they are loaded in a sample rod within a cryostat (at room temperature), surrounded by a rotatable electromagnet which can apply fields up to 900 mT. Four lock-in amplifiers are used to measure the AHE as a function of applied magnetic field on four different Ga-irradiated crosses at the same time. An AC current with a density of $\sim 3.0 \times 10^9\,\mathrm{Am}^{-2}$ at a frequency of 5 kHz is sent through the strip. The external field is applied under a variable angle α (see inset of Figure 2.6(b)). The measured lock-in voltage consists of the AHE plus a small contribution of the OHE. Since the AHE is constant when the magnetization is saturated, we can use the measured signal slope at high perpendicular fields to subtract the OHE from all other measurements.

Figure 2.6(b) shows a typical measurement of M_z/M_{s} for various α. All traces are fitted globally using a fitting routine based on energy minimization of the Stoner-Wohlfart model. Input parameters within the model are the applied field H, the angle α, the perpendicular magnetization M_z and the saturation magnetization M_{s}. The latter is estimated at $1.4 \times 10^6\,\mathrm{A/m}$ from SQUID measurements[‖]. The fit yields a value of the perpendicular anisotropy K_{eff}. The second order crystalline anisotropy is found to be negligible and therefore is not taken into account in the final fit.

It can be seen in Figure 2.6(b) that for nearly in plane fields ($\alpha > 80°$) there is a strong deviation between the fits and the experimental data. This is known to arise from non-coherent magnetization reversal processes, wherein the structure no longer behaves as a single magnetic domain [50,62]. To exclude this effect, only measurements up to an angle of 80° are incorporated in the fit.

[¶] In fact, the anomalous Hall effect is intimately related to the spin Hall effect (section 7.2.3), which describes transverse spin accumulation due to a charge current in a nonmagnetic material. In a magnetic material, this spin accumulation transforms into a real charge accumulation by spin-dependent scattering.

[‖] Superconducting Quantum Interference Device, a standard technique to measure small magnetic moments.

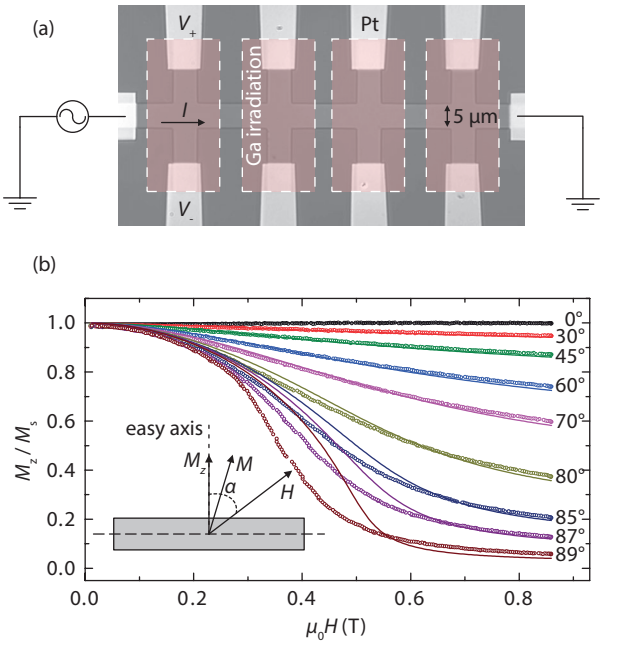

Figure 2.6 | (a) Pt/Co/Pt sample with four irradiated Hall crosses for AHE measurements; (b) Example of $M_z(H, \alpha)$ (open circles). The lines are the result of a global Stoner-Wohlfart fit for all α up to 80°. Higher α are not incorporated because of non-coherent magnetization reversal [62]. The inset shows the experimental geometry.

2.5.2 Anisotropy of Ga-irradiated Pt/Co/Pt

Figure 2.7 demonstrates the effect of Ga irradiation and Co layer thickness on the anisotropy of Pt/Co/Pt structures. First we discuss the influence of the Co layer. It is observed that the anisotropy increases if the Co thickness is reduced from 0.6 to 0.5 nm. This inverse dependence on t is expected, since K_{eff} arises from the surface anisotropy K_s at the Pt/Co interfaces via $K_{\text{eff}} = 2K_s/t - \frac{1}{2}\mu_0 M_s^2$ (combine (2.3) and (2.5)). However, the anisotropy of the 0.4 nm Co sample does not differ significantly from the 0.5 nm sample, meaning that growth-related phenomena are starting to play a role for such thin layers. Thinner layers are less well-defined and therefore the interface anisotropy will decrease; this transition occurs between 0.4 and 0.5 nm. This will also manifest itself in a significantly lower coercivity of 0.4 nm samples in section 2.6, again hinting to a more disordered layer with easy nucleation centers.

As a function of Ga dose, we see a decrease of K_{eff} that is approximately linear at low dose, and less steep at high dose. For higher doses than shown, the remanence at zero field was significantly reduced and the Stoner-Wohlfart model could not be applied. Eventually, the magnetization becomes completely in-plane (negative K_{eff}). This transition to in-plane magnetization occurs at higher dose if the Co layer is

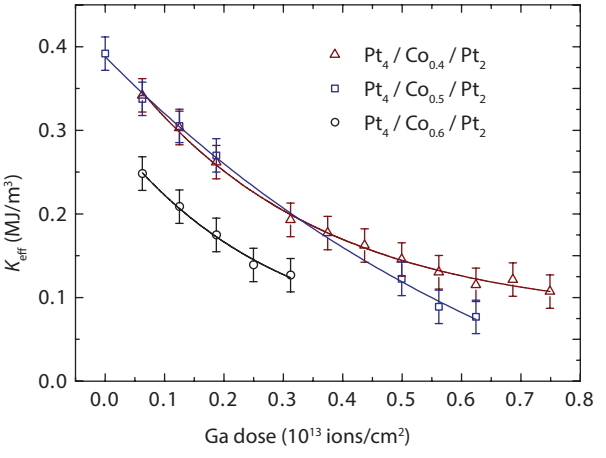

Figure 2.7 | The anisotropy constant K_{eff} as a function of the Ga irradiation dose for Pt/Co/Pt structures with varying Co thickness. The guides are exponential fits.

thinner, because the anisotropy is higher to begin with. From a practical perspective this is very interesting, because the range of Ga doses that can be applied to tune the anisotropy increases by more than a factor of 2.

Whereas the effect of Ga irradiation on the anisotropy is now quantified, the effect on other magnetic properties is not. However, we do not expect a very significant effect, since Ga irradiation mainly affects the interfaces and M_s and A are typically bulk parameters. The magnitude of the AHE signal is some measure of M_s, and we observed no trend as a function of Ga dose. Less is known about the effect on A, since this parameter is very difficult to measure, but at least such an effect is not needed for explaining the results in the remainder of this Chapter.

To conclude this section, it is seen that the anisotropy of Pt/Co/Pt samples increases for thinner Co layers, but this increase stops for very thin layers of < 0.5 nm. Interestingly, the reduction of anisotropy with low Ga dose remains constant irrespective of the starting anisotropy of the unirradiated film, i.e. the slope at low dose does not depend on the thickness in Figure 2.7. This is slightly counterintuitive, because if Ga irradiation reduces the surface anisotropy K_s by the same amount regardless of thickness, this would translate to a $1/t$ dependence of the slope of K_{eff}. From an experimental perspective this is a very useful result. By changing the Co thickness or the growth conditions, the tunable range of DW pinning fields can be expanded. In the next section 2.6 we will further investigate the consequences of this on the nucleation, pinning and injection of DWs in Pt/Co/Pt layers.

2.6 Controlling domain-wall nucleation and pinning

In the present section the effects of Ga irradiation on DW nucleation and pinning are investigated experimentally. First, the experimental method is described. In the subsequent sections, DW nucleation and pinning is investigated as a function of Ga

dose, strip width, Co layer thickness, and beam focus. It will turn out that both the height and the width of the DW energy barrier can be tuned by these parameters.

2.6.1 Experimental details

The investigated structures are rectangular Pt(4 nm) / Co(t nm) / Pt(2 nm) strips of $15 \times 2\,\mu m^2$, $10 \times 1\,\mu m^2$, $5 \times 0.5\,\mu m^2$ and $2.5 \times 0.25\,\mu m^2$. Different Co thicknesses $t = 0.4$, 0.5 and 0.6 nm are used. The structures are grown on a Si / SiO_2 (100 nm) substrate by EBL, sputtering, and lift-off.

After the fabrication of the Pt/Co/Pt layers, the left half of the strips is irradiated with Ga ions at a varying dose to reduce the anisotropy. Upon application of a magnetic field, a DW nucleates in this area and subsequently moves into the remainder of the strip. Wide-field Kerr microscopy (section 2.4.3) is used to study the effect of ion irradiation on nucleation and pinning of DWs. In the analysis we focus on the injection field H_{in}, defined as the external field at which the DW penetrates into the non-irradiated part of the structure. Since the injection of a DW involves two processes with a different typical field strength (nucleation at a field H_n and depinning at a field H_{pin}), the injection field is defined as the maximum of these two fields. The magnetic field is swept from negative to positive and a sudden change in intensity of the Kerr signal occurs in the non-irradiated area when the DW is injected. Decent statistics are obtained by averaging H_{in} over 12 structures. The error bars in all figures where H_{in} is plotted against the irradiation dose represent the standard deviation of H_{in} from structure to structure.

2.6.2 Variable Ga dose and strip width

First, the effect of Ga irradiation is studied on strips with a fixed Co thickness $t = 0.6$ nm. Figure 2.8 shows exemplary Kerr images of the switching process in several $10 \times 1\,\mu m^2$ strips. The Kerr images of three different Ga doses are shown. In Figure 2.9 the measured injection field is plotted as a function of Ga dose for structures of various sizes.

Here, we discuss the features observed in the Kerr images of Figure 2.8. The samples were saturated in a negative field and the field was swept to positive saturation. Snapshots at different positive fields during the sweep are shown. In Figure 2.8(a) (dose 0.34×10^{13} ions/cm^2), it is seen that at a certain field strength, the bright structures have switched completely while the dark structures have not. This is due to the statistical nature of domain nucleation in perpendicular materials, which occurs at random defects [64]. At a slightly higher field (Figure 2.8(b)), 2 more structures have switched instantly. This means that a DW was nucleated in the irradiated area, which instantly moves into the remainder of the strip. In other words, the nucleation field is much higher than the pinning field, $H_n > H_{pin}$. The range of doses where this is the case is denoted by A in Figure 2.9. Clearly, H_n decreases with Ga dose due to the PMA reduction.

In the snapshots taken at higher dose (0.41×10^{13} ions/cm^2) in Figure 2.8(c), it is seen that a DW which nucleated in the irradiated area pins at the boundary between the two regions in some strips. However, in other structures the DW moved instantly without pinning. This indicates that the field strengths associated with

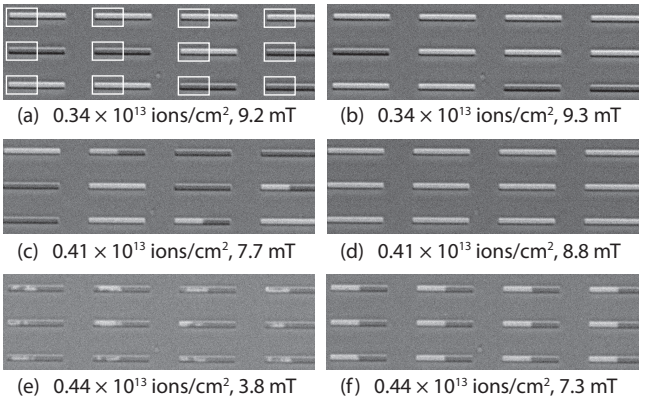

Figure 2.8 | Kerr microscopy images of the magnetic switching behavior of $10 \times 1\,\mu m^2$ Pt / Co(0.6 nm) / Pt structures for various doses of Ga irradiation. The irradiated regions are marked in (a). The magnetic contrast is enhanced by subtraction of a background image, which is obtained at zero field after saturation at high negative fields.

nucleation and pinning are approximately the same, $H_n \approx H_{pin}$. A significantly higher field is needed (Figure 2.8(d)) to depin all the trapped DWs.

Looking at a slightly higher dose of 0.44×10^{13} ions/cm^2 in Figure 2.8(e), a strong change in the nucleation of the DW is observed. Instead of the instantaneous switching that was observed before, the irradiated area now switches in many small domains, because we are getting close to the in-plane transition. By increasing the field as seen in Figure 2.8(f), a single domain will again appear and the corresponding DW is pinned for all structures at the shown field. Hence, $H_n < H_{pin}$. This regime is denoted B in Figure 2.9.

In Figure 2.9, H_{in} as a function of Ga dose is plotted for structures of different sizes. Next to the discussed regimes A ($H_n > H_{pin}$), B ($H_n < H_{pin}$), we identify a third regime C where the pinning field converges to an asymptote, because the magnetization of the irradiated region becomes in-plane. The same 3 regimes were found in the micromagnetic model depicted in Figure 2.2. For the strips of $15 \times 2\,\mu m^2$, $10 \times 1\,\mu m^2$ and $5 \times 0.5\,\mu m^2$ the behavior is very similar. The $2.5 \times 0.25\,\mu m^2$ structures, however, behave somewhat differently. Although all the observed features are still present, it can be seen that these structures have a significantly lower nucleation field in regime A. Since all structures are grown and measured under the same conditions on the same wafer, this effect must be related to the decrease in size. Indeed, due to the limitations of the lithography method used, the roughness of the strips is very significant compared to the strip width, resulting in a rather poorly defined strip. The nucleation field is very sensitive to structural defects and is therefore reduced, and also the anisotropy itself might be affected, leading to a change of the observed effects.

The magnitude of the injection fields is roughly a factor 20 higher in the simulations/1D model compared to the experiments. This is not unusual, since the simulations do not include any thermal fluctuations. In room temperature exper-

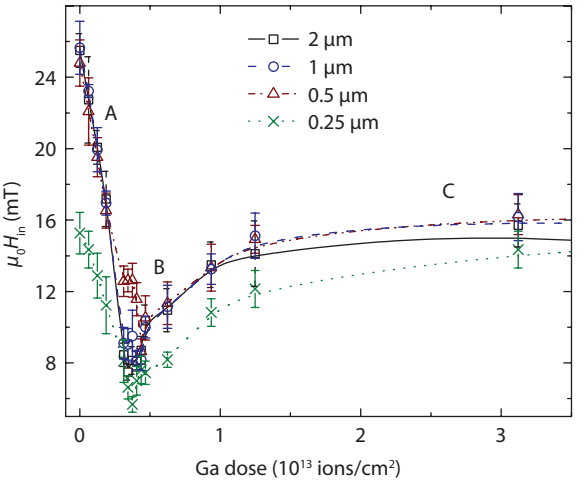

Figure 2.9 | DW injection field as a function of Ga dose for a Pt/Co(0.6 nm)/Pt strip of variable width. The lines are drawn as a guide to the eye.

iments, thermal fluctuations play a crucial role in all magnetization reversal phenomena [64]. For example, the coercive field (responsible for the injection field in the high-K range) is greatly reduced at finite temperatures, and originates from the nucleation of a small area followed by DW motion, instead of the Stoner-Wohlfart type of switching in our model. In SQUID measurements, it was found that for a similar film, the coercivity at 5 K is roughly 40 times larger than at room temperature. Also, the escape of a DW over an energy barrier (responsible for the DW injection in the low-K region) is much easier at elevated temperatures, so lower fields are required for depinning. Therefore, only a qualitative comparison with the micromagnetic model can be made.

2.6.3 Variable Co layer thickness

Figure 2.10 shows a comparison of H_{in} as a function of Ga dose, this time for different Co thicknesses in Pt / Co (t nm) / Pt structures of $10 \times 1\,\mu\mathrm{m}^2$. The $t = 0.4$ nm structures clearly have a lower nucleation field. This is probably related to the growth quality of such ultrathin films. Interestingly, the pinning strength is very similar for the 0.5 and 0.6 nm Co thicknesses. This is also what would be expected from the anisotropy measurements of Figure 2.7, because $K_{\mathrm{eff},0} - K_{\mathrm{eff}}$ appeared to be rather insensitive to the layer thickness. The minimum of the curve, where $H_{\mathrm{pin}} = H_{\mathrm{n}}$, is found at a dose of 0.44×10^{13}ions/cm^2 for both the 0.5 nm and 0.6 nm strips. For the 0.4 nm structures H_{n} is lower (related to the growth quality of such thin layers), which shifts the minimum slightly to the left at 0.31×10^{13}ions/cm^2. Also, the DW pinning in regime B is lower for the 0.4 nm strips, because the anisotropy is better retained at high doses compared to the 0.5 nm sample (as seen in Figure 2.7), leading to a lower pinning barrier. In the high-dose regime

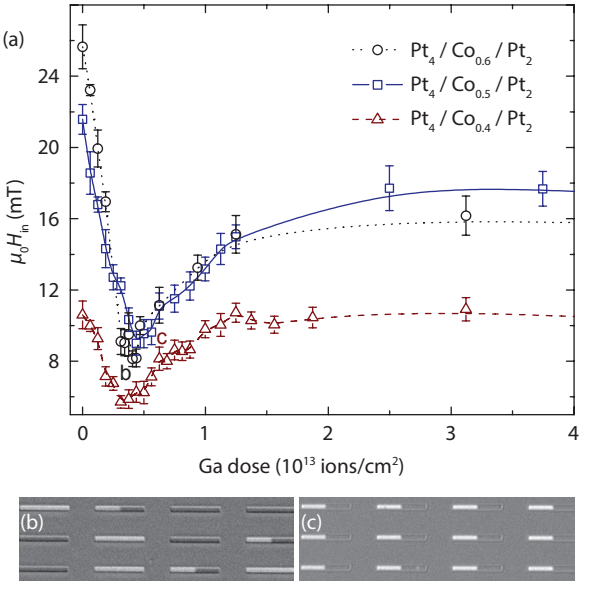

Figure 2.10 | (a) DW injection field in 1 μm wide strips as a function of Ga dose for different Co thicknesses. Kerr snapshots of (b) 0.6 nm and (c) 0.5 nm structures at the highest dose that retains full remanence, demonstrating that pinning is better tunable in a thinner Co layer.

(C), where the irradiated region has an in-plane magnetization, H_{pin} is theoretically given by $K_{\text{eff},0}/(\mu_0 M_s)$, so ultimately determined by the anisotropy of the untouched part $K_{\text{eff},0}$. Both $K_{\text{eff},0}$ and H_{pin} are significantly higher for the 0.5 nm Co film, demonstrating that the theoretical model appears to have qualitative validity also in this regime. For the 0.4 nm Co film, the pinning field at high dose is masked by the very low H_n.

Compatible with the anisotropy measurements in Figure 2.7, it is seen from the Kerr images that for thin Co layers, much larger anisotropy differences can be obtained before the magnetization becomes in-plane. Because theoretically $H_{\text{pin}} = (K_{\text{eff},0} - K_{\text{eff}})/(\mu_0 M_s)$ this means that the pinning strength of the anisotropy barrier can also be made much stronger. Decreasing the Co thickness therefore leads to more controllable DW pinning. This is illustrated by Figure 2.10(c), which shows that DWs are consistently pinned in the 0.5 nm Co strip for all the studied structures at the shown dose of 0.56×10^{13} ions/cm^2. At the same dose, the 0.6 nm Co strip is already in-plane magnetized. The highest dose where the 0.6 nm strips are fully perpendicular is 0.41×10^{13} ions/cm^2, and Figure 2.10(c) illustrates the unreliable pinning in these strips. For application as pinning sites, one typically would like to pin an existing DW without risking nucleation of a new DW. Therefore, one would require a significant 'gap' between the highest H_n and the lowest H_{pin} of any of the structures. For the 0.6 nm Co, this gap is virtually zero for any dose that retains full remanence. For 0.5 nm, the gap is maximized at 0.56×10^{13} ions/cm^2 and 0.8 mT

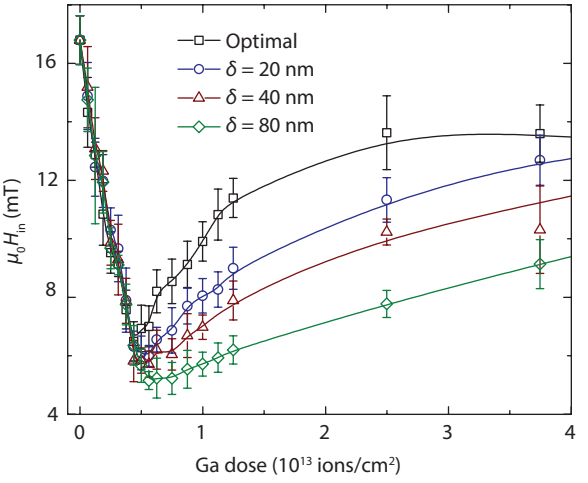

Figure 2.11 | DW injection field of 1 μm wide Pt / Co(0.5 nm) / Pt structures. The width of the anisotropy barrier δ is controlled by changing the focus of the ion beam. As expected, the pinning strength is reduced for increasing δ.

in size. Interestingly, for the 0.4 nm strips, full PMA extends to very high doses and the optimal gap was 4.7 mT at a dose of 0.81×10^{13} ions/cm^2.

2.6.4 Tuning the width of the pinning barrier

In the previous sections, we showed that the DW pinning field at a Ga irradiation boundary scales with $K_{\text{eff},0} - K_{\text{eff}}$, where $K_{\text{eff},0}$ can be tuned by the Co interlayer thickness and K_{eff} by the Ga dose. However, (2.14) suggests another parameter to tune the pinning field: the length scale of the anisotropy gradient δ. It is expected that the pinning strength decreases with increasing δ, because the energy barrier for DW propagation becomes less steep. Experimentally, δ is controlled by placing the sample away from the focal point. The distance to the focal point determines the FWHM of the beam, which is used as an estimate of δ.

Figure 2.11 illustrates the behavior of the injection field in Pt / Co (0.5 nm) / Pt as δ is varied from 0 (optimal beam focus) to ~ 80 nm. Increasing δ clearly leads to a systematic decrease of H_{pin}. The qualitative agreement with the theoretical result of Figure 2.2 is striking. The fact that a slight change of δ leads to such clear effects is strong evidence that Ga irradiation creates pinning sites at a length scale comparable to the DW width. It is interesting to note that the minimum in H_{in} is also reduced when increasing δ. A lesson to learn from this, is that in order to achieve DW injection at the lowest possible field, one should simply make δ as big as possible. This trick can be useful in experiments, if the goal is to easily create a single DW that moves in a well-defined direction through the nanostrip. For example, we will use it in Chapter 6 to introduce a DW at low field, which is subsequently stopped by an external magnetic nanopillar, of which we want to investigate the ability to pin DWs.

2.6.5 Better tunability using He ions

In the results presented so far, we employed Ga ions to locally reduce the magnetic anisotropy. The choice to use Ga is mainly governed by the wide commercial availability of *focused* Ga beams. However, other ions such as He have also already been used [45,47], but never in a focused variety. Very recently, Helium Ion Microscopy (HIM) systems have become commercially available, using a focused He beam that has several advantages for imaging and nanostructuring, the most notable advantage being the sub-nm resolution [65,66]. As an alternative to Ga FIB, where we really operate at the low-dose limit of the machine, we report here on the first use of a focused He beam to alter magnetic properties. We notice a significantly improved control of DW injection and pinning as compared to a conventional Ga FIB.

To perform the He-irradiation experiments, we have used the exact same $t = 0.6\,\text{nm}$ sample as before in section 2.6.3. In collaboration with TNO in Delft, a Zeiss Orion Plus helium ion microscope was employed, operating at 25 keV at a beam current of 1.5 pA, which is close to the upper limit of this machine, whereas this is the lower limit of our Ga FIB. Analogously to the Ga experiments, the dose is varied with hopes of observing a similar trend in the DW nucleation and pinning properties.

In Figure 2.12(a), we compare the results of Ga and He irradiation, both at optimal beam focus. We have plotted the data on the same axes by scaling the doses to obtain overlap in regime (A), because this regime is believed to scale linearly with the anisotropy. It is then clearly observed that the pinning field in regime (B) is significantly higher for the He irradiated structures. The much steeper pinning field observed at the He irradiation boundary is thus evidence for a much smaller gradient length δ, due to a much finer beam spot. This point is highlighted by the Kerr microscopy snapshots in Figure 2.12(b): there is a finite field range for which all DWs are both nucleated and pinned, whereas the equivalent Ga dose in Figure 2.12(b) shows that some DWs can already depin before other ones are even nucleated, due to the weaker pinning. Also shown are the results of an intentionally blurred Ga beam in this sample (dashed line in Figure 2.12(a)), again confirming that the slope is related to the beam focus.

We can obtain a crude estimate for the length of the anisotropy gradient at the boundary in case of Ga and He beams. The slope of the pinning regime (B) should decrease with the gradient length δ according to (2.14). We estimate this slope by a straight line through the origin and the onset of the pinning regime. By assuming a DW width of 10 nm (estimated from the micromagnetic simulations) and assuming that the gradient length at the He-irradiated boundary $\delta_{\text{He}} < 5\,\text{nm}$ (which is realistic given the $< 1\,\text{nm}$ imaging resolution), it follows that $\delta_{\text{Ga}} = 22\,\text{nm}$. The damage radius of the He beam causing the anisotropy reduction might thus be an order of magnitude smaller, allowing engineering of magnetic properties at the $< 10\,\text{nm}$ scale.

Looking at the magnitude of the Ga and He doses in Figure 2.12(a), one can see that a factor 700 more He ions are required in order to have the same reduction in perpendicular anisotropy. This is an inherent advantage when very subtle control of the anisotropy is required. The dose is controlled by the product of the beam current and pixel dwell time and both are at the lower limit for the Ga doses used

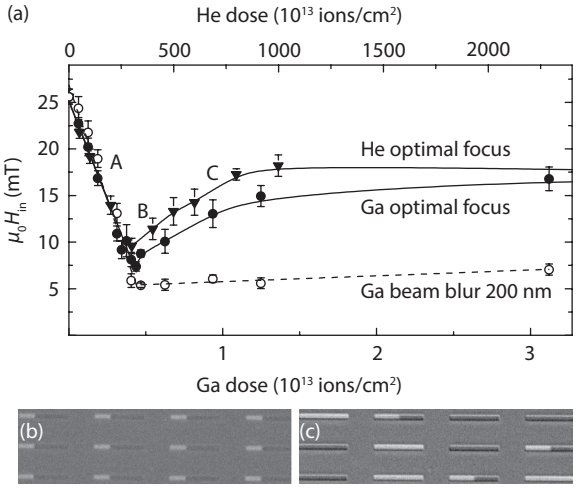

Figure 2.12 | (a) Injection field as a function of dose for He (triangles), Ga (solid circles) and blurred Ga (open circles) irradiation. The line is a guide to the eye. (b) 12 identical He irradiated structures (300×10^{13} ions/cm^2) at 7.5 mT, consistently having a pinned DW (c) Ga irradiated structures (0.41×10^{13} ions/cm^2) at 7.5 mT, where some DWs are already depinned while others are not yet nucleated.

here, so that more subtle modifications are not viable. In fact, it is not even possible to use the Ga beam for imaging purposes since that would completely destroy the PMA, which is not the case for He beam imaging. However, in the remainder of this thesis we will still use Ga irradiation, simply because it is available in our own laboratory.

2.7 Conclusion

In this Chapter, we analyzed in detail the pinning of a DW at engineered anisotropy variations. First, we analytically derived that a step in the magnetic anisotropy acts as an energy barrier for the DW. It was shown that the pinning field of a DW at such an anisotropy boundary increases with the anisotropy difference and decreases with the width of the boundary. The analytical model matches well with micromagnetic simulations. Then, it was shown that FIB irradiation with Ga ions can be used to control the magnetic anisotropy of a Pt/Co/Pt strip, and quantitative measurements were performed using the AHE. Thereafter, field-induced DW pinning and nucleation in irradiated Pt/Co/Pt nanostrips was studied using wide-field Kerr microscopy. The pinning behavior qualitatively reproduced all the features of the analytical model. The pinning of DWs was shown to be insensitive to the width of the strip in the range 0.5-2.0 μm. However, the thickness of the Co layer does provide another handle to tune DW pinning, since a thinner Co layer has higher intrinsic anisotropy, thereby increasing the possible anisotropy step that can be realized without destroying the PMA at the irradiated side. Finally, it was shown that

even the width of the anisotropy barrier, which according to our model has to be of the order of the DW width ($\sim 10\,\text{nm}$), can be precisely tuned by reducing the focus of the ion beam. This leads to a lower injection field because the energy barrier for the DW becomes less steep. However, if strong pinning is required, we found it is better to use a focused He beam instead of Ga, since the finer beam spot leads to a steeper energy barrier.

Engineered anisotropy defects can not only be used to controllably inject a DW at arbitrarily low fields, but also to provide tunable pinning sites for field- and current-induced DW motion in PMA strips. In the experiments reported in this Chapter, relatively large areas were irradiated with Ga, but also small defects could be made that act as pinning sites in the sense of Figure 1.4(a) in the introduction. These can be useful in DW-based memory or logic devices as an alternative to geometrically induced pinning sites [7,32,33], or for controlled experiments on current-induced DW depinning. To conclude, control of the magnetic anisotropy at the nanoscale is a powerful tool in many magnetic nanodevices. In fact, we will use it extensively throughout both parts of this thesis. Below, we present an outline of the remainder of Part I, to which this Chapter formed the introduction.

2.8 In this Part

In this Chapter, we have introduced the basic experimental and theoretical concepts that form the foundations for the work in this thesis. As mentioned in the general introduction, the goal of Part I is to **explore various new approaches to realize DW pinning**, and take these a step further to demonstrate **novel device applications**. One of the new approaches to DW pinning, by using ion irradiation, was already studied in detail in the current chapter. We now briefly introduce the other chapters that together make up Part I.

In the next **Chapter 3**, we will use our ability to locally change the anisotropy to generate a sawtooth-like DW energy potential along a nanostrip. Due to the asymmetric shape of this potential, the DWs experience a different pinning strength in the two possible directions of motion. By applying an alternating magnetic field, DWs will effectively move in a well-defined direction, even though the time-average magnetic field is zero. More importantly, we show that two neighboring DWs move in the *same direction*, hence we have created a kind of racetrack memory that operates with a magnetic field rather than electric current. This is interesting, because it is generally perceived that a magnetic field cannot be used for coherent DW motion, since they push neighboring DWs in opposite directions. We call this concept *DW ratchet memory* and demonstrate a proof-of-principle experiment of two DWs propagating around a ring-shaped nanostrip without annihilating.

In **Chapter 4**, we study DW pinning at an anisotropy barrier in a completely different context. This chapter applies DW dynamics to a related subfield of spintronics: that of spin-transfer oscillators (STOs). In this subfield, researchers try to create a nano-sized, tunable source of radio frequency (RF) signals, by making use of current-induced oscillations of magnetic nano-objects. Typically, these oscillations are excited in a multilayer nanopillar geometry by a vertical DC current. In Chapter 4, however, we theoretically consider the angular precession of a magnetic

DW pinned at an anisotropy barrier, excited by a *longitudinal* DC current. The use of DW oscillations for this purpose has been proposed before [67–69], but we argue that our specific scheme adds additional tunability to previous proposals.

In **Chapter 5**, we will explore an alternative approach to creating a pinning site. It is based on an emerging topic in spintronics, where *electric* fields are used to tune the magnetic properties. As briefly discussed in section 2.2.2, the perpendicular magnetic anisotropy originates from the electronic structure at the interfaces. It is therefore not surprising that adding charges to such an interface, changes the electronic interactions, and thereby alters the magnetic anisotropy. This is exactly what is used in Chapter 5. A voltage applied across a dielectric on top of a nanostrip is used to *temporarily* induce a step in the anisotropy, similar to a pinning barrier induced by Ga ions, but with the great advantage that it is non-permanent and re-programmable. The ability to remove a pinning site when desired can potentially reduce the power consumption of racetrack memory, besides being useful in other device applications.

In **Chapter 6** we study another, perhaps slightly more exotic, way to pin a DW. Vertical iron nanopillars are grown on top of a Pt/Co/Pt nanostrip by a technique called Focused Electron Beam Induced Deposition. This method can be regarded as 3D-printing on the nanometer scale. A precursor gas consisting of $Fe_2(CO)_9$ is released in the vacuum of our electron beam system, and the gas is dissociated by the electron beam, leaving behind an Fe-rich deposition on the substrate. Because the electron beam can be directed as desired, 3-dimensional shapes can be constructed. A straightforward 3D shape is a nanopillar with a diameter smaller than 100 nm, and we use the magnetic stray fields generated by these pillars to pin a DW in an underlying nanostrip. At the same time, the pinning behavior of the DWs in the nanostrip yields information on the magnetic properties of individual nanopillars.

Field-driven domain-wall ratchet memory

3

The movement of magnetic DWs can be used to build a device known as a shift register, which has applications in memory[7] and logic circuits[35,70]. However, the application of magnetic DW shift registers has been hindered by geometrical restrictions, by randomness in DW displacement, and by the need for high current densities or rotating magnetic fields. Here we propose a new approach in which the energy landscape experienced by the DWs is engineered to favor a unidirectional ratchet-like propagation. The DWs are defined between domains with an out-of-plane (perpendicular) magnetization, which allows us to route DWs along arbitrary in-plane paths using a time-varying applied magnetic field with fixed orientation. In addition, this ratchet-like motion causes the DWs to lock to discrete positions along these paths, which is useful for digital devices. As a proof-of-principle experiment we demonstrate the continuous propagation of two DWs along a closed-loop path in a Pt/Co/Pt strip.*

3.1 Introduction

Although magnetic shift registers were already considered in the 1970s[71,72] and abandoned later on, exciting developments in spintronics have led to nanometer-sized versions which are very actively investigated. A prominent example is the magnetic racetrack memory[7], where magnetic DWs are driven by current instead of magnetic fields. One of the main motivations to use current rather than a magnetic field is that two neighboring DWs will move towards each other when a field is applied, annihilating any data stored. But sending large currents through tiny wires brings about practical issues, primarily related to heating[73]. Alternatively, the 'DW logic' scheme[35,70] uses a carefully shaped permalloy track capable of storing, moving and performing logic operations on magnetic DWs, using in-plane rotating magnetic fields as a clock. But this scheme imposes very strong geometrical constraints and rotating in-plane fields are particularly hard to integrate into a chip.

*Published as: *Shift registers based on magnetic domain wall ratchets with perpendicular anisotropy*. J. H. Franken, H. J. M. Swagten, and B. Koopmans, Nature Nanotechnology **7**, 499 (2012).

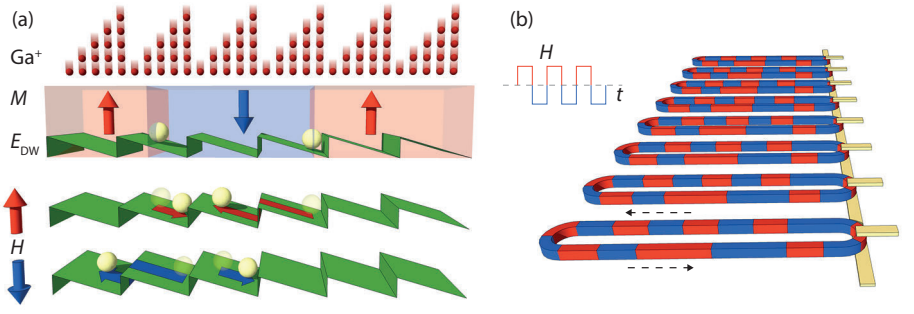

Figure 3.1 | Domain-wall ratchet shift register. (a) A magnetic nanostrip with perpendicular magnetic anisotropy exhibits magnetic domains with a net magnetization (M) pointing up (red) or down (blue). The energy landscape E_{DW} (green) experienced by the DWs (yellow beads) can be engineered by irradiating the strip with gallium ions (Ga^+) of varying intensity. The force exerted on the DWs by a positive (red) applied magnetic field (H) pushes the DWs together, while a negative (blue) field pushes them apart. By applying a positive and then a negative pulse of the appropriate duration, both DWs move to the left. (b) Possible implementation in a memory device. Loops are used to conserve the data indefinitely. One could either use a global magnetic field for all loops, or address each loop individually. Data input/output can be integrated, for example, by placing a magnetic tunnel junction (MTJ) at a single position along each track, where the track acts as free layer. Alternatively, writing schemes involving the magnetic field can be devised, for example by engineering a position where the DW nucleation field is reduced, such that a brief increase in the field amplitude can write a bit at this position.

Our approach makes use of materials with PMA, which is advantageous to in-plane materials because they exhibit narrow DWs ($\sim 10\,\mathrm{nm}$) occupying less space. The key is to create a DW ratchet, i.e. we should ensure that a DW moves easily in one direction whereas motion is blocked in the other direction[74–80]. Some ways to achieve this have been proposed for in-plane magnetized systems, for example by using the stray field of nearby magnetic elements[79,80], non-uniform transverse magnetic fields[81], or geometrical variations[74–76]. However, these effects are rather weak compared to the strong anisotropy field in PMA materials. In order to carefully control DW motion in PMA ratchets, we choose to engineer the DW energy landscape directly by modulating the magnetic anisotropy. Ion irradiation using a focused ion beam (FIB)[44,45] provides an elegant way to tune this parameter on a nanometer scale[24,49,82]. The ion irradiation pattern on a magnetic nanostrip is sketched in Figure 3.1. Higher irradiation doses lead to lower PMA and therefore a lower DW energy, giving the desired sawtooth-like potential landscape for the DWs. When a positive field is applied, a force is exerted on the DWs pushing them towards each other to minimize the Zeeman energy $-\mu_0\mathbf{M}\cdot\mathbf{H}$. However, the sudden step in the anisotropy provides an energy barrier, prohibiting the left DW from moving to the right. By proper timing of the field pulse, the right DW will move to a position within the next ratchet period. A subsequent opposite field pulse will move this DW back to its new base position, while the left DW will propagate.

As long as the distance between two DWs is at least two periods, an AC field can be used for propagating both DWs in the same direction, at the same time providing discrete positions where the DW will stop which is crucial for a digital device. To prevent data loss at the ends of the strip, one simply makes a loop in which data can propagate indefinitely.

This scheme has some unique and powerful advantages for implementation in a memory device. Because the magnetization is perpendicular to the plane, we have complete freedom to route our DWs within the film plane, for example creating loops to propagate the data indefinitely. In contrast to in-plane rotating fields [35], a perpendicular magnetic field is easy to produce, for example by the Oersted field of current lines coplanar to the magnetic structure. A possible implementation in a 2D memory architecture, including read and write access, is presented in Figure 3.1(b). In this Chapter we focus on the principal ingredient for this device, which is the demonstration and understanding of unidirectional propagation of multiple DWs.

3.2 Experimental demonstration

A first test of this working principle is presented in Figure 3.2(a). After preparing a DW in a patterned Pt/Co/Pt strip, sinusoidal pulses with amplitude 6 mT and period $T = 50$ ms are applied while the magnetic state is imaged after each pulse. The DW, initially at $x = 0$, moves a distance $-5\,\mu$m by each pulse, corresponding to the period and direction of the ratchet landscape. This illustrates that we have successfully created a ratchet: the time-average magnetic field is zero, but still the DW moves to the right and locks to discrete energy minima after each pulse. Figure 3.2(b) shows the DW position as a function of pulse number, under variation of pulse duration. Optimal motion over 4 periods is observed for $T = 50$ ms. After 4 periods the DW is blocked by a random pinning site and does not easily move beyond -20 μm.

To elucidate the different effect of positive and negative fields on DW propagation, measurements with unipolar field pulses were also performed. In Figure 3.2(c), low field pulses of 5.25 mT were applied in the easy propagation direction. Rather than reverting to the engineered energy minima, the DW stays at arbitrary positions after each pulse, due to the random pinning potential of the material which is superposed on the engineered potential. In Figure 3.2(d), a significantly higher opposite field of -6.75 mT is applied in order to move DWs against the ratchet direction. As expected, the DW now tends to stop at discrete pinning positions that block its motion.

We now apply the demonstrated ratchet functionality in a shift register, where it is vital to propagate multiple DWs without annihilation. Therefore, we created ring structures consisting of 8 ratchet periods, and study the simultaneous motion of 2 DWs around the ring (Figure 3.3). Instead of defining the rings lithographically, we employ a unique technique which we call magnetic etching (see methods section 3.5). After nucleating a pair of DWs, field pulses of alternating polarity are applied and the configuration is imaged after each pulse in Figure 3.3(b). It is observed that each time, one of the DWs moves counterclockwise to a position within the next segment, whereas the other DW locks back to the base position of the current

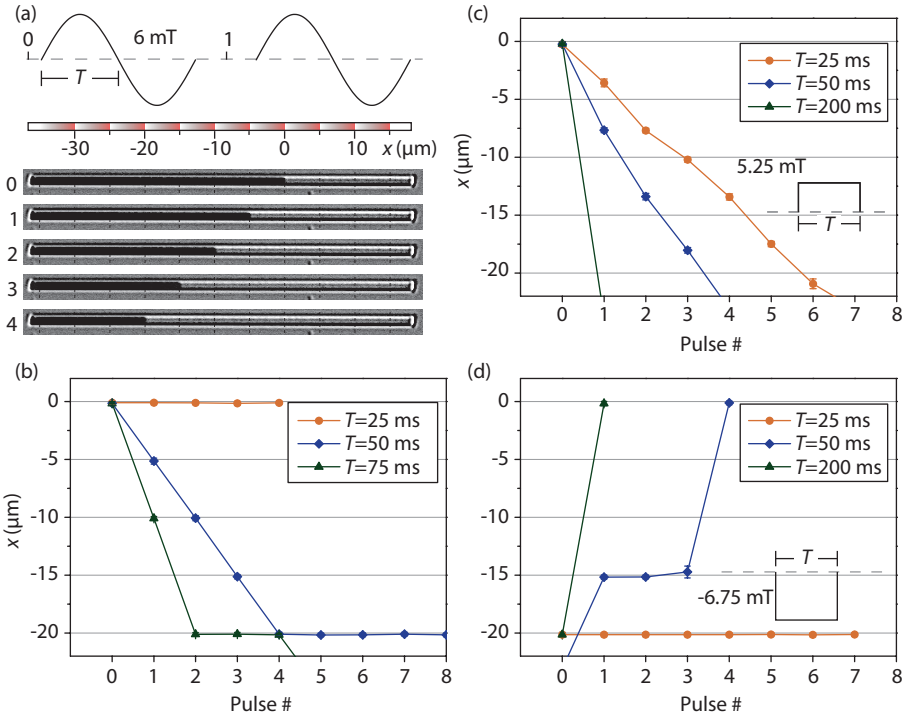

Figure 3.2 | Demonstration of the ratchet effect in a Pt/Co/Pt strip. (a) a 1 μm wide strip is patterned with a linearly increasing Ga irradiation dose (red means maximum) in 5 μm long periods. Kerr microscopy snapshots are taken in between 6 mT sinusoidal field pulses with a half-period $T = 50$ ms (defined in the inset). (b) DW position as a function of pulse number with varying pulse durations. The different effect of positive and negative field pulses is illustrated in (c) and (d). In (c), it is shown that the DW pins at a random position after each positive field pulse. A much higher negative field was necessary in (d) to have any DW motion, and the DW position clearly locks to the steep energy barriers.

segment. The detected positions of both DWs are plotted as a function of pulse number in Figure 3.3(c). The DWs complete two full loops around the track without annihilating, demonstrating the feasibility of our approach.

3.3 Performance statistics

The performance statistics of one ratchet ring are studied as a function of the pulse parameters in Figure 3.4. By separating the statistics of forward and backward motion, we can identify the forward motion as the bottleneck in ratchet performance; the success of backward motion is close to unity in the entire parameter range (Figure 3.4(b)). Averaged over all events, an optimal forward success ratio of approximately 80% is observed in Figure 3.4(a). As expected, the optimal length of the field pulse decreases as the field amplitude is increased. The maximum average success is limited to 80% due to random growth variations in the sample,

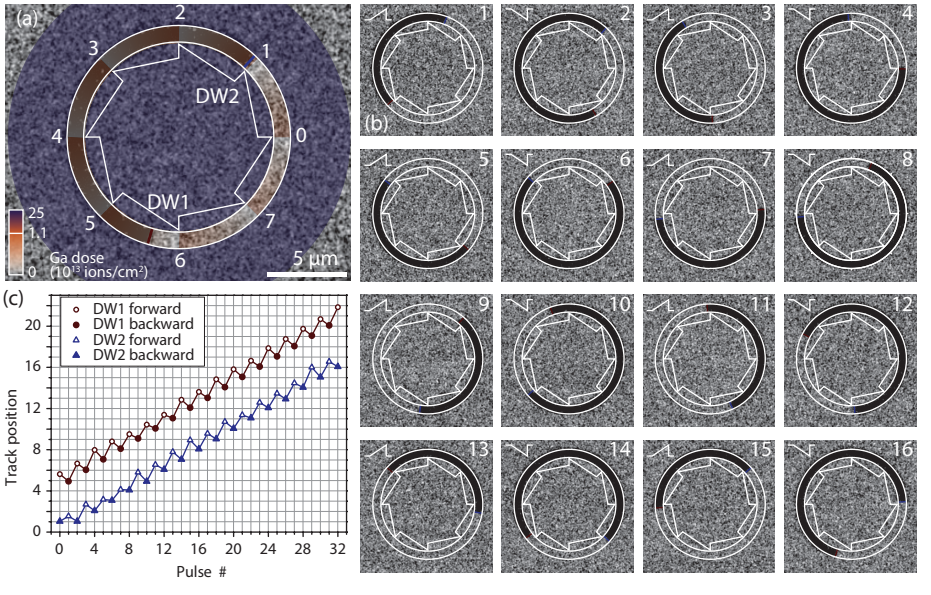

Figure 3.3 | Proof of principle operation of two DWs in a circular loop. (a) FIB-only patterning is used to define both the magnetic loop (high dose irradiation of the surroundings) and the 8 ratchet potentials within the loop (low dose variations). The initial positions of the DWs after a preparation pulse are shown in the underlying Kerr image. (b) Magnetic state and fitted DW positions after subsequent positive and negative ramped field pulses of 15.8 mT and 73 ms. The background of the positively saturated remnant state was subtracted from the Kerr images to improve contrast. (c) DW position as a function of pulse number showing near perfect discrete propagation of both DWs over 2 full loops.

leading to slightly different optimal pulse parameters for each of the 8 individual ratchets. There are also some ratchets that have lower success over the entire parameter range, for example by a relatively strong naturally occuring pinning site that hampers forward motion. In Figure 3.4(d,e), it is shown that both the forward (d) and backward (e) success rate of a selected single ratchet segment (indicated in the insets) can be brought close to unity. Therefore, limited success is not a principal problem but is rather a matter of engineering the material such that all ratchets show larger overlap in their operating range.

The combined forward/backward success plotted in Figure 3.4(c) closely resembles the forward statistics in Figure 3.4(a), as expected given the high success of backward motion. The optimal period as a function of amplitude fits well to a power law (see methods section 3.5). Figure 3.4(f) shows the average distance d (expressed in number of ratchet periods) traversed by a DW during a forward pulse, where a darker color means a larger distance. It is seen that if the field pulse is too long or high, the DW can move on average by more than 2 periods, which means a ratchet period is skipped. We find that over the entire field range, success is optimal if the pulse length is tuned to move the DW (on average) by $d \approx 1.5$,

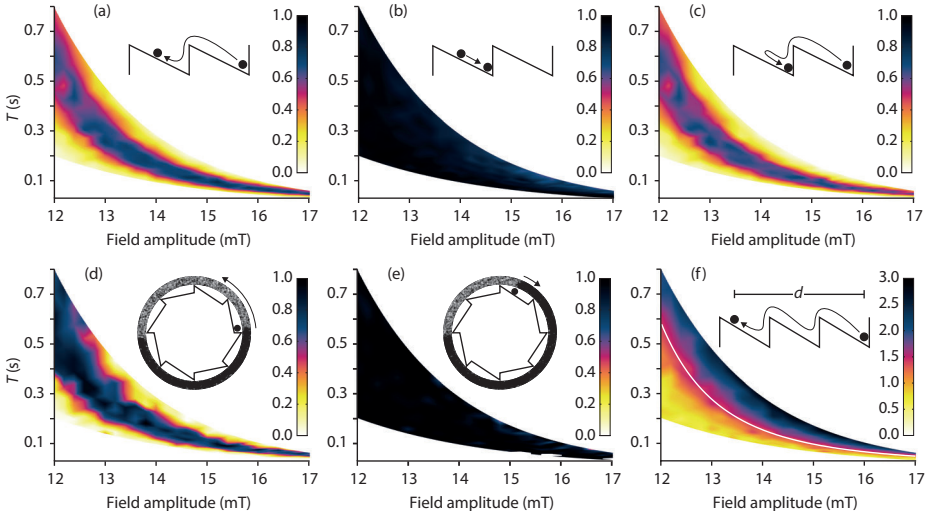

Figure 3.4 | Statistics of ratchet operation as a function of pulse duration and amplitude. (a) Success ratio of forward DW displacement to a position within the next ratchet period, averaged over all measured events. (b) Success of backward DW motion; in nearly all cases the DW locks to the base of the period where it was in. (c) Composite success of both forward and backward motion after a pair of positive and negative pulses. The statistics are clearly dominated by the success of forward motion. The white line is a fit through the optimal points. (d,e) Similar to (a,b) but only showing the statistics of motion of one selected ratchet segment on the ring (defined in the insets). (f) Average distance traveled by a DW due to a forward pulse. The color code here represents the number of ratchet periods d over which the DW moved. The white line representing optimal success coincides with a distance of $d \approx 1.5$ periods over the entire parameter range.

which is intuitive since this average DW displacement coincides with the center of the success range ($1 < d < 2$).

3.4 Conclusion

In conclusion, we have experimentally demonstrated a field-driven DW shift register by engineering a ratchet potential in a Pt/Co/Pt nanotrack. The demonstration of unidirectional DW motion changes the current paradigm, which excludes simple magnetic fields as a driving force. Furthermore, in most of the reported work on (current-driven) DW motion, the DW positions are random, whereas DWs efficiently lock to discrete positions in our scheme. However, the data rate of a future memory device is limited by the DW speed divided by the ratchet period. In our proof-of-principle experiment, DW speeds were limited to $\sim 100\,\mu$m/s by the slow electromagnet that was used, but fast motion > 100 m/s is feasible simply using higher, shorter pulses in order to change from the creep to the flow regime of DW motion [83]. To confirm that the principle still holds in this regime, a micromagnetic simulation was performed on a nanostrip with a ratchet period of 100 nm, with 8 ns

field pulses of 50 mT yielding stable ratchet operation. †. Like any DW shift register, the bit size is ultimately limited to a few times the DW width to ensure a stable configuration (so $\sim$ 50 nm in Pt/Co/Pt). Field-driven memory has many advantages, like a potentially low power dissipation per operation [70] and much longer device lifetime, which is limited by electromigration when charge currents are used. However, the discrete nature of our device is also beneficial when any other driving force is used, and could as well be applied in current-driven shift registers using spin transfer torque or recently discovered spin-orbit torques [84,85] (the topic of Part II). Using AC currents, the induced torques could lead to ratchet propagation of DWs in a fixed direction between two contacts. Here, it would be especially powerful if one could invert the ratchet direction during operation, so the bits can simply be shifted back and forth past a central reading head. This requires a programmable DW energy landscape, which could be realized using recently demonstrated electric field control of DW motion [86], and a simple programmable pinning site will be demonstrated in Chapter 5. Another interesting next step is to integrate logic functionality similar to the in-plane DW logic scheme [70], to create a fully magnetic memory and logic device from PMA materials. Apart from computer-related applications, the stray fields of propagating DWs could also be used as a particle conveyor belt in chemical/biosensors [87,88].

3.5 Methods

Ratchet strips: The 1 µm wide Pt (4 nm) / Co (0.5 nm) / Pt (2 nm) strips of Figure 3.2 were produced by e-beam lithography, sputtering and lift-off, followed by a Ga-FIB irradiation step. The perpendicular anisotropy of this material as a function of Ga dose was measured in Figure 2.7. The Ga dose was increased from 0.05×10^{13} ions/cm^2 to 0.5×10^{13} ions/cm^2 over a distance of 5 µm. This optimal Ga dose range is a balance between a sufficiently high anisotropy step to achieve DW pinning, while maintaining a high enough nucleation field to prevent spontaneous nucleation of domains by propagation pulses. To initialize a DW, a short high negative field pulse is applied to a positively saturated strip, which reproducibly creates the configuration seen in the first Kerr microscope image.

Ratchet rings: For the ratchet rings, we started from an unpatterned Ta (15 nm) / Pt (4 nm) / Co (0.5 nm) / Pt (4 nm) film, where the thick Ta seed layer serves to improve the growth quality, significantly increasing the range of Ga doses that can be applied before the perpendicular magnetization is destroyed. Here we employed a technique which we call magnetic etching, which allows us to fabricate devices simply from a homogeneous film in a single Ga-irradiation run. A magnetic ring is 'etched' by irradiating the surroundings (dark purple region in Figure 3.3) with

†A video of this micromagnetic simulation is available at http://goo.gl/bSaEll. Shown is the time evolution of the three magnetization components in a $600 \times 60 \times 1$ nm strip subjected to an AC block pulse with a time period of 8 ns. The following material parameters were used: exchange constant $A = 16$ pJ/m, saturation magnetization $M_s = 1400$ kA/m. The uniaxial anisotropy decreases from 1.5 MJ/m^3 to 1.2 MJ/m^3 in periods of 100 nm, yielding a DW energy landscape schematically sketched at the top. The precessional motion of the DWs in the XY plane indicates motion above the Walker breakdown field. Periodic boundary conditions were used in the horizontal direction.

a relatively high Ga dose of 25×10^{13} ions/cm^2, enough to destroy the magnetic anisotropy, but not enough to physically remove a significant amount of material. Within the ring, a much lower dose is used which linearly increases from 0.02 to 1.1×10^{13} ions/cm^2 in each of the eight segments in the clockwise direction, favoring DW propagation in the counterclockwise direction. This pattern is designed using line segments of constant dose pointing radially outward, separated by 40 nm. In principle, this yields a slightly higher dose in the inner boundary of the ring compared to the outer boundary, as the distance between the dose lines is smaller closer to the center. A preparatory pulse now creates two DWs at random positions. The sequence of 32 field pulses, as used in Figure 3.3, was repeated for 286 period/amplitude combinations, and each combination is repeated 10 times. This yielded nearly 100000 images of which the DW positions were detected using a MATLAB script. From this list of DW positions, we were able to track the distance moved by the DWs after each pulse and determine whether de DW behavior was successful or not (Figure 3.4). Forward success is defined as motion to a position within the the next ratchet period. Backward success means that a DW stays within the current ratchet period by a backward directed field pulse. Composite success means that a DW subsequently experienced successful forward and backward motion. For optimal success in the ratchet rings, longer pulses or higher field strengths are required compared to the experiment on straight strips shown in Figure 3.2. This is due to the different material used (the Ta seed layer increases the anisotropy which decreases the DW speed in the creep regime), the ramped pulse shape (where the maximum field strength is applied only very briefly), and possibly by the different lithography method (EBL versus FIB magnetic etching).

Power-law fit: The fit through the optimal period as a function of field amplitude (white line in Figure 3.4(c)) is of the form $T_{\text{opt}} \propto e^{CH^{-\mu}}$, with $\mu = 2.2$. It is hard to ascribe a physical mechanism to the exponent μ. For DW motion under a constant field through a uniform medium, $\mu = 0.25$ is expected in the low-field creep regime[83,89]. However, our field pulse is ramped, and especially the exact shape of the DW potential in the ratchet is a complicating factor, since a linear irradiation gradient does not necessarily lead to a linear potential landscape. For each of the individual ratchets, we find a different μ ranging between 1.5 and 2.8, so this parameter is strongly related to the local material structure.

Tunable domain-wall oscillator at an anisotropy boundary

4

We propose a magnetic DW oscillator scheme, in which a low DC current excites GHz angular precession of a DW at a fixed position. The scheme consists of a DW pinned at a magnetic anisotropy step in a perpendicularly magnetized nanostrip. The frequency is tuned by the current flowing through the strip. A perpendicular external field tunes the critical current density needed for precession, providing great experimental flexibility. We investigate this system using a simple 1D model and full micromagnetic calculations. This oscillating nanomagnet is relatively easy to fabricate and could find application in future nanoscale microwave sources. *

4.1 Introduction

As predicted theoretically[6], the magnetization of a free magnetic layer in a multilayer nanopillar can oscillate at GHz frequencies caused by the spin transfer torque exerted by a DC spin polarized current[90–92]. These magnetic oscillations at the nanoscale could find application in the area of radio-frequency (RF) devices, such as wide-band tunable RF oscillators. More fundamentally, magnetic precessions induced by a spin-polarized current can also be used to study nonlinear magnetization dynamics, either of individual or multiple coupled oscillators[93].

However, the fabrication of such nanopillar devices is particularly hard and the frequency and the output power can not be tuned independently. An alternative oscillating nanomagnet is a precessing magnetic DW. It is already widely known that DWs precess during motion at currents (and fields) above the so-called Walker limit[10]. Obviously, for a continuously operating oscillator it is vital that the DW remains at a fixed position, but for commonly used in-plane magnetized materials (i.e. $Ni_{80}Fe_{20}$) a high current density is needed for Walker precession, leading to DW displacement motion which is undesired for this particular application.

*Published as: *Tunable magnetic domain wall oscillator at an anisotropy boundary*. J. H. Franken, R. Lavrijsen, J. T. Kohlhepp, H. J. M. Swagten, and B. Koopmans, Applied Physics Letters **98**, 102512 (2011).

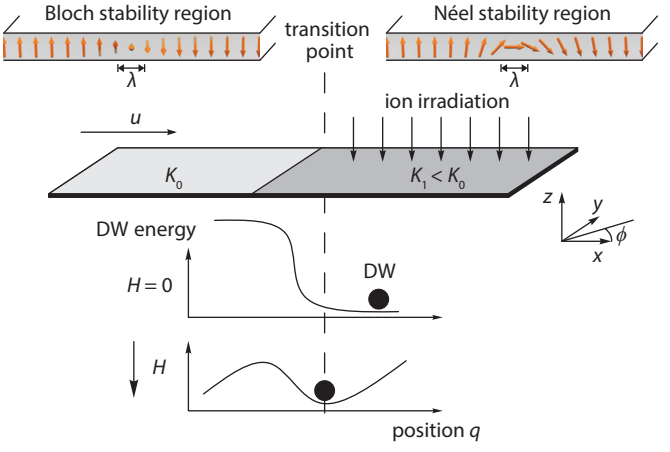

Figure 4.1 | Sketch of the perpendicularly magnetized strip with a step in the magnetic anisotropy (from K_0 to K_1) and associated DW potentials in the absence and presence of an external magnetic field. The DW potential tilts upon field application and therefore, the equilibrium position of the DW might shift from the Néel to the Bloch stability region. At a properly tuned field, the DW is at the transition point where both types are equally favorable, which makes it easy to excite DW precession $\dot{\phi}$ by a spin polarized current (u).

Experiments have been reported on RF-driven DW resonance [94–97], but for use as an RF source, a DW device needs to convert a DC current to an RF signal. Recently, several such devices have been proposed in theory [67–69], but significant obstacles must be overcome before an experimentally feasible device can be produced. Perhaps the most viable scheme to date was proposed by Bisig *et al.* [67], using a DW pinned at a constriction in a nanostrip with large perpendicular magnetic anisotropy (PMA). The key for achieving DW precession at low DC currents is to minimize the energy barrier for DW transformation between the Bloch and Néel types of which side views are shown in the top of Figure 4.1. In wide strips, Bloch walls have the lowest magnetostatic energy, whereas the Néel wall is preferred in very narrow strips [98]. By locally reducing the strip width at the constriction, the energy barrier between the Bloch and Néel walls is minimized, leading to a low critical current in this scheme. However, at the constriction the strip width needs to be trimmed to a challenging 15 nm, and also the DW somehow needs to be initialized at the correct position, leading to cumbersome experimental schemes.

In this Chapter, we propose a different scheme that overcomes these difficulties. It is inspired by our recent experimental observation that a DW in a nanostrip can be controllably pinned at a magnetic anisotropy step created by, for example, ion irradiation [22,24,49]. Interestingly, the anisotropy also controls the width of a DW, and therefore it controls whether the Bloch or Néel wall is stable. Intuitively, this is understood by considering the DW as an isolated magnetic volume which minimizes its magnetostatic energy by aligning with its longest axis, which is either along the strip for wider walls (Néel) or transverse to the strip for narrow walls (Bloch). One

can thus tune the anisotropy values at both side of the boundary in such a way, that a Bloch/Néel wall is stable in the two respective regions (Figure 4.1). A DW can be pinned exactly at the transition point between the Bloch/Néel stability regions by a DC external field, as sketched in the figure. At this position, the energy barrier between both walls is minimal and therefore, oscillations are easily excited by DC currents. We study the feasibility of this approach by a 1D model and micromagnetic simulations and discuss its advantages in terms of ease of fabrication, experimental flexibility and scalability.

4.2 1D model

To characterize the behavior of this DW oscillator as a function of current and field, we first investigate its dynamics by introducing a 1D model. Starting from the Landau-Lifshitz-Gilbert equation of magnetization dynamics with spin-torque terms and parameterizing the DW using the collective coordinates q (DW position), ϕ (in-plane DW angle) and λ (DW width) [67,98], we get†

$$\dot{\phi} + \alpha\dot{q}/\lambda(q) = \beta u/\lambda(q) + \frac{\gamma}{2M_s}\frac{\partial E}{\partial q}, \tag{4.1}$$

$$\dot{q}/\lambda(q) - \alpha\dot{\phi} = u/\lambda(q) + \frac{\gamma}{M_s}K_d(q)\sin 2\phi, \tag{4.2}$$

where $u = \frac{g\mu_B PJ}{2eM_s}$ is the spin drift velocity, representing the electric current, with g the Landé factor, μ_B the Bohr magneton, P the spin polarization of the current, J the current density and e the (positive) electron charge. M_s is the saturation magnetization, γ is the gyromagnetic ratio, α the Gilbert damping constant, β the nonadiabaticity constant and K_d the transverse anisotropy. The term $\partial E/\partial q$ is the derivative of the DW potential energy, which was obtained by assuming that the DW retains a Bloch profile symmetric around its center ($m_z = \tanh(x/\lambda)$). Using our geometry sketched in Figure 4.1, this yields $\mathrm{d}E/\mathrm{d}q = 2\mu_0 M_s H - (K_0 - K_1)\,\mathrm{sech}^2(q/\lambda(q))$, based on the model introduced in section 2.3.1. Here we have made the additional assumption that the effective perpendicular anisotropy (uniaxial anisotropy minus shape anisotropy, $K_{eff} = K_u - \frac{1}{2}\mu_0 N_z M_s^2$) changes instantly from the high value K_0 to the lower value K_1 at the position $q = 0$. This is appropriate if the anisotropy gradient length is smaller than the DW width, which can be achieved using a He focused ion beam [49] (see section 2.6.5). The transverse anisotropy constant K_d represents the energy difference between a Bloch ($\phi = \pm\pi/2$) and Néel ($\phi = 0$ or π) wall and results from demagnetization effects. Therefore, it depends on the dimensions of the magnetic volume of the DW, given by the DW width λ, the width of the magnetic strip w, and its thickness t. We estimate the demagnetization factors N_x, N_y and N_z of the DW by treating it as a box with dimensions $5.5\lambda \times w \times t$ [51]. The effective DW width 5.5λ was determined from micromagnetic

†This model is a dynamic description of our previously introduced DW energy model, based on the Landau-Lifshitz-Gilbert equation of magnetization dynamics. We will describe it in more detail in Chapter 7, where we introduce current-induced experiments.

simulations: if $w \approx 5.5\lambda$ the Bloch and Néel walls have the same energy and the transverse anisotropy $K_\mathrm{d} = \frac{1}{2}\mu_0(N_x - N_y)M_\mathrm{s}^2$ vanishes because $N_x \approx N_y$.

In the absence of transverse anisotropy ($K_\mathrm{d} = 0$), an analytical solution exists to the system of (4.1) and (4.2). The DW will precess at a constant frequency f proportional to the current, [67]

$$2\pi f = \dot{\phi} = \frac{-u}{\alpha\lambda}, \qquad (K_\mathrm{d} = 0), \tag{4.3}$$

while the DW remains at a fixed position ($\dot{q} = 0$). For the case $K_\mathrm{d} \neq 0$, however, the system is solved numerically using a standard Runge-Kutta time integration method. We use parameters typical for a Co/Pt multilayer system, with $M_\mathrm{s} = 1400\,\mathrm{kA/m}$, $A = 16\,\mathrm{pJ/m}$ and $\alpha = 0.2$. For the moment, we assume only adiabatic spin torque ($\beta = 0$). For the effective anisotropy at the left side of the boundary, we choose $K_0 = 1.3\,\mathrm{MJ/m^3}$ (corresponding to $K_{\mathrm{u},0} = 2.5\,\mathrm{MJ/m^3}$), typical for a sputtered Pt/Co multilayer [99]. By ion irradiation, this can be reduced to arbitrarily low values such as $K_1 = 0.0093\,\mathrm{MJ/m^3}$ ($K_{\mathrm{u},1} = 1.2\,\mathrm{MJ/m^3}$) at the right of the boundary. We choose this high anisotropy contrast to ensure the DW is very strongly pinned, but the physics presented here remain the same for other values. For the calculation of the transverse anisotropy, we use the geometry $w = 60\,\mathrm{nm}$ and $t = 1\,\mathrm{nm}$. The very low K_1 leads to a DW that is wide ($\lambda_1 = \sqrt{A/K_1} \approx 41\,\mathrm{nm}$) relative to the strip width, which ensures stability of the Néel wall in the right region, whereas a Bloch wall is stable in the left region ($\lambda_0 \approx 3.5\,\mathrm{nm}$). At the boundary, the anisotropy is not constant within the DW volume leading to a nontrivial dependence of λ on position q. Under the given assumptions, the derivative of internal DW energy equals $\mathrm{d}E_\mathrm{DW}/\mathrm{d}q = (K_0 - K_1)\,\mathrm{sech}^2(q/\lambda(q))$. By using the fact that $E_\mathrm{DW} = 4A/\lambda$, numerical integration yields $\lambda(q)$ as presented in the inset of Figure 4.2(a). The fact that the DW width depends on the position implicitly leads to a time-dependent DW width λ, which we take into account by updating $\lambda(q)$ at every integration step. Time variations in K_d are taken into account as well, because it depends on λ.

Solutions of the precession frequency at various fields and currents are plotted in Figure 4.2(a). The results differ from the purely linear behavior predicted by (4.3) in two ways. First of all, because of the energy barrier K_d between the Bloch and Néel walls, a critical current density needs to be overcome before precession occurs. Of the curves shown, a field of 70 mT yields the lowest critical current, so apparently this field brings the DW close to the Bloch/Néel transition point. The second deviation from linearity is seen at high current densities, where an asymmetry between negative and positive current densities exists. This arises solely from the change of the DW width: with increasing positive (negative) current density, the equilibrium DW position is pushed to the left (right), where the DW becomes narrower (wider). This behavior is sketched in the insets of Figure 4.2(a). By dividing u by λ, the linear behavior of (4.3) is recovered at high current densities (not shown). We also observe that the DW position q oscillates with an amplitude of about 1 nm and with twice the angular precession frequency (not shown), because the Bloch and Néel wall energy are minimized at different positions (both occur twice during a full precession period).

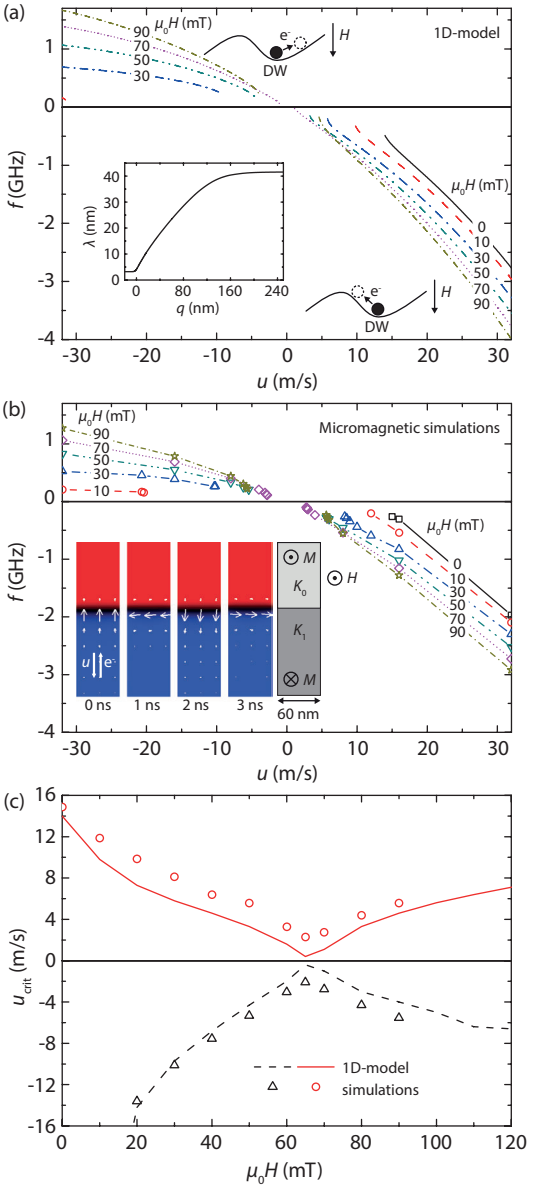

Figure 4.2 | (a) 1D-model solution of DW precession frequency as function of current density at various fields. Positive (negative) f indicates clockwise (counterclockwise) precession. Sketches show the potential landscape of the DW and the displacement due to the electron flow. The inset graph shows the equilibrium DW width as function of position. (b) Similar to (a), but obtained from micromagnetic simulations. The inset shows snapshots of the spin structure during simulation ($\mu_0 H = 70\,\mathrm{mT}$, $u = 4\,\mathrm{m/s}$). (c) Critical spin drift velocity (current) as a function of applied field, obtained using the two methods.

4.3 Micromagnetic simulations

To confirm the validity of our 1D approximation, we simulate the same system using micromagnetic calculations [56]. The strip is 400 nm long, 60 nm wide and 1 nm thick and divided into cells of 4x4x1 nm^3. The uniaxial perpendicular anisotropy constants to the left and right of the center are $K_{u,0} = 2.5$ and $K_{u,1} = 1.2\,MJ/m^3$, respectively, yielding the same effective anisotropy constants K_0 and K_1 as before when shape anisotropy is subtracted. A DW is initialized at the boundary and energetically relaxed. Simulations with various values of the applied field and current are performed, and the terminal precession frequency is extracted. Snapshots of the spin structure during precession are shown in the insets of Figure 4.2(b). The results in Figure 4.2(b) qualitatively match our simplified 1D model, with slightly lower frequencies. However, the critical current needed for precession is somewhat larger in the simulations as compared to the 1D model, which is shown in Figure 4.2(c) where the field dependence of the critical current is plotted for both methods. We attribute this to an observable deviation from the 1D profile in the simulations, which leads to inhomogeneous demagnetization fields posing additional energy barriers between the Bloch and Néel states. At $\mu_0 H \approx 65\,mT$, $u_{crit} \approx 2\,m/s$ is minimized, which corresponds to a current density $J \approx 9 \times 10^{10}\,Am^{-2}$ assuming a spin polarization $P = 0.56$ in Co/Pt [100]. Nanostrips can withstand current densities in this range, and the critical current can be further reduced by proper tuning of the material properties, for example by reducing the anisotropy step, which gives better agreement with the 1D profile.

Although the nonadiabatic β-term in (4.1) greatly affects the dynamics of *moving* DWs [10], we found only minor consequences for a *pinned* oscillating DW. Simulations at varying β could be reduced to a single $f(u,H)$ curve by a simple correction to the external field $H^\star = H + \frac{\beta u}{\mu_0 \gamma \lambda}$, which vanishes in the low-current regime and slightly pushes the DW to the left or right in the high-current regime, depending on current polarity. We therefore conclude that the uncertainty in the reported magnitude of β has no consequences for the correct operation of this device.

4.4 Discussion & conclusion

We argue that this DW oscillator scheme has several advantages over prior schemes. First of all, one does not need complicated nanostructuring of geometric pinning sites, as FIB irradiation readily creates pinning sites without changing the geometry and with a spatial resolution in the nm range when a focused He beam is used [49]. Secondly, initialization of a DW at an anisotropy boundary is inherently simple; the area with reduced anisotropy has lower coercivity and is therefore easily switched by an external field. Thirdly, many DW oscillators can be introduced in a single strip by an alternating pattern of irradiated and non-irradiated regions, and all DWs can be initialized at the same time by the external magnetic field. Fourthly, the external magnetic field provides the unique experimental flexibility to tune the critical current needed for precession after the device has been fabricated. The field might be cumbersome in device applications, but by correctly tuning the anisotropy K_1 a low critical current density at zero field is also possible. The main advantage of DW oscillators over the conventional nanopillar geometry is the ability to tune the

frequency independent of the microwave output power. This can be achieved by letting the DW act as the free layer of a magnetic tunnel junction (MTJ) grown on top of the DW and with the approximate dimensions of the DW ($20 \times 60\,\mathrm{nm}^2$), in a three-terminal geometry[69]. Interestingly, the output power of such a device might exceed that of a conventional STO, since the DW exhibits full angular precession in contrast to the small-angle precession of most STOs, at a similar feature size. An estimate of the output power can be made using the parameters of an STO MTJ[101], namely a low resistance-area product ($1.5\,\Omega\mu\mathrm{m}^2$), a TMR ratio of 100% and a maximum bias voltage of 0.2 V. Under these assumptions, we estimate a maximum RF output power $P_{\mathrm{rms}} = 23\,\mu\mathrm{W}$. Although this figure would already be useful for applications, the output power can be further increased by producing arrays of DW oscillators which are coupled through dipolar fields, spin waves and/or the generated RF current. Simulations have been performed illustrating that slightly different DW oscillators in closely spaced parallel strips indeed oscillate at a common frequency due to stray field interaction. ‡

Alternative ways to probe the oscillations are the Anisotropic Magnetoresistance (AMR) effect (due to the varying angle between DW and current direction), the intrinsic DW resistance (which depends on the time-varying DW width), or the Anomalous Hall Effect (AHE) in transverse contacts (through periodic DW displacements of the order of a few nm).

In conclusion, we have introduced a DW oscillator scheme, in which a low DC current excites GHz precession of a DW pinned at a boundary of changing anisotropy in a PMA nanostrip. The frequency of the precession is tuned by the DC current amplitude. A perpendicular external field tunes the critical current needed for precession. The system is well-described by a 1D model, which gives results almost identical to micromagnetic calculations.

‡See http://goo.gl/UXiUez for a micromagnetic simulation movie of two different oscillators oscillating at one common frequency due to stray field coupling. In the top strip, the uniaxial anisotropy changes from $K_{\mathrm{u},0} = 2.4\,\mathrm{MJ/m}^3$ (left) to $K_{\mathrm{u},1} = 1.2\,\mathrm{MJ/m}^3$. In the bottom strip, $K_{\mathrm{u},0} = 2.5\,\mathrm{MJ/m}^3$ yielding a different frequency. Due to the small separation (32 nm), both systems oscillate at a locked frequency of 1.46 GHz, with $u = 9\,\mathrm{m/s}$ and $\mu_0 H = 70\,\mathrm{mT}$. Frequency locking disappeared when the distance was doubled to 64 nm. The two oscillators have a different phase, minimizing the magnetostatic energy of the system.

Voltage-gated domain-wall pinning 5

In spintronic devices relying on magnetic DW motion, robust control over the DW position is required. We use electric-field control of perpendicular magnetic anisotropy to create a voltage-gated pinning site in a microstructured Pt/Co/AlOx DW conduit. A DW pins at the edge of a gate electrode, and the strength of pinning can be tuned linearly and reversibly with an efficiency of 0.22(1) mT/V. This result is supported by a micromagnetic model, taking full account of the anisotropy step at the gate edge, which is directly caused by a change in the electron density due to the choice of material. *

5.1 Introduction

In recent years, control of ferromagnetic (FM) devices by electric fields has received a lot of attention due to very promising prospects for low-power memory and logic devices. In particular, it was found that applying a voltage to a thin magnetic film across a gate dielectric can reversibly alter the magnetic properties, such as the magnetic anisotropy[102–109], coercivity[110,111], saturation magnetization[102,112,113], and Curie temperature[112,114]. This has been demonstrated to be of use in exciting applications such as low-dissipative voltage-driven switching[115,116], voltage-gated switching by the spin Hall effect[117], controlling the domain structure[118–120] and control over magnetic DW velocities[86,121–124]. Several mechanisms can be responsible for these effects: strain transfer from a ferroelectric layer[118–120], changes to the occupation of electron orbitals at the FM / oxide interface[102], charge trapping[125] and finally, migration of O ions from the interface[126].

Recently Bauer *et al.*[126] have been able to create pinning sites in a DW conduit† which can be reprogrammed by applying a voltage. This is particularly promising for application in current-driven DW racetrack memory[7], in which a long train

*Published as: *Voltage-gated pinning in a magnetic domain-wall conduit*. J. H. Franken, Y. Yin, A. J. Schellekens, A. van den Brink, H. J. M. Swagten, and B. Koopmans, Applied Physics Letters **103**, 102411 (2013).

†By a DW conduit, we simply mean a magnetic nanostrip through which a DW is able to propagate.

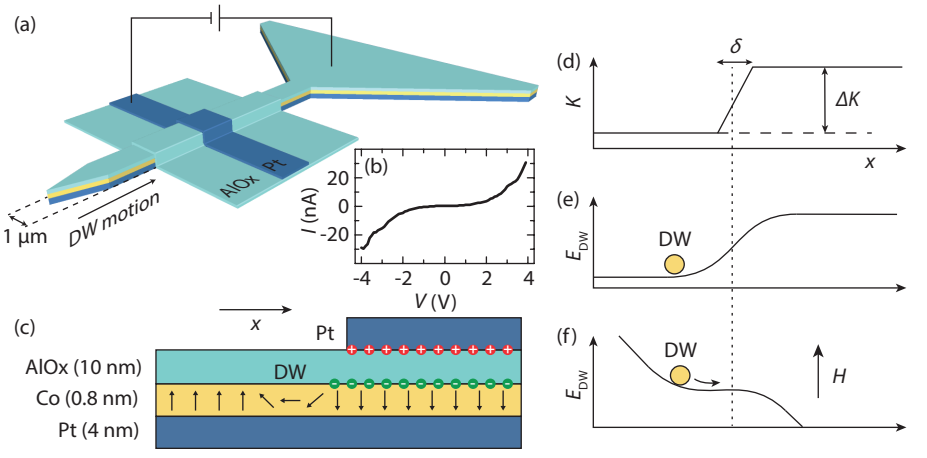

Figure 5.1 | (a) Sketch of the fabricated device. (b) I-V characteristic of the device. (c) Sketch of the situation in the gate region: the excess electrons at the AlOx/Co interface enhance the magnetic anisotropy, thereby creating a step in the anisotropy at the gate boundary as sketched in (d). This leads to a DW being pinned in the DW energy landscape sketched in (e). Upon application of a magnetic field H in (f), the DW can be depinned.

of magnetic DWs propagates through a nanostrip which functions as a DW conduit. Reproducible operation of such a device requires well-defined pinning sites, which are typically realized by locally altering the geometry [40] or material properties [49,82,127]. The ability to activate and deactivate these pinning sites, preferably at fast timescales, provides new device options and could greatly reduce the current density needed to move the DWs from site to site. The devices by Bauer *et al.* [126] relied on the effect of electromigration, which has its own advantages and disadvantages. Bernand-Mantel *et al.* [124] also showed DW pinning at the boundary of a large electrode by the completely different effect of interface charging, although a systematic analysis of the tunability of the effect was still lacking.

In this Chapter, we have equipped a microstructured DW conduit with a voltage-gated pinning site which functions by changing the electron density at the FM / oxide interface. The effect is demonstrated in Pt/Co/AlOx, a material that is also very interesting for device applications since it exhibits very fast current-induced DW motion [30]. We show that the pinning strength experienced by a DW at the edge of a gate electrode is enhanced or decreased reversibly and linearly by a positive or negative voltage. The linear relation between pinning strength and voltage is supported by a micromagnetic model, taking into account the details of the electric field distribution that creates the step in the anisotropy leading to pinning.

5.2 Experimental design

Devices were fabricated following the design of Figure 5.1(a). The devices consist of a bottom Pt (4 nm) / Co (0.8 nm) and a top Pt (20 nm) electrode, separated by

a 10 nm AlOx insulating layer. The bottom Pt/Co/AlOx electrode shows perpendicular magnetic anisotropy (PMA) [128] and is fabricated by means of Electron Beam Lithography (EBL) followed by sputtering of Pt/Co/Al, plasma oxidation of the Al layer, and lift-off. It is shaped to function as a conduit for magnetic DWs by patterning it into a 1 μm wide strip with a large contact pad attached to it on one end, while the other end is tapered. After fabrication of the bottom electrode, an additional AlOx layer is deposited everywhere to ensure gate insulation, and the sample is annealed at 300°C. After that, the top Pt electrode is fabricated by EBL.

The I-V characteristic of the fabricated device is shown in Figure 5.1(b). It is seen that the AlOx layer functions as a tunnel barrier, with a tunneling current that is negligibly small between -4 V and +4 V, allowing us to exclude current-induced effects on the magnetization. In our main experiment, we therefore apply voltages in this range and study how DW pinning at the electrode position is affected. The idea of the experiment is as follows (see Figure 5.1(c)): by applying a voltage of the appropriate sign, the anisotropy in the DW conduit is increased in the gate region. A perpendicular magnetic field H is applied to move a DW from left to right through the conduit. The DW experiences a step ΔK in the anisotropy before entering the gate region (Figure 5.1(d)). Since the energy cost of a DW increases with $\sqrt{K}$, this creates a step in the DW energy landscape at the edge of the gate, where the DW tends to be pinned (Figure 5.1(e)). The pinning can be overcome by applying a stronger H-field, which tilts the energy landscape due to the added Zeeman contribution (Figure 5.1(f)).

5.3 Experimental results

The motion of DWs through the fabricated DW conduit is observed directly using Kerr microscopy (Figure 5.2(a)). First, we describe the situation without an applied voltage (middle row of images). Starting from negative saturation, the external magnetic field is increased to 4 mT and a DW is nucleated. Interestingly, the DW does not nucleate in the contact pad as intended, but rather at the tapered end, an effect that was recently described in detail [129]. After nucleation, the DW propagates towards the gate. It is observed that the DW stops to the left of the gate (left image), even when the voltage is zero. Since this is observed in almost all fabricated devices, we believe the material properties are slightly different underneath the contact due to, e.g., strain effects or fabrication details, which create a pinning position for the DWs. However, the pinning strength is quite weak and of the same order as natural pinning sites which occur randomly in Pt/Co/AlOx DW conduits. The DWs can therefore still be moved past the gate by applying a slightly higher z-field of 5.0 mT (see the change between the left and center image at 0 V); this field is referred to as the *pinning field*.

We now repeat the experiment for various applied voltages and study how the pinning strength is altered. Kerr microscopy snapshots for -4 V, 0 V and 4 V are shown in Figure 5.2(a). Indeed, it is observed that the applied voltage leads to either enhancement or reduction of the pinning field, depending on the sign of the applied voltage. A negative voltage increases the pinning strength, as seen in the top row of images. On the other hand, a positive voltage leads to a significantly reduced pinning field (< 4.0 mT), as seen in the bottom row of images.

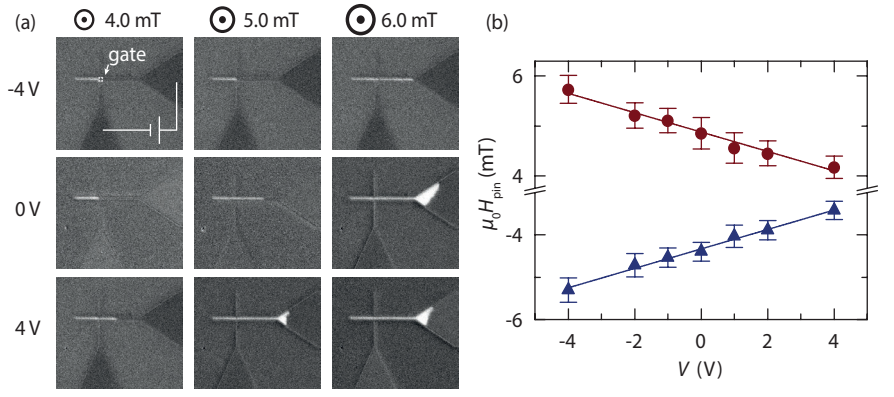

Figure 5.2 | (a) Kerr microscopy images of DW behavior around the gate as a function of applied magnetic field (horizontal) and applied voltage (vertical). It is seen that the DW moves past the gate at a field strength which depends on the voltage. (b) Systematic measurement of the pinning field as a function of voltage. Similar slopes are found for up-down DWs (red discs, $0.23 \pm 0.01\,\mathrm{mT/V}$) and down-up DWs (blue triangles, $0.19 \pm 0.01\,\mathrm{mT/V}$). The error bar represents the standard deviation of the measurement (10 repeats).

In Figure 5.2(b), we have performed a systematic measurement of the pinning field as a function of voltage. At each voltage, the experiment outlined above is repeated $N = 10$ times and the average pinning field is plotted, where the error bar represents the standard deviation of the measurement (which is $\sqrt{N-1}$ times larger than the error in the average). It is found that the pinning strength changes linearly with the applied voltage. Comparing the red and blue lines in Figure 5.2(b), it is observed that the pinning strength is altered similarly for the two H-field polarities, which is compatible with the idea that we are tuning the DW pinning barrier and further excludes effects of the leakage current. The effect of the voltage on DW pinning (average absolute slope of Figure 5.2(b)) quantifies to $0.22 \pm 0.01\,\mathrm{mT/V}$ in the studied range. Somewhere beyond 4 V, the device suffered from dielectric breakdown after which the junction was destroyed. Looking at the error bars, it can be seen that there is a certain spread among individual measurements of the pinning field at constant voltage. This can be attributed to thermally activated depinning: even if a field below the 'true' (zero-temperature) pinning field is applied, there is a certain probability for the DW to overcome the energy barrier [40], leading to a statistical distribution in the measured pinning field.

5.4 Discussion

We now turn to our simple DW-energy model developed in section 2.3 in order to verify these results, in particular the magnitude of the observed pinning effect. In our previous experiments on permanent DW pinning sites created by focused ion beam irradiation [49,82] (Chapter 2), we developed equation (2.14) to describe the

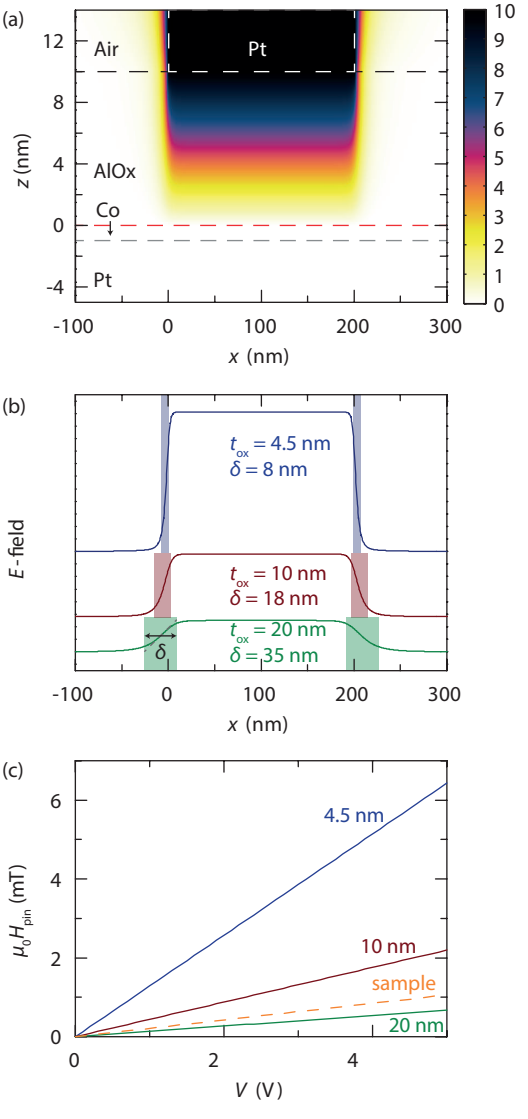

Figure 5.3 | (a) Calculation of the voltage profile at the gate for an AlOx thickness $t_{ox} = 10\,\text{nm}$. The resulting E-field as a function of x at the Co/AlOx interface (red dashed line) is plotted in (b) for $t_{ox} = 4.5\,\text{nm}$ (blue), $t_{ox} = 10\,\text{nm}$ (red) and $t_{ox} = 20\,\text{nm}$ (green), where the shaded area indicates the width of the E-field profile, which is seen to increase for thicker t_{ox}. Panel (c) shows the expected DW pinning strength as a function of voltage based on the profile width δ plugged into (5.1), along with a fit to the experimental data (dashed orange line).

pinning field at an anisotropy step ΔK,

$$H_{\mathrm{pin}} = \frac{\Delta K}{2\mu_0 M_s} \times \frac{2\lambda}{\delta} \tanh \frac{\delta}{2\lambda}. \tag{5.1}$$

Here, M_s is the saturation magnetization (1400 kA/m for Co), and λ the width of the DW. We estimate $\lambda = \sqrt{A/K} = 7.7\,\mathrm{nm}$, assuming the exchange stiffness $A = 16\,\mathrm{pJ/m}$ [89] and the effective uniaxial anisotropy $K = 0.27\,\mathrm{MJ/m^3}$, measured by SQUID magnetometry. Furthermore, two important tunable parameters can be identified: (1) the magnitude of the step in the anisotropy ΔK, and (2) the length scale δ of the anisotropy gradient, as defined in Figure 5.1(d).

To estimate the magnitude of ΔK in our experiments, we use results that were obtained on very large junctions made of the same material, where the DW velocity was altered using an electric field [86]. In this experiment, it was found that in order to explain the observed changes in DW velocity, the change of the Co/AlOx surface magnetic anisotropy per applied electric field amounted to $14 \pm 2\,\mathrm{fJV^{-1}m^{-1}}$. Multiplying this value by the electric field V/t_{ox} and dividing by the Co thickness (0.8 nm) yields the effective (volume) anisotropy change ΔK. Less straightforward is the estimation of the length scale of the anisotropy gradient, δ. The electron density at the Co/AlOx interface, which determines K, is not expected to jump instantaneously at $x = 0$, where the top electrode starts. Rather, the electron density is expected to change gradually, and the characteristic length δ of this change might depend on the thickness t_{ox} of the insulating layer and its relative permittivity ϵ_r. To estimate this, a 2D COMSOL model is developed which calculates the electric field distribution in the layer system around the gate region. Taking $\epsilon_r = 7$ for AlOx and $t_{\mathrm{ox}} = 10\,\mathrm{nm}$, we find the voltage distribution as sketched in Figure 5.3(a). It is expected that the the PMA scales with the electric field at the Co/AlOx interface (dashed line), which is plotted as a function of x in Figure 5.3(b) for various t_{ox}. As expected, it is observed that δ increases with t_{ox}, which is visualized by the shaded areas in Figure 5.3(b). We define the gradient length δ by extrapolating the slope at the center of the profile to the full profile height. If we incorporate the values of δ extracted from Figure 5.3(b) into the model of (5.1), we get the pinning strength as a function of voltage shown in Figure 5.3(c) for varying AlOx thickness t_{ox}. The slope of the voltage induced pinning field for a 10 nm thick AlOx layer is 0.44 mT/V (red line in Figure 5.3(c)), of the same order as the value 0.22 ± 0.01 mT/V found in the experiment (dashed orange line in Figure 5.3(c)). We therefore think this model captures the essential physics of the observed effect, although fully quantitative agreement cannot be claimed due to various subtleties, such as the uncertainty in the voltage dependence of K, the 1D-model simplification, the roughness of the top electrode, the precise value of the DW width λ, and the fact that DW pinning is a thermally assisted process. We should also note that in the model, pinning is absent at 0 V, whereas in the experiment the strength of an already existing pinning barrier is altered, although this does not have major consequences for the physics involved.

5.5 Conclusion

In conclusion, we have demonstrated a pinning site in a Pt/Co/AlOx DW conduit which can be tuned by applying an electric field. The pinning field was shown to change linearly as a function of applied voltage at $0.22 \pm 0.01\,\mathrm{mT/V}$. A simple micromagnetic 1D model in combination with calculations of the electric field distribution yielded a reasonable reproduction of the observed effect. The model suggests that not only the magnitude of the electric field, but also the width of the electric field distribution at the gate edge is important in engineering an efficient pinning site. Although a much stronger pinning field was achieved by Bauer *et al.* [126] using the effect of electromigration, our result is caused by the completely different mechanism of tuning the electron density at the interface which might have its own advantages, such as a potentially higher toggling speed. In a preliminary experiment, we have observed that a pinned DW depins relatively quickly ($\sim 1\,\mathrm{s}$) after the voltage is removed. It is therefore worthwhile to investigate the speed limit of this mechanism for application in future devices.

Beam-induced Fe nanopillars as tunable domain-wall pinning sites

6

We employ Focused-Electron-Beam-Induced Deposition (FEBID) to create freestanding magnetic nanostructures. By growing Fe nanopillars on top of a perpendicular magnetic DW conduit, pinning of the DWs is observed due to the stray fields emanating from the nanopillar. Furthermore, we observe a different DW pinning behavior between the up and down magnetic states of the pillar, allowing us to deduce the switching fields of the pillar in a novel way. The implications of these results are twofold: not only can 3-dimensional nano-objects be used to control DW motion in applications, we also propose that DW motion is a unique tool to probe the magnetic properties of nano-objects. *

6.1 Introduction

Magnetic DWs receive widespread attention due to their promising application in novel nanodevices [7,70,127]. In an envisioned 3-dimensional memory device, DWs are propagated between discrete sites along a nanostrip, forming a bit shift register with a very high data density [7]. However, an efficient way to pin DWs at discrete positions is needed [130], and novel nanostructuring techniques are required to create 3-dimensional structures. An interesting new route to 3-dimensional nanostructures is provided by Focused-Electron-Beam-Induced Deposition (FEBID) [131–142], a tool that can be used to create nano-objects of any desired shape. Here, we employ this technique to create vertical iron nanopillars and demonstrate their magnetic behavior through the effect they have on DW motion in an underlying DW conduit. We show that the stray fields from a magnetic nanopillar serve as an efficient pinning site for a magnetic DW in materials with perpendicular magnetic anisotropy (PMA), and that the pinning can be tuned by the height of the pillar as well as its magnetic state. This proves that these small freestanding structures are indeed magnetic, which we also show unambiguously by imaging the stray fields of the pillars in a Lorentz Transmission Electron Microscope (TEM). Furthermore, we exploit the

*Accepted for publication in Advanced Functional Materials as: *Beam-induced Fe nanopillars as tunable domain-wall pinning sites*. J. H. Franken, M. A. J. van der Heijden, T. Ellis, R. Lavrijsen, C. Daniels, D. McGrouther, H. J. M. Swagten, and B. Koopmans.

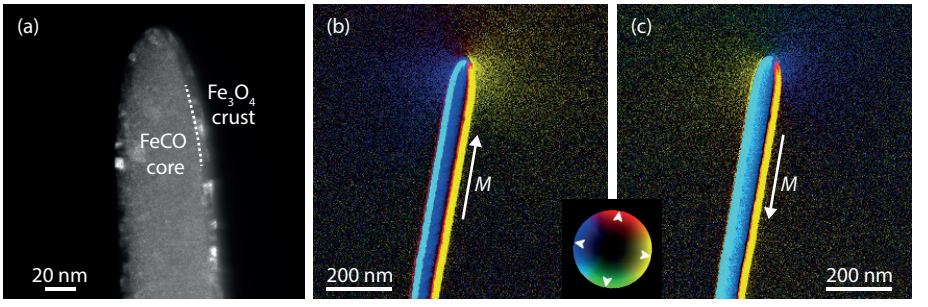

Figure 6.1 | (a) Dark field TEM image showing the pillar geometry and structure. (b-c) color DPC mode STEM images showing stray fields emanating from the pillar tip. From (b) to (c), the stray field directions in the space around the tip are inverted (see color code) when the magnetization of the pillar is switched by means of an external field (53 mT).

fact that DW pinning depends on the magnetic state of the pillar, to determine the switching field of the pillars themselves. This way of probing magnetic nano-objects is potentially interesting for nanomagnetic sensors based on DWs [143–146].

6.2 Imaging stray fields of magnetic pillars

To perform the experiments, pillars with diameters between 45 and 70 nm were grown using a $Fe_2(CO)_9$ precursor [147,148] and a focused electron beam to dissociate the precursor molecules, thereby depositing the desired structures (see Methods section 6.6). This yielded pillars with at most 60% Fe, with O and C as the other main constituents [147]. By changing the dwell time and precursor pressure, the height of the pillars is varied between 100 nm and 1 μm. First, we confirm the properties and magnetic behavior of the pillars by direct imaging using a (Scanning) Transmission Electron Microscope ((S)TEM) equipped with a cold field emission gun. Figure 6.1(a) shows a high magnification dark field image of one of the pillars. It can be seen that the width of the pillar is $\sim$ 53 nm and it consists of an amorphous/ultra nano-crystalline core surrounded by a poly-crystalline coating, 6 nm in thickness, which has been previously shown [147] to be Fe_3O_4. The radius of curvature at the tip of the pillar is $\sim$ 20 nm.

Figure 6.1(b-c) show color Differential Phase Contrast (DPC) images [149,150] of a 1.2 μm high pillar, acquired from operation of the microscope in Lorentz STEM mode (see section 6.6). In both figures, in the free-space adjacent to the top of the pillars, color contrast is observed that relates to the stray fields emanating from the pillar. The color contrast in the pillar itself is unfortunately non-interpretable, because it is dominated by strong electrostatic contributions arising due to the circular cross-section and oxide layer that obscure the magnetic component. In Figure 6.1(b), moving clockwise around the pillar tip, the color contrast changes from blue to red to yellow. By referring to the color wheel, the magnetostatic fields can be understood to be diverging from the tip. That no strong magnetostatic contrast is observed anywhere else but at the base of the pillar suggests strongly that it is

uniformly magnetized in an upwards direction (any DWs within such narrow pillars would be expected to have associated stray field distributions). After application of a magnetic field of 53 mT oriented downwards, the magnetostatic color contrast at the tip in Figure 6.1(c) is observed to have altered. Moving round the tip in a clockwise direction, the colors go from yellow to green to blue, from which it is inferred that the magnetization in the pillar has been reversed by the field.

6.3 Stray-field induced pinning

We now study the effect that the stray fields emanating from the base of the pillar have on DW motion in underlying DW conduits. It has previously been shown that dipolar stray fields generated by an array of nanodots produced by a conventional lithography method alters the average speed of DW motion in a 2-dimensional film [151], but here our aim is to completely stop a DW in a 1D DW conduit by a single nanopillar of varying height. An analogous approach was studied in detail in systems where the magnetization was oriented along the length of the DW conduit, by the use of dipolar fields generated by coplanar magnetic nanobars [80,152,153] or by a small coil wound around a microwire [154]. The reciprocal effect was also studied, where the stray field of a moving DW was used to assist switching of a nearby magnetic element [155]. However, inducing DW pinning by stray fields that are oriented in-plane seems less appropriate in materials with perpendicular magnetization which are studied here. Although it could work to some extent because the magnetization inside the DW is also oriented in-plane, the pinning effect is expected to be small given the very small DW width that these materials typically exhibit, yielding a low interaction energy. Instead, an approach using perpendicularly oriented stray fields seems more appropriate, and such a field could be provided by our vertical nanopillars grown on top of a DW conduit.

The DW conduits consist of 500 nm wide Pt/Co/Pt strips, fabricated by electron beam lithography, sputtering and lift-off. This material exhibits PMA, so the magnetization is perpendicular to the sample plane in the two domains (up and down) which are separated by a DW as indicated in Figure 6.2(a). In order to introduce a DW into the conduit at a low and controlled magnetic field, Ga irradiation with a focused ion beam is employed on an area to the left of the pillar as indicated in Figure 6.2(b) (bright yellow area) to locally reduce the DW creation field [24]. The FIB was put slightly out of focus to get a smoother irradiation boundary, thereby reducing DW pinning at the boundary [49,82] (section 2.6.4) and making it easier to inject a DW into the non-irradiated part of the DW conduit, where our pillar is located. The field required to inject a DW into the conduit such that it can freely move towards the pillar is defined as the injection field H_{in} and has a typical value of 3 mT. For an untreated strip, the injection field would be much higher at typically 23 mT, and the domain wall would originate from an uncontrolled position.

Switching of the strips was studied using Kerr microscopy, and snapshots of the magnetic state of the DW conduit with increasing magnetic field are shown in Figure 6.2(b). The first image shows the saturated single-domain state at zero field, after coming from a high negative perpendicular field (-100 mT). As we will show later, both the pillar and the DW conduit are magnetized downwards in this starting

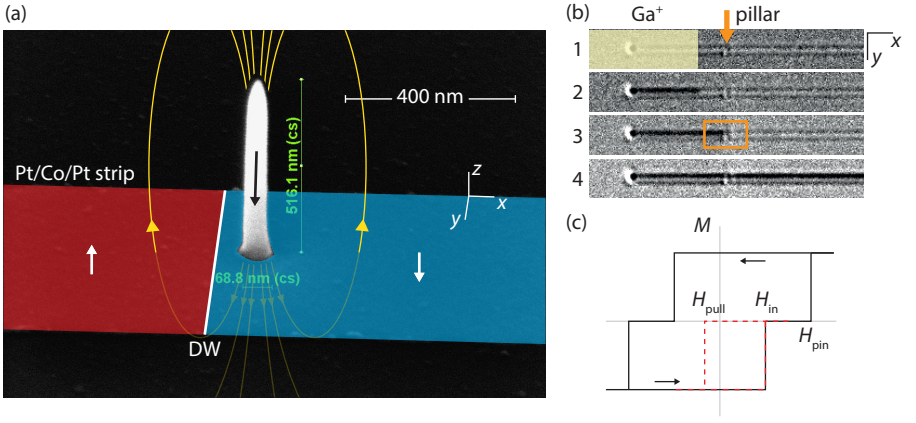

Figure 6.2 | (a) SEM micrograph of a Fe nanopillar deposited on top of a Pt/Co/Pt strip. A DW, present at the transition between up (red) and down (blue) magnetization, pins in front of the pillar because the domains are aligned with the pillar stray field (yellow field lines) in that case. (b) Kerr microscopy snapshots of the DW pinning experiment on a Pt/Co/Pt strip. The left (yellow) area of the strip is irradiated with Ga irradiation to nucleate a DW at low field. After negative saturation (1), the field is increased until the irradiated area is switched at $\sim 2\,\mathrm{mT}$ (2), the DW depins from the irradiation boundary at $H_{\mathrm{in}} \approx 3\,\mathrm{mT}$ and subsequently pins at the pillar (3), and finally the DW depins from the pillar at H_{pin} (4). A schematic hysteresis loop averaged over the (orange) region of interest is sketched in figure (c). A minor loop (red dashed line), is used to identify the negative field needed to move the DW back from the pillar position (H_{pull}).

position. While increasing the field, the second image shows nucleation of a DW in the irradiated area of the conduit (black and white contrast), which pins at the irradiation boundary. Further increasing the field in the third image, this DW is injected into the DW conduit but, remarkably, stops at the position where our pillar is located. This shows that FEBID-grown Fe pillars can indeed be used to pin a DW and since the effect is absent with non-magnetic Pt pillars (not shown), the pinning potential has to originate from the stray fields induced by the magnetic pillar. The last image shows that the DW can be depinned from the pillar if a sufficiently high field is applied. By averaging the optical contrast of the area around the pillar as a function of field (see Figure 6.2(b)(3), orange rectangle), a hysteresis loop can be obtained as sketched in Figure 6.2(c) (black line), where the plateau between H_{in} and H_{pin} indicates DW pinning. The field strength at which the DW leaves the pillar position is defined as the pinning field H_{pin}.

While we have shown that the pillar can block the motion of the DW in the forward direction, one could wonder if the same applies to the backward direction. Therefore, we also try pulling a DW that is pinned at the pillar position back to the direction where it came from, by sweeping back the field when the plateau is reached (minor loop in Figure 6.2(c)). It was found that this 'pulling field' $|H_{\mathrm{pull}}|$ required to move the DW to the left side was consistently lower than the pinning

field $|H_{\text{pin}}|$ required to move it to the right, and also lower than the injection field $|H_{\text{in}}|$ required to inject a new (opposite) DW from the left side. This is compatible with a picture of DW pinning by the magnetic stray fields emanating from a pillar with fixed magnetization as shown in Figure 6.2(a). This creates a favorable position for the DW right in front of the pillar where there is a transition of the z-component of the stray field from up to down, to align with the magnetization in the two domains. A significantly higher field is required to overcome the strong z-field right underneath the pillar and move the DW forward, as compared to the field needed to pull the DW back to overcome the weak opposite stray field in front of the pillar [151].

To find further proof for the pinning mechanism based on stray fields, we explore the tunability of the pinning effect by varying the pillar height as shown in Figure 6.3(a). The pillar height determines the stray-field-induced DW potential landscape underneath the pillars; a higher pillar gives a higher stray field right underneath the pillar, whereas field lines become more dispersed away from the pillar yielding a smaller opposite stray field in the circumference (see Appendix A.1). This is clearly observed in the magnitude of both the pinning and pulling field; the pinning field (a measure for the stray fields underneath the pillar) clearly increases with pillar height, whereas the pulling field appears to decrease slightly.

We now turn to a simple model to explain the DW pinning, based on the stray field that a pillar induces in the plane of the DW conduit (2 nm below the pillar). The stray field calculation was done as a function of pillar height using the Biot-Savart law, assuming a homogeneously magnetized cylinder with a diameter of 60 nm (see Appendix A.1 for details). This was used as input for a 1D DW model, where it was assumed that a DW at position x along the strip senses the z-component of the stray field, averaged along the width of the strip (500 nm). The calculated pinning and pulling fields reproduce the observed experimental behavior (Figure 6.3(b)). The pinning field increases for higher pillars (solid black line), whereas the pulling field is much lower and decreases (solid red line). In fact, we can use the measured DW pinning strength as a magnetometer for the pillar's magnetization, by choosing a value of M_s that gives agreement between model and experiment. A good match is found for $M_s \approx 100$ kA/m, and this value was used in the calculation of Figure 6.3(b). This deduced value of M_s is much lower than for pure Fe (1700 kA/m), which can be due to various reasons. First of all, the Fe content is much lower than 100%. In planar non-freestanding depositions grown in the same vacuum, a Fe content of 60% percent was found using Energy-dispersive X-ray spectroscopy (EDX) [147], but this does not necessarily translate to the pillar geometry, since the pillar has a relatively large surface area which is sensitive to oxidation, and the temperature during growth is expectedly different. We therefore might expect less than 60% Fe in the pillars. Secondly, the value of M_s is likely underestimated due to the effect of thermal activation: at room temperature, random fluctuations can lead to an escape of the DW over a finite energy barrier, which reduces the pinning field as compared to our zero-temperature model [80]. Thirdly, M_s may be underestimated if the remanence is less than 100%. Thirdly, other complicating factors are the precise shape of the bottom of the pillar, or the possibility of a compositional gradient along the length of the pillar. In Fe pillars grown by different

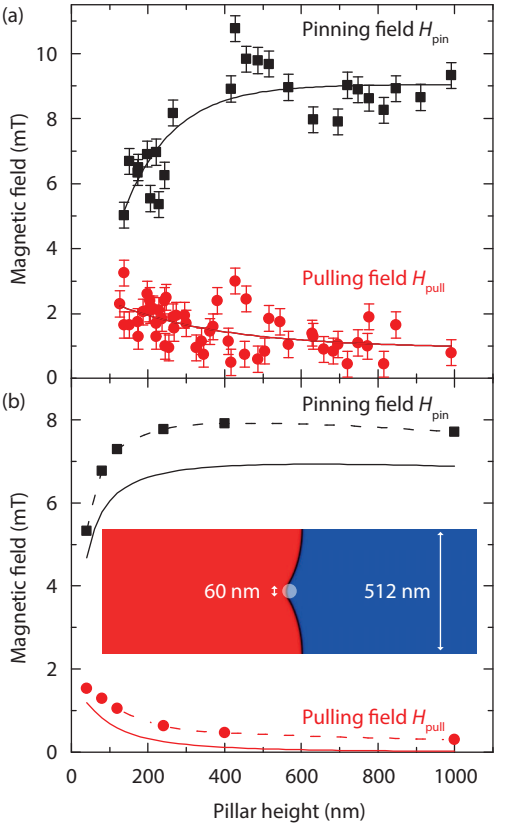

Figure 6.3 | (a) Measured pinning (black squares) and pulling fields (red circles) as a function of pillar height. The lines are to guide the eye. (b) (solid lines) Pinning and pulling field expected based on a 1D DW model. The behavior is confirmed by full micromagnetic simulations (squares and circles). The simulation snapshot in the inset show that the DW deviates from a 1D description by bending around the pillar (white circle) before depinning.

precursor gases[134,137,139], remnant magnetizations in the range $160 - 600\,\mathrm{kA/m}$ were found by Electron Holography TEM[134], so our result is at the lower end of this range. This is however beneficial for our experiment, since we observed in the simulations that a higher magnetization could lead to nucleation of a new domain rather than pinning of an existing DW in the conduit.

To confirm that our simplified 1D-model gives a reasonable estimate of the pinning potential, full 2D micromagnetic calculations of a DW moving underneath a pillar are also conducted[56]. The calculated pillar stray field maps are used as a position-dependent external field acting on a 512 nm wide, 0.5 nm thick strip with perpendicular magnetization. The strip has a saturation magnetization $M_s = 1400\,\mathrm{kA/m}$, uniaxial anisotropy constant $K_u = 1.5\,\mathrm{MJ/m^3}$, and exchange con-

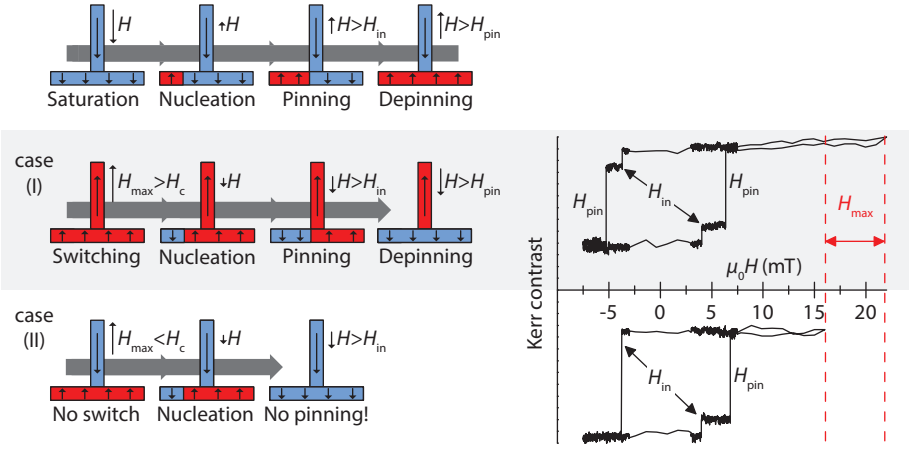

Figure 6.4 | (right) Hysteresis loops as a function of maximum positive field H_{max}; depending on H_{max}, the pillar either switches or does not switch, leading to symmetric (case I) or asymmetric (case II) hysteresis loops. This difference is explained by the cartoons on the left.

stant 16 pJ/m [82]. The magnetization of the pillar is assumed to remain fixed in the $-z$ direction. Starting from an artificially created DW on the left side of the pillar, we study how the DW moves to the right while increasing the applied field in small steps. The field at which the DW detaches from the pillar and moves out on the right of the strip is defined as the pinning field. Interestingly, it is observed that the DW does not retain a 1D profile but bends around the pillar because of the high stray fields underneath it (inset of Figure 6.3(b)). This, combined with additional contributions from the in-plane components of the stray field, leads to pinning fields that are slightly different but comparable in magnitude to the 1D-model. Repeating the simulations with varying pillar height reproduces the trend of increasing pinning field with increasing height (black squares in Figure 6.3(b)). The pulling field was also simulated by sweeping the field in the negative direction in order to move the DW to the left, and again the 1D-model trend was reproduced (red circles in Figure 6.3(b)).

6.4 Probing the coercive field of pillars

So far, it was assumed that the magnetization in the pillar remains fixed during the experiment. However, if the pillar itself switches with respect to the magnetization of the strip, the pinning behavior should also invert. In fact, this provides us with a unique tool to determine the magnetic state of the pillar. We exploit this to deduce the coercive field (or switching field) of the pillar from the DW pinning characteristics. Like before, we measure hysteresis loops in the region of interest around the pillar starting from high negative saturation, but this time we vary the maximum positive field H_{max} in each recorded loop, as seen in Figure 6.4. It is seen that there are two possible shapes of the hysteresis loop. The cartoons in Figure 6.4

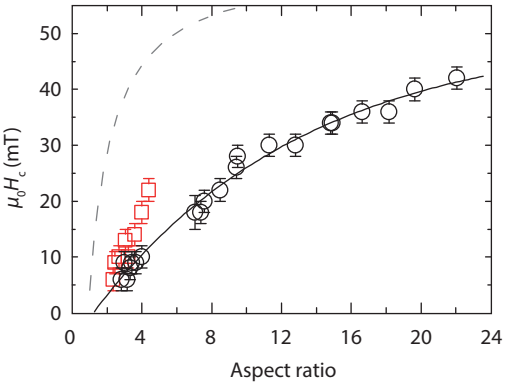

Figure 6.5 | Coercive field as a function of pillar aspect ratio. The solid line is a guide to the eye. The square red data points are outside of the trend because these pillars were grown under slightly different circumstances. The dashed grey line represents the coercive field of pillars based on the Stoner-Wohlfarth model.

schematically show what happens in the two cases. In case (I), H_{max} is higher than the coercive field of the pillar, so that the forward and backward sweep are completely symmetric. In that case, we start from a saturated state in both the forward and backward sweep of the loop (the top and middle row of cartoons, respectively), and observe the features of DW nucleation, DW pinning and DW depinning on both sides of the loop. In case (II) however, H_{max} is slower than the coercive field of the pillar, such that the pillar is not switched during the forward sweep, and the magnetization of the pillar and the DW conduit are not aligned when the backward sweep is started (bottom left cartoon in Figure 6.4). The new domain that is nucleated in the next cartoon, is now aligned with the pillar's magnetization and therefore easily moves underneath the pillar once it reaches it. The DW might experience the (much smaller) pulling field when it leaves the pillar on the right side, but this is not observable in the experiment since the pulling field is much lower than the injection field that was needed to bring the DW to the pillar in the first place. Therefore, no plateau is observed in the hysteresis loop during the backward sweep in case (II), which makes it possible to distinguish whether the pillar was switched or not.

The coercive fields are thus obtained simply by repeating the hysteresis loops at increasing H_{max} until symmetric (case I) behavior is observed. The results are plotted as a function of pillar aspect ratio (height divided by diameter) in Figure 6.5 (black circles). It is observed that at increasing pillar aspect ratio (height), the coercive field increases. This is qualitatively compatible with the coercive fields of magnetic cylinders calculated with the Stoner Wohlfarth model[156,157] assuming $M_{\mathrm{s}} = 100\,\mathrm{kA/m}$ like before (dashed grey line in Figure 6.5, see Appendix A.2 for calculation details). However, the coercive field saturates already at lower pillar aspect ratios in the model, compared to the experimental data. This implies that the Stoner-Wohlfahrt model, which assumes a single domain structure of the

pillar, probably represents a too simplified description, and switching mechanisms involving nonuniform magnetization might play a role [132,147,158]. This microscopic switching mechanism cannot be revealed with our measurement scheme and is therefore beyond the scope of this Chapter. In fact, we are mostly sensitive to the magnetization in the bottom part of the pillar, hence it cannot be guaranteed that the whole pillar switches together. In that case the data represents only the switching field of the bottom part, which might be different from the rest of the pillar. Finally, we would like to show that the switching field is strongly influenced by compositional variations. The red square data points in Figure 6.5 are representing pillars grown in the same vacuum but in a later run, where the precursor pressure had dropped leading to a lower growth rate. This also has an influence on the composition and this is reflected in a different coercive field compared to similarly high pillars grown at a higher pressure (red squares).

6.5 Conclusion & outlook

In conclusion, we have shown by both TEM and optical Kerr microscopy that FEBID-grown Fe nanopillars are magnetic and can be used to pin DWs in a PMA strip, where the pinning strength is tuned by the pillar height. The observed DW pinning was explained using a simplified 1D-model and supported by full micromagnetic simulations. By comparing simulations and experiment, the DW pinning process can in principle be used as a magnetometer for the pillar's magnetization, and a value $M_s \approx 100\,\mathrm{kA/m}$ was estimated. Furthermore, we exploited the fact that DW pinning depends on the magnetic orientation of the pillar, allowing us to determine the coercive fields of such nanopillars. The observed coercive field increases with the pillar aspect ratio, which was qualitatively explained with a Stoner-Wohlfarth model.

The use of DW motion as a probe of nanomagnetic objects is potentially interesting for use in sensors or lab-on-chip applications [87,88,159–161], as an alternative to more conventional magnetoresistive sensors [160,161] or anomalous Hall effect sensors [162]. We already mentioned previous studies demonstrating sensitivity of in-plane magnetized DW conduits to external ferromagnetic objects [80,152,153], and similar conduits were also shown to be sensitive to the presence of magnetic beads [143–146] used as markers in biosensors. Here, we applied such phenomena to technologically relevant PMA materials. As an example, one could devise an instrument that measures the absence, presence, magnetic moment, size or switch field of a single magnetic nano-object which lies on a DW conduit, by measuring the field that is required to move the DW past the object to a read-out position. As recognized by Vavassori *et al.* [146], the key fundamental advantage of using a DW for sensor purposes is the fact that the sensing area is determined by the DW width, which happens to be especially small in PMA materials ($\sim 10\,\mathrm{nm}$). Another advantage of a DW sensor is its high mobility, meaning that the position of the probed object does not matter as long as it is somewhere on the DW conduit. However, drawbacks are the fact that there usually occurs random pinning in the DW conduit of the order of 1 mT, which masks stray-field-induced pinning below this value, and the measurement scheme in its current form is rather complex.

Looking at applications of the pillars themselves, they could be used to selectively pin DWs of a certain polarity. This feature makes them less suitable for application in a current-driven DW shift register[7], where pinning sites should act equally on up-down and down-up DWs, but could be employed as a polarity filter in other applications such as DW logic. Since external magnetic objects such as our pillars do not appreciably alter the DW properties in the underlying DW conduit, they can be beneficial compared to pinning sites that are structured in the DW conduit itself[80,152]. Furthermore, the pillars' functionality can be reprogrammed by switching their magnetic state, enabling the fabrication of versatile magnetic logic devices.

6.6 Methods

Sample fabrication: The Pt/Co/Pt DW conduits were produced on Si / SiO_2 (100 nm) substrates by E-beam lithography using PMMA as resist, developed in MIBK, sputtered at an Ar pressure of $\sim 10^{-2}$ mbar (base pressure 2×10^{-8} mbar), followed by lift-off in acetone. On top of these conduits, the Fe pillars were grown in a dual-beam system (FEI Nova 600i NanoLab) at a precursor pressure between 2.06 and 4.12×10^{-6} mbar, using a focused electron beam operating at 5 kV and 0.4 nA. The pillar height was controlled by changing the dwell time between 10 and 30 s. Since the precursor pressure decreases during a deposition run, the exact height cannot be controlled accurately; therefore we measure the width and height of each individual pillar afterwards using SEM images. Dividing height by width gives the aspect ratio of a pillar. The pillars that were studied in the TEM microscope (JEOL ARM200FCS) were grown on an Omniprobe Cu Lift-Out grid under similar circumstances. *Stray field imaging:* The magnetic contrast in Figure 6.1(b-c) was obtained in DPC mode, where contrast arising from phase shifts of the electron beam wave-function from electrostatic and magnetic origins is detected by use of a segmented photo-diode detector. Obtaining difference images from opposing segments leads to grayscale phase contrast images with orthogonal directions of sensitivity. These grayscale component images are combined to produce a color vector representation of the phase contrast[149].

Kerr microscopy: Before recording the Kerr microscopy snapshots of the DW conduits in Figure 6.2(b), the sample was saturated in negative field and a background image was recorded at zero field. This background image has been subtracted to produce all shown subsequent images, so that only changes in the magnetization with respect to the saturated state are visible. The border that is seen around the Pt/Co/Pt strip is because of a slight drift of the sample after the background was recorded. The field is increased in small steps of 0.02 mT and the magnetic state is recorded after each step. This leads to an effective field sweep rate of approximately 0.1 mT/s limited by the acquisition time of the CCD camera. The magnetic contrast that is observed is only due to the DW conduit, since the Kerr signal from the vertical pillars is negligible.

Details of the stray field and switching field modeling are presented in Appendix A.

Part II

Current-induced effects

Introducing current-induced effects 7

The origin of current-induced DW motion in PMA materials has been the subject of intense debate in the past years, because conflicting results were reported on the magnitude and even the direction of the effect. This introductory chapter presents the context in which our experiments on current-induced effects were conducted. It starts with the conventional description of DW motion based on spin-transfer torque. Then, it is described how the spin-orbit coupling can give rise to two additional torques, together called spin-orbit torques, and their influence on magnetization dynamics is briefly introduced. Afterwards, we introduce an additional contribution to the magnetic energy due to the Dzyaloshinskii-Moriya interaction, which can influence the DW structure and thereby influence DW motion. We end with an overview of the chapters that follow this introduction, where we perform experiments with the ultimate goal of identifying the main mechanisms that dominate the controversial current-induced DW motion in PMA materials.

7.1 Conventional spin-transfer-torques

As mentioned at the very start of this thesis in Chapter 1 (Introduction), current-induced DW motion (CIDWM) is 'conventionally'[10] described as the result of two torques acting on the DW when a current runs through it, visualized in Figure 1.3(a). The most straightforward torque is the *adiabatic* spin-transfer torque (STT), which exists because of the following. A current that runs through a ferromagnet becomes spin-polarized, since there is a difference in the density of states at the Fermi level between majority and minority spins. At the DW, in the case of a transition metal, the spin of the (4s-)electrons adiabatically follows the magnetization, through an interaction with the localized (3d-)electrons responsible for the magnetization, which Berger called the *s-d exchange* force[4]. Because of spin angular momentum conservation, the torque on the conduction electrons leads to a reaction torque on the localized 3d-electrons themselves, which causes the DW to be pushed in the direction of electron flow.

The second, *nonadiabatic* STT was introduced in order to explain unexpected early experimental results[11–16], where DWs were seen to move already at lower

values of the current than expected. The origin, as well as the magnitude of this nonadiabatic contribution has been the subject to scientific debate [9,10,17,163] which is still not fully resolved, and we will elaborate on this later in section 7.1.2.

7.1.1 Modified LLG equation

Irrespective of the microscopic origin of the nonadiabatic contribution, both STTs can be added to the LLG equation that governs magnetization dynamics [10]:

$$\frac{\partial \mathbf{m}(t)}{\partial t} = \underbrace{-\gamma\mu_0 \mathbf{m}\times\mathbf{H}_{\text{eff}}}_{\text{precession}} + \underbrace{\alpha \mathbf{m}\times\frac{\partial \mathbf{m}(t)}{\partial t}}_{\text{damping}} - \underbrace{(\mathbf{u}\cdot\nabla)\mathbf{m}}_{\text{adiabatic}} + \underbrace{\beta \mathbf{m}\times(\mathbf{u}\cdot\nabla)\mathbf{m}}_{\text{nonadiabatic}}, \tag{7.1}$$

where $\mathbf{m} = \mathbf{M}/M_s$ represents the magnetization direction. The first two terms form the original LLG equation, representing precession around the (effective) magnetic field $\mathbf{H}_{\text{eff}}$, and the phenomenological Gilbert damping term describing all dissipation channels that eventually lead to an equilibrium magnetization. The third, adiabatic term is easily derived from spin angular momentum conservation as described above, where the role of the current is captured by the vector $\mathbf{u}$, the *spin drift velocity*,

$$|\mathbf{u}| = u = \frac{g\mu_B P J}{2eM_s}, \tag{7.2}$$

pointing along the electron flow direction. Here, g is the Landé factor ($\sim$2), J is the current density, P is the spin polarization of the current and e is the elementary charge.

The nonadiabatic term is phenomenologically introduced in (7.1) [10] and its strength is characterized by the parameter β. The implications of this parameter on CIDWM can be enormous. This can be observed by studying the equations of motion of a DW based on the extended LLG equation (7.2), but integrated over all space assuming the 1D profile of the DW which we introduced in (2.7) [10]

$$\dot{\phi} + \alpha\dot{q}/\lambda = \gamma\mu_0 H_{\text{ext}} + \beta u/\lambda, \tag{7.3a}$$

$$\dot{q}/\lambda - \alpha\dot{\phi} = \gamma\mu_0 H_K \sin\left(2\phi\right)/2 + u/\lambda. \tag{7.3b}$$

In this 1D approximation, the degrees of freedom of the DW are its position along the nanostrip, q, and its internal angle, ϕ. The values $\phi = 0\,\text{or}\,\pi$ and $\phi = \pm\pi/2$ represent the Néel and Bloch wall structure, respectively, introduced before in Figure 1.2. $H_K = 2K_d/\mu_0 M_s$ is the DW anisotropy field, corresponding to the energy barrier K_d between the Bloch and Néel states, and λ is the DW width, assumed constant during the dynamics.

Figure 7.1 shows typical solutions to these coupled equations of motion, for various values of β. Plotted is the speed of DW motion, as a function of the current (represented by u). It is seen that β has a huge influence, especially in the low current regime. In fact, if $\beta = 0$, DWs do not move at low current: they exhibit *intrinsic pinning*. That is due to the precessional nature of the adiabatic STT: it tilts the DW away from the stable wall structure (usually Bloch, $\phi = \pm\pi/2$), but

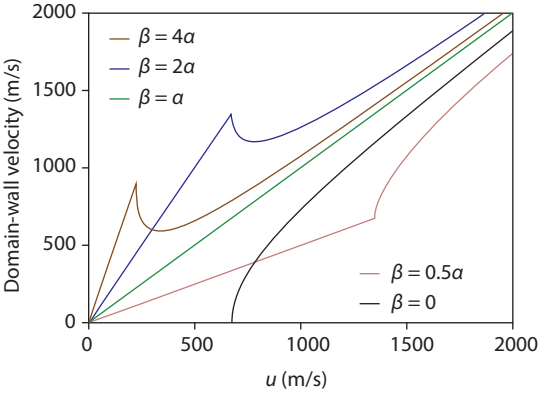

Figure 7.1 | Simulated DW velocity versus current for various values of β. Adapted from [10].

the torque needs to be strong enough to do so, otherwise the DW remains stationary. If the STT can tilt the DW over a critical angle, the DW will start to precess, and this precession is associated with forward motion, in a phenomenon called *Walker breakdown*[164] *. If β is finite, however, DWs are not intrinsically pinned. That is the reason why this term was introduced in the first place: early experiments[11–16] displayed DW motion at much lower currents than the intrinsic critical current density that was calculated from micromagnetic simulations[165]. A small critical current was still present due to randomly occurring *extrinsic* defects which locally reduce the DW energy, similar to our engineered pinning sites in Part I of this thesis.

Looking at the equations of motion, we can see that the β term enters as an effective magnetic field. Therefore, to measure β, it is very convenient to extract β from the equivalence between field and current. This works especially well in the low current limit (far below the intrinsic critical current density), where the influence of the adiabatic torque can be neglected. In a typical experiment, DWs are depinned from a (either engineered or natural) pinning site by a magnetic field, and one measures the reduction or enhancement of the required field as a function of current. Based on (7.3), we know that simply $\beta = \gamma\mu_0\lambda\frac{\mathrm{d}H}{\mathrm{d}u}$. This is a quite robust scheme, since the low current density leads to a negligible influence of dissipative Joule heating, and it also does not rely on the interpretation of complex (precessional) DW dynamics which may be influenced by many factors.

7.1.2 The β controversy

Up until now, we completely stepped over the microscopic origin of β, and only described its phenomenological effect on DW motion. However, since its introduc-

*In Chapter 4, we already employed this phenomenon to let a DW precess, only in that case the DW was kept at a stationary position by introducing a pinning site.

tion, the β parameter has been subject to a lot of debate amongst theorists and experimentalists alike, as several different mechanisms could describe it[10]. As mentioned, this torque is ascribed to a deviation from the simple adiabatic tracking of the magnetization by the conduction spins. DWs in perpendicular magnetized materials are usually very narrow, resulting in very high magnetization gradients. Therefore, it is expected that conduction electrons cannot adiabatically follow the magnetization, resulting in mistracking between the s- and d- electrons of the current and magnetization, respectively. This mistracking could lead to a nonzero nonadiabatic torque[166–168] perpendicular to the adiabatic one. A second contribution to the nonadiabatic torque could arise when there is spin relaxation in the DW[9,169]. This spin relaxation can occur due to spin-flip scattering without spin conservation, which can become important in high spin-orbit coupling materials.

This discussion on β initially focused on DW motion in in-plane magnetized materials, in particular the well-known material permalloy ($Ni_{80}Fe_{20}$). A lot of experimental studies on β were published, from which no consensus has yet emerged[25]. In general one could say that, in particular for the complicated vortex wall structure that occurs in relatively wide nanostrips, β is much larger than the damping constant α[25]. Still, the origin of β in permalloy was never completely clarified, and likely β is a combination of multiple effects.

The reason permalloy was initially studied, is because it has some advantages for racetrack memory such as a high spin polarization and low DW pinning at defects. The low DW pinning originates from the fact that DWs are very wide in this material ($\sim 100\,\mathrm{nm}$), which on the other hand is a big drawback since it limits the areal information storage density. Furthermore, experiments identified some other drawbacks, such as a high critical current density, and the complexity of the wall structures which may unexpectedly transform into each other, influencing the dynamics[25]. For this reason, the attention has really shifted to out-of-plane magnetized (PMA) systems, which exhibit narrow DWs with a simple and more rigid Bloch or Néel structure, and therefore a high data storage density and potentially a larger nonadiabatic torque with better reproducibility.

The β discussion continued in these PMA materials, where the contradiction between experiments became even more apparent. Not only was there a large spread in measured β depending sensitively on the material, there even was confusion over the *direction* of the DW motion. We will not bother the reader with an enumeration of all experiments, but refer to[25] (Tables 1&2 therein) for an elaborate overview. The explanation for the surprising inversion of DW motion was sought in various directions, such as a negative β, a negative spin polarization, and finally in potentially new sources of current-induced spin torque. Experiments conducted in our group by Lavrijsen revealed that the application of in-plane fields can crucially influence the DW motion[28], and also the precise stacking order in Pt/Co/Pt with different Pt thicknesses can lead to a sign change of the DW motion[29]. This thesis work started in the heat of that discussion, and started off by studying a property that might be intimately related to the nonadiabaticity parameter: the *DW resistivity*.

7.1.3 DW resistivity due to spin mistracking

In order to shed light on the β controversy, we aimed at finding a correlation between the β term in DW motion, and other related properties. The electrical resistivity of DWs is a significant research field by itself[170], which also deals with spin-dependent transport in magnetization textures. This field aims at explaining why there is a resistance change between a homogeneously magnetized strip, and the same strip that is prepared in a multidomain state. In fact, it has been proposed a long time ago by Levy and Zhang[171] that the DW itself leads to an intrinsic contribution to the resistivity of a magnetic strip, if the conduction spins do not adiabatically follow the magnetization. In other words, mistracking of electrons can give rise to a significantly increased scattering rate inside the DW, hence an increased resistivity, while the same mistracking was also proposed to lead to the β term. This lead us to perform a systematic study of the DW resistivity as a function of the main parameter that governs this mistracking: the DW width λ.

In fact, when we started out these experiments, our aim was to gather a complete dataset of the DW resistivity *and* the β parameter as a function of the DW width. However, although we will demonstrate a very clear dependence of the resistivity on the DW width in Chapter 8, measurements of β turned out to be hardly reproducible. Based on our findings in the later Chapter 9, we know with hindsight that the measured β were very strongly influenced by small accidental field misalignments and small details of the material configuration. We found that it is not β, but a *spin-orbit torque* caused by the spin Hall effect that dominates the DW motion.

7.2 Spin-orbit torques

Spin-orbit torques (SOTs) are a generic term for additional spin transport phenomena that can occur in systems with high spin-orbit coupling. Here, we sketch a brief history of how additional torques due to spin-orbit coupling effects were proposed to explain confusing DW motion results. Thereafter, we will briefly discuss the origin of the two prominent spin-orbit torques, due to the Rashba effect and the spin Hall effect, respectively, before describing their effect on the magnetization dynamics.

7.2.1 Early work

Although it is hard to pinpoint the 'birth' of SOTs as an effect on DW motion, one particularly pioneering report was done by Moore, Miron, *et al.*[26]. They were the first to report high DW velocities exceeding 100 m/s (albeit at current densities exceeding 10^{12} Am^{-2}) in the material Pt/Co/AlOx. The reason for this high velocity was initially attributed to a high β. The real surprise came later, however, when they published an erratum stating that the DWs had not moved with, but *against* the electron flow direction[27]. Not much later, the group published a different study on the same material, where they claimed the existence of a large current-induced transverse *Rashba magnetic field* in the y-direction, as evidenced by an asymmetry in the domain nucleation rate as a function of applied transverse fields[172]. Not

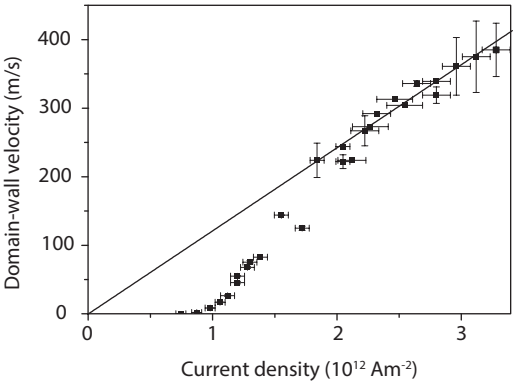

Figure 7.2 | Measured DW velocity as a function of current density in Pt/Co/AlOx. A transition from the slow 'creep' behavior to the flow regime is observed, with no indication of Walker breakdown. Adapted from [30].

surprisingly, they later used these findings to explain DW motion in this material as well [30].

Figure 7.2 represents their main experimental result. It is seen that the DW velocity is high and scales linearly with the current in the high current regime. To explain the high magnitude of the slope, a very high $\beta \approx 1$ was required, but since this $\beta \gg \alpha$, a Walker breakdown should occur based on the simulations we showed before in Figure 7.1. They attributed this absence of Walker breakdown to the strong Rashba y-field that stabilizes the Bloch wall. This suppresses any changes to the DW structure, hence the DWs are rigid Bloch walls which are moved at high efficiency by the large β contribution. Still, the inverted direction of DW motion remained a mystery, hence the controversy was far from solved. Note that in the low current regime, the DW velocities are much lower than expected based on the simulations (straight line). This is due to the strong extrinsic pinning that is present in these PMA materials, a phenomenon known as thermally activated *creep motion* which has been known for a long time in the context of field-driven motion [83,89]. The fact that current- and field-driven DW motion give equivalent results indeed suggests that the current acts as an effective field similar to the β-contribution, but this interpretation is doubtful because of the unexpected direction of DW motion.

The experiments detailed in this Part of the thesis aim at explaining these phenomena, such as the observed sign changes of DW motion as well as the role of in-plane magnetic fields. We will now briefly introduce the Rashba effect and the spin Hall effect, both of which can potentially explain these fascinating observations.

7.2.2 Rashba effect

The first of the spin-orbit torques originates from the Rashba effect [173]. This effect can arise when there is an electric field gradient due to symmetry breaking at an

interface. Although first identified in semiconductors, the effect could also arise in metallic ferromagnets, in particular in a system consisting of a metal with large spin-orbit coupling, a ferromagnetic layer, and an oxide layer[174]. A simple sketch of this effect is presented in Figure 7.3. Due to an asymmetric crystal field potential at the interface between two different materials, electric fields E can build up at the interfaces when a lateral current flows through the layer system. In a classical picture, these electric fields transform to magnetic fields H_R in the rest frame of the electrons flowing at the interfaces. This effective field couples to the magnetic moment of the adjacent magnetic layer through the s-d exchange interaction. This can be modeled simply as an effective magnetic field in the y-direction transverse to the current flow.

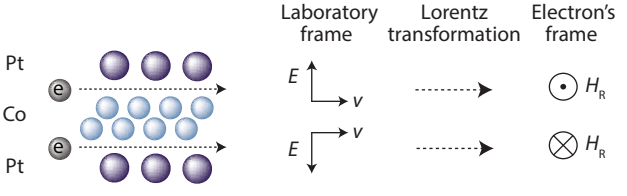

Figure 7.3 | Classical explanation of the Rashba effect. An asymmetric crystal field at the interfaces leads to effective electric fields E, which transform to magnetic fields H_R in the rest frame of the electron. This couples to the magnetization through the s-d exchange interaction. After [175].

The key ingredients to achieving a significant Rashba effect are a strong spin-orbit coupling (characterized by the Rashba parameter α_R), a strong effective electric field at the interfaces, and a strong structural inversion asymmetry (SIA), i.e. asymmetry between the top and bottom interfaces. For this reason, Pt/Co/Pt seems unlikely to exhibit a significant Rashba effect, since it lacks the asymmetry between top and bottom interfaces. Indeed, Miron *et al.* found no indication of a Rashba field in symmetric Pt/Co/Pt[172], whereas in Pt/Co/AlOx on the other hand, they claimed a Rashba field of up to 1 T[30,172].

In addition to this effective field, a secondary torque due to the Rashba effect was predicted to occur[174,176,177], perpendicular to the first. This 'nonadiabatic' contribution to the Rashba effect can be caused by spin diffusion inside the magnetic layer[174,176]. In Section 7.2.4, we will discuss how these torques enter the LLG equation.

7.2.3 Spin Hall effect

The spin Hall effect was first proposed by Dyakonov and Perel[178,179] although its current name was introduced much later by Hirsch[180]. It describes how spins accumulate at the interfaces of certain materials, due to spin-dependent deflections of electrons in the directions transverse to the current flow direction, as sketched in Figure 7.4. When a ferromagnetic layer is present on top of such a spin Hall material, the vertical spin current (polarized in the y-direction) can be injected

into it. The maximum *perpendicular* spin current J_s induced by a *longitudinal* charge current density J is characterized by the *spin Hall angle* θ_{SH},

$$J_s = \theta_{SH} J. \tag{7.4}$$

This spin current is injected into (and absorbed by) the magnetic layer, exerting a torque on the magnetization because of angular momentum conservation. A similar process was first studied by Slonczewski[6], who used a perpendicular charge current that is polarized by a reference magnetic layer. Apart from the different generation of the spin current, the torques are the same, and therefore we call it a Slonczewski-like torque.

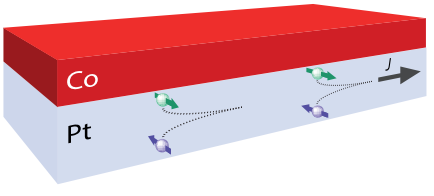

Figure 7.4 | The spin Hall effect leads to a transverse deflection of spins in Pt. With respect to the current flow, right-oriented spins flow up and left-oriented spins flow down. A pure left-polarized spin current is therefore injected into the adjacent Co layer.

After the initial predictions, it took over 30 years to experimentally demonstrate the existence of the the SHE, first in semiconductors[181,182], and later in metals such as Pt[183,184]. There has been a lot of debate on the magnitude of the spin Hall angle in Pt, with experimental results varying by a factor 20 depending on the experimental scheme that was used[185]. Recently, Liu *et al.*[31] experimentally showed that the spin Hall angle is large enough ($\theta_{SH} = 0.07$) to induce switching of an adjacent magnetic layer (see also section 7.2.5). Even more recently, surprisingly large spin Hall angles were found in Ta[85], and W[186] as well.

Regarding the origin of the spin-dependent deflections that cause the SHE, several mechanisms exist, and different mechanisms dominate in different materials. This fact even manifests itself in a different *sign* of the spin Hall angle in, for example, Ta as compared to Pt. In Pt, with its heavy intrinsic spin-orbit coupling, the dominant contribution is the *intrinsic* spin Hall effect[63]. This originates from a spin-dependent Berry curvature in k-space, a topic that is difficult to grasp intuitively (an attempt is made in the master thesis of Haazen[175]). In other materials, there are two *extrinsic* contributions related to impurities: side-jump[187] and skew scattering[188]. The side-jump describes the lateral shift in the position of a wave packet during collision with impurities, and is actually governed by the same physics as the intrinsic contribution, applied to the impurity potential[63]. The skew-scattering process is somewhat more straightforward and arises from the fact that the momentum of an electron is altered spin-dependently after scattering with an impurity. Upon scattering from a positively charged impurity, an electron briefly

experiences an electric field. Through spin-orbit coupling, this electric field transforms to an inhomogeneous magnetic field in the reference frame of the electron, leading to a force with a direction depending on its spin. This extrinsic contribution seems especially interesting for engineering materials with a high spin Hall angle. In a recent theoretical paper [189], perfect alloys for SHE-induced switching were explored, and it was identified that the skew-scattering contribution to the spin Hall angle can be made very large by adding a small percentage of (heavy) impurities to materials like Cu or Ag.

7.2.4 LLG-equation with spin-orbit torques

Having introduced the two sources of spin-orbit torques, we now describe how they enter in the LLG equation that governs magnetization dynamics. As discussed before, the Rashba effect acts as an effective field in the y-direction, hence the torque it exerts is often called a field-like (FL) torque and has the form, [172,190]

$$\boldsymbol{\tau}_{\text{Rashba}} = -\tau_{\text{FL}}^{\text{Rashba}}(\mathbf{m}\times\hat{\mathbf{y}}), \quad \text{with } \tau_{\text{FL}}^{\text{Rashba}} = \frac{\gamma\alpha_{\text{R}}JP}{\mu_{\text{B}}M_{\text{s}}}. \tag{7.5}$$

Here, γ is the gyromagnetic ratio, μ_{B} is the Bohr magneton, P is the spin polarization in the ferromagnetic layer, and α_{R} is the Rashba parameter averaged over the magnetic film thickness.

The spin Hall effect on the other hand, acts as a y-polarized spin current that is injected into the magnetic layer, and therefore has the form of a Slonczewski-like (SL) torque as mentioned in the previous section, mathematically described by [191]

$$\boldsymbol{\tau}_{\text{SHE}} = -\tau_{\text{SL}}^{\text{SHE}}(\mathbf{m}\times\hat{\mathbf{y}}\times\mathbf{m}), \quad \text{with } \tau_{\text{SL}}^{\text{SHE}} = \frac{\gamma\hbar\theta_{\text{SH}}J}{2eM_{\text{s}}t}, \tag{7.6}$$

where t is the thickness of the ferromagnetic layer.

Since the two effects take a different form in the LLG equation, it is possible to separate the two contributions by measurements of the magnetization dynamics. However, several theorists recognized that both the Rashba and the spin Hall effect can have a 'nonadiabatic' counterpart [174,176,192,193]. This makes it less straightforward to distinguish the two effects, since the nonadiabatic Rashba torque has the same SL form as the direct SHE torque, and the nonadiabatic SHE torque takes the FL form of the direct Rashba torque.

The nonadiabatic Rashba torque $\tau_{\text{SL}}^{\text{Rashba}}$ originates from spin diffusion within the ferromagnetic layer, and is generally expected to be smaller than the direct Rashba torque $\tau_{\text{FL}}^{\text{Rashba}}$ [176,192]. However, in extreme cases (layer thicknesses smaller than the spin dephasing length) it was calculated that it could be even slightly larger than the direct Rashba effect [174]. In any case, if the direct Rashba is negligible, the nonadiabatic term also vanishes. Therefore, from an experimental point of view, we can say that if a large τ_{SL} is measured while τ_{FL} is very small, this excludes the Rashba effect as a significant contributor.

Similarly, the spin Hall effect can have a nonadiabatic FL contribution $\tau_{\text{FL}}^{\text{SHE}}$. The possibility of the latter contribution is mainly inspired by observations of spin torques induced through magnetic tunnel junctions, where this effect can be very

large, but it does not play a significant role when all transport takes place in metals [193–195], like in our situation. Therefore, if we measure a significant τ_{FL}, it likely originates from the Rashba effect rather than the SHE.

7.2.5 Spin-orbit torque switching

As briefly mentioned in section 7.2.3, spin-orbit torques can be strong enough to completely reverse the magnetization of either an in-plane [85], or out-of-plane [31,84] magnetized layer. Here, we discuss these experiments in a bit more detail, since they inspired us to study the effect of spin-orbit torques on DW motion. The experimental situation is sketched in Figure 7.5. As first reported by Miron [84], a current pulse running through a Pt layer, leads to switching of the perpendicular magnetization of an adjacent Co layer. In order to achieve this, an in-plane field H_x (anti-)parallel to the direction of current flow needs to be applied, which slightly cants the magnetization. By inverting the current direction, the magnetization can be switched back, and inverting the in-plane field also changes the sense of switching. To explain such switching behavior, a SL torque is required. In the original interpretation of Miron, this SL torque was attributed to the nonadiabatic contribution of the Rashba torque. However, in a very similar experiment by Liu *et al.* [31], the authors came to a different conclusion. They could quantitatively explain all the features of the switching behavior using the SHE. Furthermore, they argued that if the Rashba effect was to be responsible for the SL torque, it should be accompanied by an even bigger FL torque. Evidence for such an FL torque should occur when changing the in-plane direction of the applied field, and they found no significant FL torque. Thereby, they made a strong point in favor of the SHE as the dominant switching mechanism.

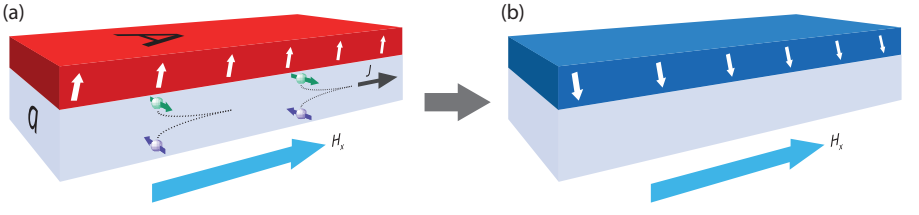

Figure 7.5 | Spin Hall switching. (a) Starting from a saturated 'up' state, with its magnetization slightly canted due to the external H_x field, a spin Hall current is injected. The torque exerted by the injected 'green' spins switches the magnetization to the 'down' state shown in (b).

The SHE induced switching is very interesting for use in memory applications similar to MRAM. In a conventional MRAM device, a vertical charge current is used, which becomes spin polarized in a first, magnetic layer, and then exerts a SL torque on a second, switchable free layer. However, the spin polarization of a charge current can fundamentally not exceed unity. A spin current from the SHE does not have this fundamental limit, since the charge and spin currents are separated [31].

The charge current only flows through the cross-sectional area of the Pt strip a, whereas the spin current flows through the injection interface between the Pt and Co layer characterized by the area A (see Figure 7.5). Therefore, the ratio of spin current to charge current is given by $\theta_{\mathrm{SH}} \cdot A/a$, which easily exceeds unity. This is one of the reasons why the SHE is very promising for a new type of MRAM.

However, a drawback of SHE induced switching is the external H_x-field that needs to be applied, which is not desirable in an integrated circuit. This field cants the magnetization a little bit and breaks some of the symmetry that is present in the system. Without this broken symmetry, there is no reason why the magnetization would prefer to end up in any of the two states upon injection of the transversely polarized spin current, as we will argue in Chapter 9 from symmetry arguments.

Nevertheless, inspired by these very efficient switching experiments, we successfully reproduced them in Pt/Co/Pt samples (see Chapter 9), in which we measured no significant Rashba-like torque. This is in line with the claims of Liu *et al.* [191]. Realizing the important implications that such a SHE torque can have on DW motion, we performed DW depinning experiments as a function of H_x. Very low currents were used, such that the SHE torque is too weak to induce switching of a single-domain state. Still, the SHE produced by this small current does exert a significant torque on the DW region and moves the DW, but only if it is forced to the Néel state by the symmetry-breaking H_x field, in line with theory. Additional information is gained by varying layer thicknesses: the net spin Hall current strongly depends on layer thicknesses, and so do the measured effects, providing a strong indication of DW motion governed by the SHE.

7.3 Dzyaloshinskii-Moriya interaction

In the previous section, several current-induced spin-orbit torques were introduced which can lead to magnetization dynamics and could potentially influence DW motion. The key to the existence of these torques is a high spin-orbit coupling, combined with structural inversion asymmetry (SIA): if the top and bottom interface/layer are completely symmetric, all mentioned effects should cancel out. However, not only does SIA play a role in these current-induced effects, it can also influence the *static* magnetization configuration, through an effect called the *Dzyaloshinskii-Moriya interaction* (DMI).

The DMI is an *anisotropic* exchange contribution that is allowed in systems with broken symmetry in the presence of spin-orbit coupling. It leads to spin structures of a certain chirality being favored over the opposite chirality. In order to explain this, let us first consider a highly symmetric system of two spins, as sketched in the top of Figure 7.6(a). Going from the left to the right spin, the magnetization rotates counterclockwise. We perform two energy-conserving symmetry operations: rotation around the x-axis and spin inversion. The result is the same system, but now with a clockwise rotation of the magnetization. Hence, the clockwise and counterclockwise configurations have the same energy. This is to be expected from direct, isotropic exchange: the exchange energy simply depends on the relative orientation of the spins.

However, the situation changes when the exchange between the two sites is mediated through spin-orbit coupling by a third site, for example a Pt ion, that is

situated *above* the original sites, as shown in Figure 7.6(b). Clearly, this system has a reduced symmetry compared to the initial situation. In this situation, the same symmetry operations can be used to transform from a counterclockwise to a clockwise rotation, but now the Pt ion is situated *below* rather than above the spins, hence represents a 'sample' different from the original one. Therefore, within the original sample, symmetry allows for a different energy of the two *chiralities*, because of the different orientation of the spins with respect to the third ion.

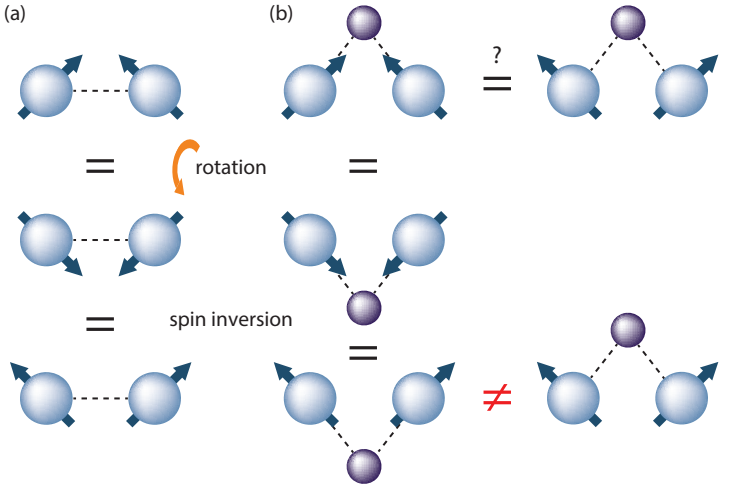

Figure 7.6 | DMI from symmetry arguments. (a) In a symmetric system, a left-handed spin configuration (top) can be transformed to a right-handed configuration without changing the energy. (b) Applying the same transformations to a system including a symmetry-breaking third ion, it is not possible to transform the handedness without changing the relative position of this ion, hence the energy can depend on the chirality.

The possibility of a mediated exchange interaction was introduced under the name superexchange by Kramers and Anderson [196] and was first used to explain antiferromagnetism in crystals like MnO. Purely on symmetry grounds, Dzyaloshinskii [197] realized that, in crystals with reduced symmetry, this could give rise to an anisotropic exchange interaction between two spins, of the form

$$\mathbf{D} \cdot \left(\mathbf{S}_i \times \mathbf{S}_j \right). \tag{7.7}$$

Later, Moriya [198] identified that such a term could be large when mediated by the spin-orbit coupling. Due to this coupling, the spins interact with the wavefunction of the third ion. Therefore, the wavefunction overlap that leads to exchange depends on the orientation of the spins with respect to the position of the third ion, giving rise to an anisotropic exchange contribution.

Although this term was first introduced in the context of low-symmetry crystals, Fert was first to mention that it could also be important at the interface of

ultrathin films [199]. Many years later, the DMI indeed revealed itself experimentally through chiral spin structures that were observed in epitaxial magnetic mono- and bilayers by spin-polarized scanning tunneling microscopy [200,201]. If the DMI is so strong that it even dominates over the symmetric exchange interactions, this leads to a spatially rotating magnetic ground state [200], or a ground state with vortex-like textures known as skyrmions [202,203]. In a perpendicular magnetic bilayer of Fe on W [201], it was found that the DMI determines the chirality of the DWs, which were of the Néel type. Next to these observations on epitaxial systems, by the end of this thesis (Chapter 10) we will see that this can also be the case in relatively disordered ultrathin Pt/Co systems grown by sputter deposition, if sufficient asymmetry is present [204–206].

To understand why the DMI favors Néel walls rather than Bloch walls, we can write (7.7) in terms of magnetization gradients in a 2D ultrathin film, [204]

$$E_{\mathrm{DMI}} = D\left[m_z\frac{\partial m_x}{\partial x} - m_x\frac{\partial m_z}{\partial x} + m_z\frac{\partial m_y}{\partial y} - m_y\frac{\partial m_z}{\partial y}\right]. \tag{7.8}$$

In the case of a nanostrip with a confined width, one may assume there are no gradients in the y-direction and the last two terms vanish. Then, it is easily seen that the energy within the DW depends on its orientation in the x direction: if we invert m_x, both energy terms change sign. The same goes for an inversion of m_z. Therefore, assuming a positive D, if m_z rotates from up-to-down the DW minimizes its energy by orienting itself along $-x$, whereas in a down-to-up configuration the DW energy is minimal along $+x$. This way, the sense of rotation (left-handed versus right-handed) should always be the same when DMI is present. However, the strength of D has to be strong enough to overcome the DW shape anisotropy H_K which favors Bloch walls, which was already introduced in (7.3). Furthermore, the in-plane orientation of the DW can be tuned by an externally applied magnetic field. In Chapter 10, a formula for all ϕ-dependent contributions to the DW energy will be given, which is needed to explain our experimental results.

A peculiar coincidence occurs in materials like Pt/Co/AlOx. Owing to the spin Hall effect in the Pt layer on one side, a longitudinal current is transformed into a vertical spin current that can only move Néel DWs (Chapter 9), and the direction of motion depends on the DW chirality. At the same time, the structural inversion asymmetry in this system leads to the stability of only one particular Néel DW chirality. Combining these two effects, all DWs will be moved in the same direction by the spin Hall current, as has recently been shown in [204–206]. In Chapter 10, we will confirm that this is the case, and tune the structural inversion asymmetry to observe a gradual transition from Bloch wall stability to Néel wall stability.

7.4 In this Part

Having introduced the context in which this thesis work was conducted, we now briefly discuss the Chapters that follow, and how they are mutually related.

Motivated by the surprising results on DW motion in Pt/Co/Pt, we study the related DW resistivity property in **Chapter 8**. We will show that the resistivity of

DWs decreases with $1/\lambda^2$, in line with the theory of Levy and Zhang based on spin mistracking. This suggests that the β that was measured in these materials originates (at least partly) from spin mistracking.

Therefore, in **Chapter 9**, we measure the β-like contribution on DW motion by studying current-assisted DW depinning from a Ga-irradiated pinning barrier, and conclude that β does not play an important role in Pt/Co/Pt. We observe that when a longitudinal H_x field is applied, the efficiency (β) of DW motion rises from almost zero to a high value. By varying the stacking order and the DW polarity, we will show that the spin Hall effect has the correct symmetry and magnitude to explain the strong influence of the longitudinal field, whereas Rashba effects are negligible.

Finally, in **Chapter 10**, we revisit the SHE-induced DW depinning in Pt/Co/Pt, inspired by the observed influence of DMI in systems with stronger inversion asymmetry [205,206]. We observe that, although the bottom and top layers are made of the same material, there is actually a small, tunable DMI contribution that gives the DWs a slight Néel character, even at zero in-plane field. Performing similar experiments on Pt/Co/AlOx, we argue the DW motion is governed by exactly the same mechanism, only much more efficiently due to a strong built-in chiral field. This is also a more likely explanation to the DW motion experiments of Miron *et al.* [30,204] and given the sensitive influence of layer thickness and material, it might also explain the discrepant results found by many others [25]. Finally, we employ our DW resistance toolkit that was developed in Chapter 8, to provide more direct evidence that the in-plane fields influence the DW structure in Pt/Co/Pt, and show that H_x indeed forces the Néel wall that is efficiently moved by the SHE. These developments are promising for a SHE driven racetrack memory, since it provides endless ways to optimize the efficiency by engineering the interfaces and the adjacent materials, in order to tune the DMI [205,206] and the SHE [189].

Measuring the resistivity of individual magnetic domain walls

8

Despite the relevance of current-induced magnetic DW motion for new spintronics applications, the exact details of the current-DW interaction are not yet understood. A property intimately related to this interaction is the intrinsic DW resistivity. Here, we investigate experimentally how the resistivity inside a DW depends on the wall width λ, which is tuned using focused ion beam irradiation of Pt/Co/Pt strips. We observe the nucleation of individual DWs with Kerr microscopy, and measure resistance changes in real-time. A $1/\lambda^2$ dependence of DW resistivity is found, compatible with Levy-Zhang theory. Also quantitative agreement with theory is found by taking full account of the current flowing through each individual layer inside the multilayer stack. *

8.1 Introduction

Current-induced motion of DWs in magnetic nanostrips is an actively investigated topic [25], because of possible application in memory and logic devices [7]. Although successful DW motion has been shown, details of the interaction between current and DWs remain unclear. In particular, the magnitude of the nonadiabatic torque varies greatly, especially in the case of perpendicularly magnetized materials [40,41,207], and also theoretical work [9,166,168] is focusing on various underlying physical mechanisms. It is suggested that this nonadiabatic contribution could arise when there is mistracking between the spin of conduction electrons and the local magnetization, which is also believed to be the origin of the electrical resistance induced in DWs. Systematic measurements of DW resistivity, which is the focus of the present Chapter, are therefore of crucial importance in unraveling the physics behind nonadiabatic spin torque.

Several effects can lead to resistance changes when a DW is introduced into a magnetic system. One effect is the anisotropic magnetoresistance (AMR), which always occurs when the magnetization gains a component parallel to the current

*Published as: *Tunable resistivity of individual magnetic domain walls*, J. H. Franken, M. Hoeijmakers, H. J. M. Swagten, and B. Koopmans, Physical Review Letters **108**, 037205 (2012).

flow and is therefore not intrinsic to the DW. Various mechanisms can lead to *intrinsic* DW resistivity (DWR) [170]. Viret *et al.* [208] first treated resistance due to spin mistracking semi-classically; the DW represents a magnetic field rotating over a distance λ (DW width) in the rest frame of an electron moving at the Fermi velocity v_F, and the electron spin can only follow this field adiabatically if the precession frequency ($2J_{sd}/\hbar$) of the spin about the exchange field is much larger than the rotation frequency ($\pi v_F/\lambda$). Levy and Zhang later presented a quantum-mechanical version of this model [171], starting from the same Hamiltonian used to describe the giant magnetoresistance (GMR) in magnetic multilayers. Mistracking leads to mixing of the majority and minority spin channels, changing the spin dependent scattering at impurities within the DW. This increases the resistance of one spin channel while reducing that of the other, thereby giving a higher net resistance of the two parallel channels. Some experimental values of DWR compatible with the theory of Levy and Zhang have been reported [23,209–211], although measurements were often hampered by the presence of other magnetoresistive effects. In contrast, other conflicting theories of DWR predict negative resistance [212] or a contribution that can have either sign [213]. Unusually high DWR values were found in epitaxial Co strips at 77 K [214], which was attributed to the spin flip length being much larger than the width of the DW leading to spin accumulation at the DW, although it was later argued that this is not sufficient to explain their results [215]. Despite this considerable progress during the past years, the width of the DW, which is obviously a crucial parameter in fundamentally unraveling the origin of DWR, could never be changed systematically in experiments on DW resistivity.

In this Chapter we address this outstanding issue, by introducing a unique approach to simultaneously engineer the DW width and measure its intrinsic resistivity. We use Ga irradiation to create a controlled magnetic domain pattern in a Pt/Co/Pt strip [23], and measure the resistance of individually appearing DWs directly by real-time magneto-optic imaging. Interestingly, the perpendicular anisotropy is tuned by the irradiation dose, and thereby the DW width λ can be carefully controlled. It is found that the DWR scales as $1/\lambda^2$, lending strong support to the aforementioned Levy-Zhang theory [171]. Also quantitative agreement is found by taking into account the current flow through the individual layers of the multilayer stack [216], allowing us to estimate the spin asymmetry of the current in the Co layer. We believe that the observed dominant role of mistracking between mobile electron spins and local DW magnetic moments will aid in pinpointing the origin of nonadiabatic spin-transfer-torque in novel DW devices.

8.2 Experimental procedure

The resistance of DWs is measured on 1.5 μm wide Pt (4 nm) / Co (0.5 nm) / Pt (2 nm) strips fabricated by e-beam lithography, sputter deposition and lift-off. We adopt an on-sample Wheatstone bridge configuration [23] with 4 identical Pt/Co/Pt strips as shown in Figure 8.1(a). One of the four strips is then patterned with 30 keV Ga ions using a focused ion beam, to create regions with a reduced magnetic anisotropy and coercivity [23,82], as outlined in Chapter 2. The resistance of this strip changes when DWs are present, leading to a change in the offset voltage $V_A - V_B$.

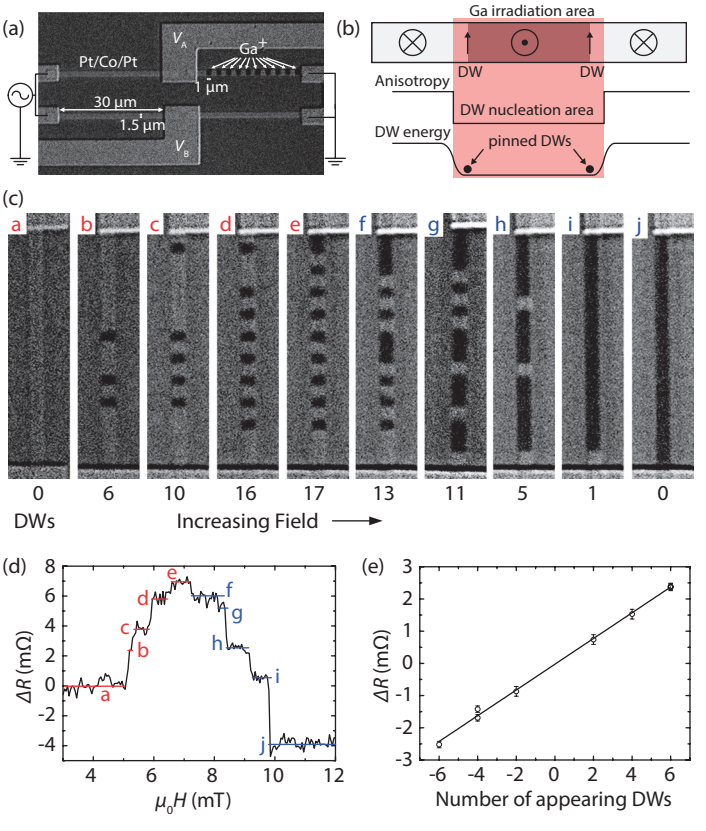

Figure 8.1 | (a) Kerr microscopy image of the experimental geometry showing 4 Pt/Co/Pt strips in a Wheatstone bridge configuration, where one of the strips has been patterned using a focused Ga-ion beam with an irradiation dose of 0.56×10^{13} Ga ions/cm^2. The dark areas have inverted magnetization and correspond to the irradiated areas. (b) Close-up of a Ga irradiated area (top), leading to an anisotropy well along the strip direction (middle), which translates into an energy well for the two DWs that are nucleated in the irradiated area. The DWs will thus remain within the irradiated area where their width can be tuned by the irradiation dose. (c) Kerr images recorded upon increasing the external magnetic field, showing nucleation and annihilation of magnetic domains. (d) Resistance as a function of field. Discrete steps are observed whenever DWs are nucleated or annihilated as visualized in (c). (e) Magnitude of resistance jumps as a function of number of DWs nucleating/annihilating. The slope represents the resistance increase due to a single DW.

An AC current runs in the indicated direction and $V_A - V_B$ is measured using a lock-in amplifier. Knowing the resistance of the four individual strips ($R \sim 1.3\,\mathrm{k\Omega}$), the resistance change in the patterned strip ΔR can be accurately determined.

Starting from negative perpendicular saturation, ΔR is measured as a function of positive applied field (Figure 8.1(d)), while the magnetic configuration is imaged in real-time in a wide-field Kerr microscope (Figure 8.1(c)). As the magnetic field is increased, domains are nucleated in the Ga-irradiated regions and expand to the irradiation boundaries, where DWs get pinned, as sketched in Figure 8.1(b) [24,49,82]. Since there is some spread in the nucleation fields of each irradiated region, not all domains are created at the same time. Each time a new domain appears, a step in the resistance is observed, corresponding to the resistance of the new pair of DWs. When the field is increased further, DWs depin from the irradiation boundaries and annihilate with neighboring DWs, which is accompanied by a stepwise decrease of the resistance.

This technique is very powerful to directly determine the resistance of individual (pairs of) DWs, which was before only attempted indirectly by comparing with MFM images recorded afterwards [23,217]. Furthermore, our measurement scheme allows for exclusion of measurement artifacts caused by other magnetoresistive effects. For example, the AMR contribution to the resistance does not depend on the number of DWs, since the magnetic orientation within the Bloch DWs is always perpendicular to the current flow†. Another measurement artifact is readily observed in Figure 8.1: the final resistance step from (i) to (j) in Figure 8.1(d) appears to originate from the disappearance of a single DW in Figure 8.1(c). However, this resistance change is too large to correspond to a single DW, and instead originates from switching of the magnetic area underneath the bottom contact, probably yielding a contribution from the anomalous Hall effect (AHE). A similar effect is observed in the switching from state (d) to (e), albeit less prominent. Therefore, switching events that include a contact are excluded from the data analysis. In Figure 8.1(e), all observed resistance jumps are plotted as a function of the number of DWs (dis)appearing, showing an expected linear behavior, from which the resistance of an individual DW can be accurately extracted.

8.3 Results & discussion

Combining all resistance steps linked to switching events, we find a positive resistance change $\Delta R = 7 \pm 1\,\mathrm{m\Omega}$ when the maximum number of 20 DWs is present. To quantitatively compare these data with theoretical models we should obviously consider the DW *resistivity* in the magnetic Co layer, excluding current shunting through the Pt layers. The spin-resolved current density in the layer system was therefore computed using a Fuchs-Sondheimer model with parameters from [216], as shown in Figure 8.2. We find a fraction $p \approx 3\%$ of the current flows through the Co layer, much less than the 8% predicted by only considering the bulk resistivities [23] without interface scattering. This fraction is used to compute $R_{Co} = R/p$

† In Chapter 10, we will find that the DWs in this material can have a small m_x-component and accompanying AMR contribution, but it only becomes measurable when in-plane fields are applied.

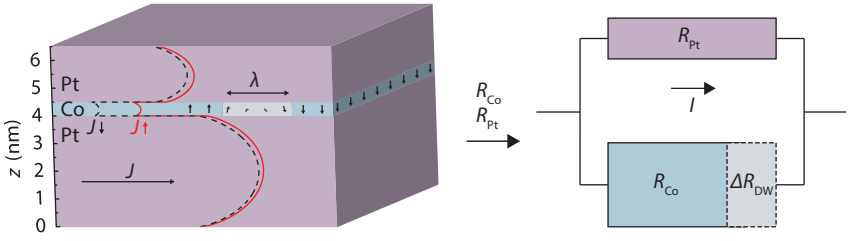

Figure 8.2 | Sketch of the multilayer geometry, including a calculation of the current distribution of majority and minority electrons, using the Fuchs-Sondheimer model. The same material parameters as in [216] were used. 3% of the current flows through the Co layer, which was used to evaluate the resistance of the Pt and Co layers in a parallel resistor model. On the right, the contribution of the Co layer, Pt layers and DW resistance to the total resistance of the strip is sketched.

and $R_{\mathrm{Pt}} = R/(1-p)$, which can then be used to quantify the resistance change of the Co layer ΔR_{DW} due to all DWs present, using the geometry of Figure 8.2,

$$\Delta R_{\mathrm{DW}} = \frac{\Delta R\,(R_{\mathrm{Pt}} + R_{\mathrm{Co}})}{R R_{\mathrm{Pt}} - R_{\mathrm{Co}}\Delta R} R_{\mathrm{Co}}. \tag{8.1}$$

Finally, the desired DW resistivity is then found by multiplying with the layer cross section $w\,t_{\mathrm{Co}}$ and dividing by the total width of the N DWs,

$$\rho_{\mathrm{DW}} = \frac{\Delta R_{\mathrm{DW}}\, w\, t_{\mathrm{Co}}}{N\,\lambda}. \tag{8.2}$$

The DW width λ is estimated by $\pi\sqrt{A/K_{\mathrm{eff}}}$, with $A = 16\,\mathrm{pJ/m}$ [218] the exchange stiffness and K_{eff} the magnetic anisotropy, whose magnitude we will discuss later.

As mentioned, the DW width λ is a crucial parameter in theories on DWR. Therefore, we take a unique approach to tune the DW width by the Ga irradiation dose. It is known that Ga irradiation reduces the perpendicular magnetic anisotropy constant K_{eff} [44,82], and this leads to wider DWs. Furthermore, we know that a Ga irradiation boundary acts as an energy barrier due to the sudden increase of magnetic anisotropy, and a pinned DW resides at the base of the barrier, hence in the irradiated region, as sketched in Figure 8.1(b) [24,49,82]. Thus by varying the irradiation dose, we can vary the width of a pinned DW, of which the resistance is measured as explained before. Figure 8.3 constitutes the main result of this experiment.

In Figure 8.3(a), the raw data of the resistance increase ΔR due to 20 DWs in a Pt/Co/Pt strip is plotted as a function of Ga dose. A decrease is observed, meaning that a lower anisotropy yields a lower DW resistance. In Figure 8.3(b), the anisotropy of Pt (4 nm) / Co (0.5 nm) / Pt (2 nm) as a function of Ga dose is shown and fitted with exponential decay. The anisotropy was measured in section 2.5.2 on irradiated 5 µm wide Hall bars by fitting $M(H)$ according to Stoner-Wohlfarth

theory, with H applied at different angles to the film normal [82]. The result is used in Figure 8.3(c) to convert each used Ga dose to a value of K_{eff} on the x-axis. On the y-axis, the DW resistivity ρ_{DW} (8.2) normalized by the resistivity of the Co layer ρ_0 ($= R_{\text{Co}} \times w \times t_{\text{Co}}/L \approx 1.07\,\mu\Omega\text{m}$) is shown.

As one of the most prominent observations in this Chapter, it is seen that the DW resistivity as a function of anisotropy is not only remarkably linear, but also extrapolates through the origin. This implicitly means that the DW resistivity ρ_{DW} scales with $1/\lambda^2$, which we show in Figure 8.3(d) by deducing the DW width from the anisotropy constants. This, together with the fact that $\rho_{\text{DW}} > 0$ for all DW widths, strongly suggests that the effect should arise from additional scattering due to mixing between the spin channels when electrons are trying to follow the changing magnetization direction within the wall, an effect that according to our data quadratically becomes larger when reducing the width of the wall. As already mentioned in the introduction, this is fully compatible with the spin-mistracking model proposed by Levy and Zhang [171], where

$$\begin{aligned}\frac{\rho_{\text{DW}}}{\rho_0} &= \frac{1}{5}\left(\frac{\pi\hbar^2 k_{\text{F}}}{4m\lambda J}\right)^2 \\ &\quad\times\left(\frac{\rho_\uparrow}{\rho_\downarrow} - 2 + \frac{\rho_\downarrow}{\rho_\uparrow}\right)\left(3 + \frac{10\sqrt{\rho_\uparrow/\rho_\downarrow}}{\rho_\uparrow/\rho_\downarrow + 1}\right),\end{aligned} \tag{8.3}$$

with $\rho_{\uparrow(\downarrow)}$ the resistivity of up (down) electrons, $\hbar$ Planck's constant, k_{F} the Fermi wavevector, m the electron mass, and J the exchange splitting. Using $\lambda = \pi\sqrt{A/K}$[‡], the linear dependence on K_{eff} as observed in Figure 8.3(c) is recovered. Quantitative information can be gained from the slope of the linear fit, which yields a value for the spin asymmetry $\rho_\uparrow/\rho_\downarrow = 7.5$ if the other parameters are kept constant at $k_{\text{F}} = 1\,\text{Å}^{-1}$, $A = 16\,\text{pJ/m}$ and $J = 0.5\,\text{eV}$. We should note that this is the spin asymmetry of the current in the ultrathin Co layer, so a higher value in bulk Co is needed to reproduce this in the Fuchs-Sondheimer model. Still, the value is very reasonable and comparable with previous measurements and thin-film band structure calculations [23].

We strongly believe that the observed effect as a function of Ga dose is dominated by the tuning of the DW width. While Ga irradiation could influence the transport properties, we verified that the change in ordinary resistivity was only 0.5% in the Ga dose range used. Furthermore, preliminary experiments on current-assisted DW depinning from the irradiated area indicate no decrease of spin torque efficiency with increasing dose, hence spin-polarized transport appears to be conserved. Finally, intrinsic magnetoresistance effects such as AMR or anisotropic interface magnetoresistance [220] can be excluded, since the resistance of a DW should in that case increase instead of decrease as a function of λ.

[‡]Note that in obtaining their result, Levy and Zhang [171] used a simplified DW profile with $\theta = \pi x/\lambda$. In such a linearized profile, the width obtained from the more accurate Bloch definition $\lambda = \sqrt{A/K_{\text{eff}}}$ is an underestimation. Hence we used the other common convention containing a prefactor π [219], which has an influence on the fitted value of $\rho_\uparrow/\rho_\downarrow$. In Chapter 10, we took the more complicated approach of integrating the LZ resistance over the Bloch profile, since we needed to take into account the influence of an in-plane field on that profile.

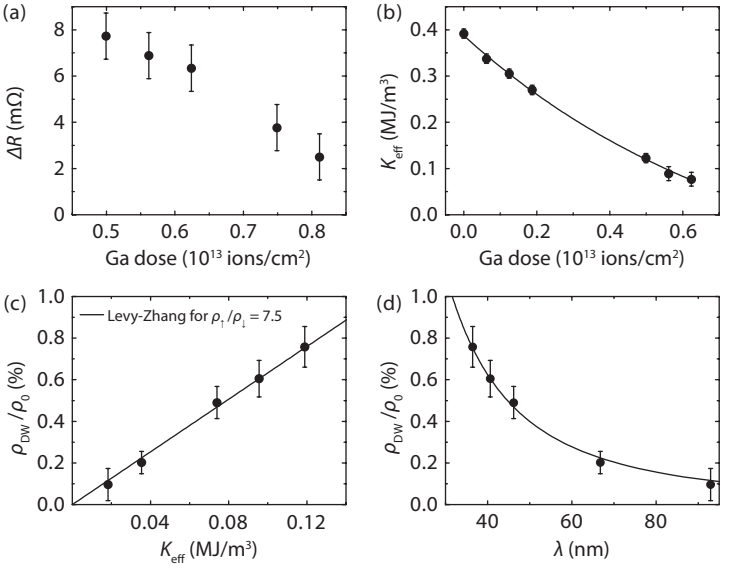

Figure 8.3 | (a) Resistance change ΔR due to 20 DWs in a Pt/Co/Pt strip as a function of Ga dose. (b) Perpendicular anisotropy as a function of Ga dose. The line is an exponential fit. (c) Normalized DW resistivity as a function of anisotropy. The line is the theoretical result of the Levy-Zhang model with $\rho_\uparrow/\rho_\downarrow = 7.5$. The same data is plotted in (d) as a function of DW width, showing the $1/\lambda^2$ dependence.

8.4 Conclusion

In conclusion, our measurement of the DW resistivity in Pt/Co/Pt as a function of magnetic anisotropy by variation of Ga irradiation dose lend strong support to the theory of Levy and Zhang [171]. The $1/\lambda^2$ dependence predicted by the model was, to our knowledge, verified for the first time, and quantitative agreement is found with a value for the spin asymmetry $\rho_\uparrow/\rho_\downarrow = 7.5$. Besides its fundamental importance, this could have interesting implications for current-induced DW motion, in particular the nonadiabatic spin-transfer torque (STT) contribution characterized by the β parameter [9,166,168], in which both the width and the resistivity of the DW are important parameters. Our result implies that mistracking of the spin of conduction electrons with the local magnetization increases significantly in smaller DWs. Recent experiments have revealed that β is relatively insensitive to the DW width down to 1 nm [40]. This calls for further systematic studies of β and the DW resistivity down to sub-nm DW widths, as a shift between the spin relaxation [9], spin mistracking [168] and momentum transfer [166] mechanisms could become apparent.

Domain-wall depinning governed by the spin Hall effect

9

Perpendicularly magnetized materials have attracted significant interest due to their high anisotropy, which gives rise to extremely narrow, nano-sized DWs. As a result, the recently studied current-induced DW motion (CIDWM) in these materials promises to enable a novel class of data, memory, and logic devices [20,70,221–223]. Here we propose the spin Hall effect as an alternative mechanism for CIDWM. We are able to carefully tune the net spin Hall current in depinning experiments on Pt/Co/Pt nanostrips, offering unique control over CIDWM. Furthermore, we determine that the depinning efficiency is intimately related to the internal structure of the DW, which we control by the application of small fields along the nanostrip. This novel manifestation of CIDWM offers an attractive degree of freedom for manipulating DW motion by charge currents, and sheds light on the existence of contradicting reports on CIDWM in perpendicularly magnetized materials [26,29,30,224–226]. *

9.1 Introduction

CIDWM is often explained in terms of the adiabatic and nonadiabatic torques [4,9,10,14], which both depend on the in-plane spin current that arises from the spin-polarization of the charge current that runs in the ferromagnet. However, in the typical multilayer structures used for DW motion in perpendicular materials, a second spin current, generated by the spin Hall effect (SHE) in the adjacent non-magnetic metal layers [179,180,227], can be injected into the ferromagnet. Materials exhibiting a large SHE are often used for these non-magnetic metal layers, because both the perpendicular anisotropy and the SHE depend strongly on spin-orbit coupling. In such multilayered thin-films, the SHE is particularly efficient in affecting the magnetization because of its large injection interface (the in-plane cross section of the strip). In these structures, spin Hall currents have indeed been shown to change the effective damping [228], induce ferromagnetic resonance [191], inject

*Published as: *DW depinning governed by the spin Hall effect*. P. P. J. Haazen, E. Murè, J. H. Franken, R. Lavrijsen, H. J. M. Swagten, and B. Koopmans, Nature Materials **12**, 299 (2013).

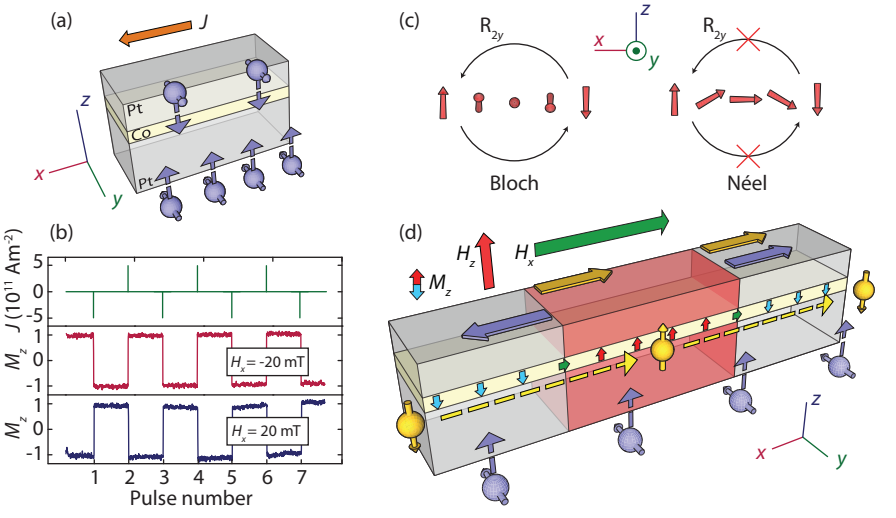

Figure 9.1 | Magnetization dynamics induced by the Spin Hall effect. (a) A vertical spin current is generated in both Pt layers as a consequence of the charge current density J via the SHE and injected in the Co. The thickest Pt layer induces a higher spin current, leading to a nonzero net injected spin current. (b) Perpendicular switching of a uniformly magnetized Pt (2 nm) / Co (0.5 nm) / Pt (4 nm) nanostrip confirms the torque from the spin Hall current, where the combination of the charge current direction and the in-plane field H_x set the stable perpendicular magnetization direction. (c) Bloch and Néel DW types. The Bloch wall is symmetric under a 180° rotation along the y-axis (R_{2y}), which prohibits motion of the DW when subjected to a Slonczewski-like torque. (d) Contributions to the CIDWM (arrows on top of structure) from conventional torques (yellow) and the spin Hall effect (violet). For simplicity, only the dominating spin current from the bottom Pt layer is visualized. Under the application of an applied magnetic field in the x-direction (H_x), the Néel wall can be stabilized, with its center spin pointing along the field.

and detect spin waves [229], and switch the magnetization of in-plane magnetized β-Ta/CoFeB [85] and out-of-plane magnetized Pt/Co/AlOx [31,84] nanodots. Furthermore, it was suggested that CIDWM in in-plane materials could be influenced [230]. These considerations suggest that the SHE plays an important role in the intensively studied CIDWM in perpendicular materials. In this Chapter, we explore the potential of CIDWM by the SHE, showing that it in fact constitutes the main contribution to DW motion in Pt/Co/Pt.

9.2 The spin Hall effect in Pt/Co/Pt

To study the effect of the spin Hall current on DW motion, we have used Pt/Co/Pt structures. Both Pt layers in this stack act as a spin Hall current source, which inject oppositely oriented spins into the ferromagnetic Co layer (see Figure 9.1(a)). Therefore, to inject a net spin current in the Co, the spin Hall currents from the

two Pt layers should not cancel fully. This is achieved by choosing unequal Pt layer thicknesses in the range of the spin diffusion length λ_{sf} of Pt, since the spin Hall current is dependent on the layer thickness, as was experimentally verified before[191]. Consider for example the top Pt layer: spin accumulation occurs at the top of the stack, which by spin-diffusion can flow down to the Co/Pt interface where the spins compensate the directly injected spin Hall current because their polarization is opposite. In a drift-diffusion model[185], this gives rise to a reduction factor $1 - \mathrm{sech}(t_{Pt}/\lambda_{sf})$ for a single Pt layer. Hence, subtracting the contributions from the bottom and top Pt layers having thicknesses t_b and t_t, the net spin Hall current is reduced from the bulk value by a factor ν,

$$\nu = \mathrm{sech}\left(\frac{t_t}{\lambda_{sf}}\right) - \mathrm{sech}\left(\frac{t_b}{\lambda_{sf}}\right). \tag{9.1}$$

For studying pure SHE-induced dynamics, Pt/Co/Pt stacks have the advantage that Rashba effects are negligible. In the closely related Pt/Co/AlOx, in which SHE-induced magnetization reversal has been shown recently[31,84] (see section 7.2.5), it was suggested that a nonadiabatic contribution of the Rashba field[176] could be important. In Pt/Co/Pt, there are two approximately equal (Pt/Co) interfaces, resulting in a Rashba field that is negligible (see Appendix B.4 for experimental backup). Pt/Co/Pt therefore functions as an excellent model system to unambiguously study the hitherto unexplored role of the SHE in DW dynamics.

First, we have verified that the SHE can indeed inject a net spin current, capable of inducing a significant torque on the magnetization, in an asymmetric Pt (4 nm) / Co (0.5 nm) / Pt (2 nm) nanostrip. For these unequal Pt layer thicknesses, the net spin Hall current should be approximately 35% of the bulk value based on (9.1). As confirmation of the existence of a net SHE, we have performed pure current-induced switching of a uniformly magnetized nanostrip, analogous to experiments performed on Pt/Co/AlOx[31,84]. Current pulses of 30 ns and 5×10^{11} A/m^2 were injected into a nanostrip subjected to an applied field, $\mu_0 H_x = 20$ mT, parallel to the charge current. Indeed, the current pulses result in magnetization reversal of the nanostrip, as is shown in Figure 9.1(b), where the stable direction of the magnetization is determined by the sign of both the in-plane field and the current, and equal to that observed in Pt/Co/AlOx[31,84]. This confirms that the thickest Pt layer indeed leads to a larger spin Hall current, resulting in a torque that is not fully compensated by the torque from the spin current from the thinner top layer.

9.3 Spin Hall torque on domain walls

We will now consider the effects of this net spin Hall current on a magnetic DW in a nanostrip. When injected into a ferromagnetic layer, the spin Hall current gives rise to a torque on the magnetization of the Slonczewski-form[6]. This contribution is added to the LLG equation, which describes the time evolution of the magnetization $\mathbf{m}$:

$$\frac{\partial \mathbf{m}(t)}{\partial t} = -\gamma\mu_0 \mathbf{m} \times \mathbf{H}_{\mathrm{eff}} + \alpha \mathbf{m} \times \frac{\partial \mathbf{m}(t)}{\partial t} - (\mathbf{u}\cdot\nabla)\mathbf{m} + \beta \mathbf{m} \times (\mathbf{u}\cdot\nabla)\mathbf{m} - \tau_{\mathrm{SL}}^{\mathrm{SHE}} (\mathbf{m} \times \hat{\mathbf{y}} \times \mathbf{m}), \tag{9.2}$$

with α the Gilbert damping parameter, γ the gyromagnetic ratio, $\mathbf{u}$ a measure of the current density as defined in (7.2). The terms on the right hand side denote, in order, precession along an effective field $\mathbf{H}_{\text{eff}}$, the Gilbert damping, the conventional adiabatic and nonadiabatic terms, and finally the new Slonczewski-like (SL) torque induced by the SHE, with $\tau_{\text{SL}}^{\text{SHE}}$ denoting its magnitude.

To analyze the effect of the Slonczewksi torque, it is important to consider the internal structure of the DW. Since the width of the Pt/Co/Pt nanostrips is much larger than the typical DW width, the DWs are expected to be of the Bloch type (see Figure 9.1(c)). For this wall type, the Slonczewksi torque cannot lead to DW motion because of symmetry considerations: the 180° rotational symmetry around y-axis (R_{2y}) of this wall type prohibits a well-defined direction of movement, since a hypothetical direction of motion would reverse under this symmetry operation while the system and the resulting SL torque remain unchanged. However, the Bloch wall can easily be perturbed, so that this symmetry is broken. In this research, to tune the internal structure of the DW, a field in the x-direction (along the nanostrip) is applied. This applied field changes the DW from the initial Bloch type to a Néel type (see Figure 9.1(c)) with the center spin aligned to the field.

When the DW is of the Néel type, the spins obtain an x-component, thereby breaking the R_{2y} symmetry, which is crucial for the movement of the wall. This dependence on the x-component is analogous to the required tilt of the magnetization in the switching that was shown in Figure 9.1(b), where a specific combination of an in-plane field and spin Hall current direction results in a single stable perpendicular magnetization direction. A domain with this magnetization direction is expected to expand under influence of the SHE (Figure 9.1(d), blue arrows), which we verified by micromagnetic simulations, based on (9.2) (see Appendix B.3). The conventional adiabatic and nonadiabatic terms also give rise to torques on the DWs, and are expected to push the domain in the electron drift direction, independent of the polarity of the domain [10] (Figure 9.1(d), yellow arrows). Hence, one DW will be driven by a combination of conventional torques and the SHE because they work in parallel for that wall, whereas these two contributions counteract one another in the other DW, thereby providing an excellent tool to disentangle these contributions to the CIDWM.

9.4 Experimental demonstration

This scheme to uniquely identify the role of the SHE is now applied to a Pt (4 nm) / Co (0.5 nm) / Pt (2 nm) nanostrip, in which a well-defined region with reduced anisotropy is engineered using Ga ion irradiation [49]. In this magnetically softer region, a domain can be stabilized, as can be seen in Figure 9.2(a) (left pane). Since the energy of a DW scales with the root of the anisotropy, the DWs stay pinned at the anisotropy steps. When the perpendicular H_z field is increased, a critical field H_{pin} will depin the DWs over the energy barriers, after which they propagate towards the ends of the nanostrip.

We will now concentrate on the dependence of H_{pin} on an in-plane current for both DWs where we set the Néel structure by applying an in-plane field $\mu_0 H_x = -15\,\text{mT}$. As can be seen in Figure 9.2(b), already at reasonably low current density J (i.e. $\sim 10^{10}\,\text{A/m}^2$), H_{pin} can be significantly altered, and an almost

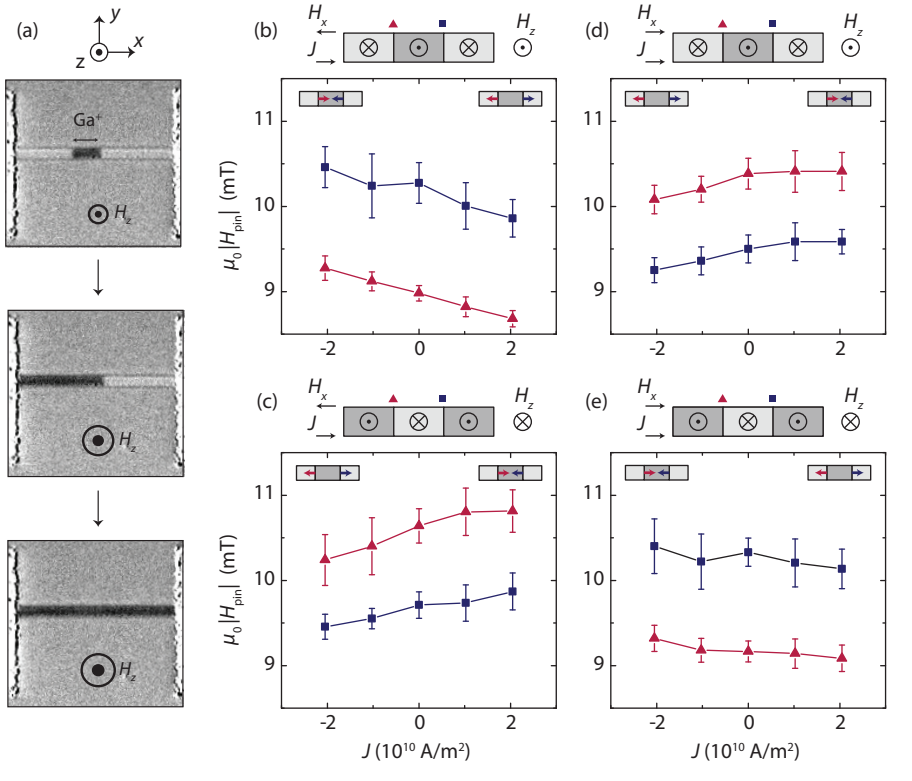

Figure 9.2 | DW depinning experiment. (a) Kerr images of the subsequent nucleation of a domain in the low-anisotropy region and the depinning events of the two walls of the domain. (b-e) Pinning fields for the right (blue squares) and left (red triangles) DWs versus in-plane current in Pt (4 nm) / Co (0.5 nm) / Pt (2 nm). Data points are averaged values of 20 depinning events, with the standard deviation given by the error bars. Measurements were performed with in-plane fields of $\mu_0 H_x = -15$ mT (b,c) and $\mu_0 H_x = 15$ mT (d,e). The sign of the contribution of the current to the DW depinning changes under reversal of DW polarity (see b vs c and d vs e) and in-plane field (b vs d and c vs e). The cartoons on top of the graphs shows the labels of the two DWs as a legend, and the cartoons in the graphs show the direction of the current induced contribution to the depinning process for negative (left side) and positive (right side) currents.

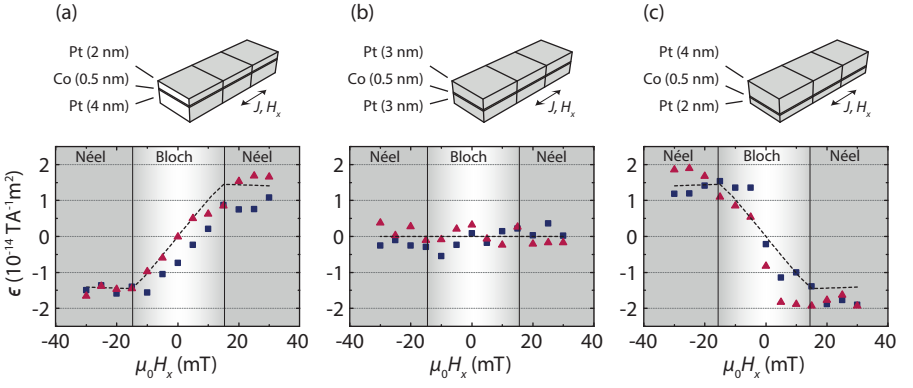

Figure 9.3 | Depinning efficiency as a function of H_x field, for Pt (t_b nm)/Co (0.5 nm)/Pt (t_t nm). (a) $(t_b, t_t) = (4, 2)$; (b) $(t_b, t_t) = (3, 3)$; (c) $(t_b, t_t) = (2, 4)$. The magnetization of the expanding domain is parallel to $+z$. The cartoons on top of the graphs indicate the stack sequence. The dashed black lines are the results of the micromagnetic simulations, performed without adjustable parameters (see Appendix B.3), and the symbols indicate ϵ for the two DWs, with the color coding analogous to Figure 9.2. The internal structure of the DW, as determined by micromagnetic simulations, is indicated by the background color of the graph. At fields higher than $\mu_0 H_x = 15$ mT, the structure is of the Néel type, and at $\mu_0|H_x| < 15$ mT, the DW structure gradually changes from the Néel type to the Bloch type (at $\mu_0 H_x = 0$ mT) to the opposite Néel type.

linear dependence on the current is measured. However, the observed symmetry is radically different from that expected of the conventional torques. When the center domain is magnetized in the upward direction and a negative H_x is applied (Figure 9.2(b)), a positive current results in a lower H_{pin} for both DWs, and is therefore *assisting* the depinning of both DWs similar to a H_z-field, even though their depinning directions are opposite. Furthermore, when the polarity of the DW is reversed (Figure 9.2(c)), the current is now *opposing* the DW depinning for both DWs. When the in-plane field is reversed, the slopes of H_{pin} versus J again change sign, as can be seen in Figure 9.2(d) and Figure 9.2(e). Such behavior cannot be explained in the paradigm of conventional torques, which predicts an opposite sign of the slopes for the two DWs, and none of the observed sign changes. Moreover, we find no systematic difference in the slopes for the two DWs, indicating that the conventional torques are negligible. Instead, we have demonstrated a new mechanism for DW motion, governed by the spin Hall effect. Note that the offsets in Figure 9.2(b-e) also depend on the in-plane field in a non-trivial way. This is probably caused by details of the local energy landscape of the depinning center, thereby forming a separate effect that is not relevant for the SHE-induced behavior of $\mathrm{d}H_{\text{pin}}/\mathrm{d}J$ (Appendix B.2 presents a systematic measurement).

9.5 Role of stack composition

To further proof that the spin Hall effect is of dominant importance for the DW depinning, we will now discuss the role of the stack composition. The subtractive nature of the two competing spin currents from the Pt layers predicts that engineering of the strength and sign of CIDWM by tuning the Pt thicknesses is possible via (9.1). Therefore, we have repeated these measurements on Pt (t_b nm) /Co (0.5 nm)/Pt (t_t nm) nanostrips with $(t_b, t_t) = (4,2); (3,3); (2,4)$. Indeed, the sign of the depinning efficiency, $\epsilon = \mu_0 \mathrm{d}H_{pin}/\mathrm{d}J$, clearly reverses between the (4,2) and (2,4) stacks, as can be seen in Figure 9.3. Furthermore, for the (3,3) stack, the two spin currents cancel, resulting in a zero net spin current and no systematic influence on the DW depinning.

Up until now, we discussed measurements at a fixed $|H_x| = 15\,\mathrm{mT}$, but the functional dependence of ϵ on H_x also shows an interesting behavior (Figure 9.3(a)). Starting from 0, after a linear increase, at $\mu_0 H_x > 15\,\mathrm{mT}$ ϵ saturates for both the (4,2) and (2,4) stacks. Micromagnetic simulations using only the SHE-induced SL torque also reproduce this saturation, without using any free parameters (see Appendix B.3), as can be seen in Figure 9.3 (dashed lines). They reveal that the internal structure of the DW is indeed of crucial importance for ϵ. At $H_x = 0$, the DW is of the Bloch type, and the depinning efficiency is zero. When an H_x is applied, the internal angle of the DW starts to align with this field, and ϵ increases. At $\mu_0|H_x| \approx 15\,\mathrm{mT}$, the DW is fully aligned with H_x (i.e. in a full Néel configuration, see Appendix B.3), and ϵ saturates. These results show that it is possible to tune the efficiency and the direction of the CIDWM by controlling the magnitude of the net spin Hall current and the internal DW structure.

9.6 Conclusion & outlook

To conclude, we have demonstrated a mechanism of DW motion by the SHE, in which the direction of motion depends on the polarization of the spin Hall current, the x-component of the magnetization within the DW, and the polarity of the DWs. Note that the latter two observations together actually imply that the *chirality* of the DW defines the direction of motion. The findings presented in this Chapter have important implications for the research field, where the spread in sign and magnitude in reported values of ϵ is an urgent issue [26,29,30,224–226]. Because of the abundant use of materials with high spin-orbit coupling in perpendicularly magnetized DW conduits, it is very likely that the SHE also plays a role in other CIDWM experiments. Even without the use of an in-plane field, deviations from a pure Bloch structure can be induced by other factors, such as field misalignments or contributions from the adiabatic and nonadiabatic torques, from the shape anisotropy in narrow strips, or from the Dzyaloshinskii-Moriya interaction as discussed in the next Chapter. Hence, it is likely that in previous research the SHE has influenced the CIDWM, and these contributions could have been erroneously ascribed to the nonadiabatic torque. We therefore belief that the SHE plays a decisive role in explaining, at least partially, the existence of contradicting reports on CIDWM in perpendicular materials.

Finally, for DW-based applications, the demonstration of the SHE driven DW motion offers a completely new degree of freedom for controlling DW motion by

a charge current. We have shown that when the DW structure and chirality are controlled, reliable SHE-driven DW motion can be achieved. Furthermore, its favorable scaling behavior makes the SHE-driven DW motion especially promising, since it opens up possibilities for efficient and dense data storage devices.

9.7 Methods

The dimensions of the Pt/Co/Pt nanostrips are $1.5\,\mu m \times 20\,\mu m \times 6.5$ nm. Pt and Co were deposited on thermally oxidized SiO_2 substrates by DC magnetron sputtering in a system with a base pressure of $\sim 3 \times 10^{-8}$ mbar. From these thin films, nanostrips were fabricated using e-beam lithography and lift-off. The electrodes were made of 35 nm thick Pt and were also deposited by sputter deposition. The out-of-plane component of the magnetization (M_z) of the nanostrips was measured by polar Kerr microscopy. The external magnetic field was applied in 3 orthogonal directions. The H_x field was applied before nucleation, and kept constant until completion of the measurement routine. No contributions from Joule heating, which would have resulted in a deviation from the linear behavior of H_{pin} versus J, can be observed in the depinning experiments, because low current densities ($< 2.5 \times 10^{10}\,A/m^2$) were used.

In Appendix B, more supplementary information is provided as referred to at several points within the text.

Tunable chiral spin texture in magnetic domain walls

10

Magnetic DWs with a preferred chirality exhibit very efficient current-driven motion [204–206]. Since structural inversion asymmetry (SIA) is required for their stability, the observation [231] of chiral DWs in highly symmetric Pt/Co/Pt is intriguing. Here, we tune the layer asymmetry in this system and observe, by current-assisted DW depinning experiments, a small chiral field which sensitively changes. Moreover, we convincingly link the observed efficiency of DW motion to the DW texture, using DW resistance as a direct probe for the internal orientation of the DW under the influence of in-plane fields. The very delicate effect of capping layer thickness on the chiral field allows for its accurate control, which is important in designing novel materials for optimal spin-orbit-torque-driven DW motion. *

10.1 Introduction

Current-induced motion of magnetic DWs in materials with perpendicular magnetic anisotropy (PMA) could be used to transport data in next-generation storage devices [7]. Recently, it has been suggested that in addition to conventional bulk STT contributions [10], various current-induced torques relating to the high spin-orbit coupling in these materials could play a dominant role [84,85,232]. Most notably, the sources of these so-called spin-orbit torques include the Rashba field, which enters as a current-dependent transverse H_y field [30,176,192], and the spin Hall effect (SHE) [180], which leads to a vertical spin current with transverse polarization σ_y. In the previous Chapter [233], we demonstrated that the SHE has the correct characteristics to describe the effect of current on DWs in Pt/Co/Pt. It was observed that the efficiency of current-induced DW motion is practically zero, since the Bloch wall that is expected to be stable does not have the correct symmetry to be moved by the SHE (Figure 10.1(a)) [193,233]. Efficient motion arose when the internal structure was forced to the Néel type by applying a field along the current direction. However,

*Under review at Nature Communications as: *Tunable chiral spin texture in magnetic domain-walls*. J. H. Franken, M. Herps, H. J. M. Swagten, B. Koopmans.

this still contradicts the coherent motion, at zero in-plane field, that was observed in other materials where the magnetic layer was sandwiched between two different materials [26,30,234]. After publication of the previous Chapter, several authors recognized [204–206,235,236] that in the case of structural inversion asymmetry (SIA), the Dzyaloshinskii-Moriya interaction (DMI) [198] gives rise to *chiral* spin structures, in this case chiral Néel walls [201,237], which are moved coherently by the SHE-induced effective field (H_{SHE} in Figure 10.1(b)) that we identified in the previous Chapter.

In this Chapter, we demonstrate by current-assisted depinning measurements that a measurable DMI is also present in Pt/Co/Pt [231], which is surprising at first since the top and bottom interfaces are in principle the same. The DMI effect is found to be highly tunable by varying the top layer thickness, and becomes very large when the top Pt layer is substituted by AlOx. In fact, the tuning is so delicate that the DW can have any in-plane angle ϕ in between the Bloch ($\phi = \frac{\pi}{2}$) and Néel ($\phi = 0$) states at remanence, due to the competition between the effective longitudinal DMI field H_D and transverse DW anisotropy field H_K, as visualized in Figure 10.1(c). Our data can be explained by a very simple model [204] of the internal DW angle ϕ under influence of H_D, H_K, and externally applied in-plane fields H_x and H_y (Figure 10.1(d)). The efficiency of DW depinning is simply proportional to $\cos\phi$, as expected from a Slonczewski-like torque by the SHE [204]. To prove that the DW angle ϕ is responsible for the efficiency, we measure the DW resistance as a function of in-plane fields (Figure 10.1(e)) and observe that the DW structure is indeed changing from Bloch to Néel, which is often just assumed based on elementary micromagnetics without any convincing experimental proof. These measurements allow us to directly correlate a high DW efficiency to the presence of Néel walls, which we show to be stabilized by the DMI in a tunable way.

10.2 Effect of chiral field on DW depinning

To allow for DW resistance as well as DW depinning measurements, 1.5 µm wide strips with varying layer configurations were fabricated. Irradiation with Ga ions is employed to locally reduce the PMA in these strips, allowing us to introduce a well-defined number of DWs into the strip [49,238]. The Kerr microscopy image in Figure 10.1(e) visualizes the controlled domain structure that is essential for the DW resistance measurements presented later. When the perpendicular field strength is increased from this state, DWs are randomly depinning from the edges of the irradiated regions, as seen in Figure 10.1(f). We analyze the effect of current on the depinning of two particular DWs, indicated by the red circle and blue square in Figure 10.1(f). The graph shows how the pinning field of these DWs change with increasing current density in a Pt(4)/Co(0.4)/Pt(2) sample (all thicknesses in nm). The slopes define the depinning efficiency $\epsilon = \mu_0 \frac{\mathrm{d}H_{\mathrm{SHE}}}{\mathrm{d}J}$ of each DW. The opposing slopes of the 2 DWs actually imply a coherent action of the current on the DWs: since the field pushes both DWs outwards (incoherently), the current reduces the pinning field of DW2 (negative efficiency) and increases the pinning field of DW1 (positive efficiency). It is worth noting that the sign of current-induced DW motion opposes the electron flow direction and is therefore unlikely to be caused by conventional STT. Instead, we propose that the DWs have a certain degree of

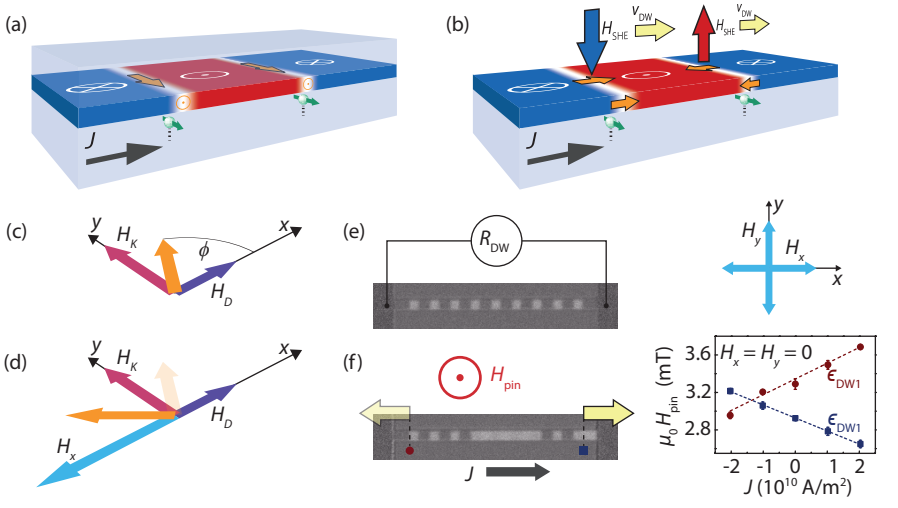

Figure 10.1 | Tuning the chirality of magnetic DWs. (a) In a symmetric layer system, Bloch walls are favored (orange arrows), on which the spin Hall current (green spins) cannot exert a torque. (b) If SIA is introduced, chiral Néel walls with alternating orientation become stable, which are moved coherently (yellow arrows) by the effective spin Hall field $H_{\mathrm{SHE}} \propto \cos\phi$. (c) The in-plane DW angle ϕ (orange) is determined by the competition of the DMI field H_D (violet) and the DW anisotropy field H_K (pink). (d) The internal angle can be further tuned using an external magnetic field H_x (light blue) or H_y (not shown). (e) DW resistance measurements can be used to verify the DW angle ϕ under influence of H_x and H_y. This can be linked to DW motion measurements on the same samples (f), where the pinning field H_{pin} as a function of current density J is measured for the two outermost DWs. The slope of this relation defines the depinning efficiency ϵ of each DW, which scales with $\cos\phi$.

built-in chirality, which leads to their coherent motion driven by the SHE. To prove this, we will use in-plane fields to either oppose or assist the built-in chiral field H_D.

Figure 10.2 shows the measured current-induced depinning efficiency $\epsilon(H_x)$ (top panes) and $\epsilon(H_y)$ (bottom panes) on three samples with different compositions. We first discuss Figure 10.2(a-b), representing the sample with the lowest degree of inversion asymmetry, Pt(4)/Co(0.4)/Pt(2). The H_x and H_y data have been fitted simultaneously using the efficiency expected from the 1D-model with only the SHE as driving force [204], †

$$\epsilon = \mu_0 \frac{\mathrm{d}H_{\mathrm{SHE}}}{\mathrm{d}J} = \frac{\pi\hbar\nu\,\theta_{\mathrm{SH}}}{4eM_s t}\cos\phi =: \epsilon_{\mathrm{SHE}}\cos\phi, \tag{10.1}$$

† In the previous chapter, we used computationally expensive micromagnetic simulations, but the SHE torque on DWs can actually be implemented in the simple 1D model [10], where the only additional input required is the DW anisotropy H_K (which is automatically taken into account in the full simulations).

with θ_{SH} the spin Hall angle, M_s the saturation magnetization, t the magnetic layer thickness, ν a loss factor due to compensating spin Hall currents from the bottom and top Pt layers [233], and ϕ the internal DW angle prescribed by energy minimization of

$$E_{\mathrm{DW}} = \lambda\mu_0 M_s \left(H_K \cos^2\phi - 2\left(H_D + \frac{\pi}{2} H_x \right) \cos\phi - \pi H_y \sin\phi \right). \tag{10.2}$$

Here, λ is the DW width (assumed constant), H_K the shape anisotropy field of the DW, and $H_D = \pi D/(2\mu_0 M_s \lambda)$ the effective chiral magnetic field (with D an energy constant characterizing the strength of the DMI). The free parameters of the fit are H_K, H_D, and ϵ_{SHE} as indicated in Figure 10.2(a). This graph clearly shows that there is a contribution from DMI: the red and blue curves have been shifted to the left and right, respectively, due to the effective chiral magnetic field $H_D \approx 12.5 \pm 0.4$ mT, which has opposite sign for DWs of opposite polarity (up-down vs down-up)[‡]. Apart from the horizontal shift, there is a linear increase from $\epsilon = 0$ to ϵ_{SHE} over a field range $\pi H_K/2$, which is attributed to the transition from Bloch to Néel. Replacing H_x by H_y in Figure 10.2(b), the efficiency simply decreases with $|H_y|$, because H_y gradually pulls the wall to a Bloch state. Interestingly, the DW at zero in-plane field is neither a Bloch nor a Néel wall. From the efficiency at zero in-plane field, it can be deduced that the DW angle at remanence is $\phi \approx 60°$, rather than the 90° that is expected in a system without SIA. To our knowledge, the stability of this in-between wall type in PMA materials has not been reported before and might be interesting for specific applications.

To explore the tunability of the small DMI in Pt/Co/Pt, samples with a thinner 1 nm Pt capping layer were fabricated, in order to increase the apparent SIA. Indeed, in Figure 10.2(c) it is observed that H_D has increased significantly to the value 37 ± 1 mT. The change of efficiency at saturation ϵ_{SHE} matches with the change in layer thickness as discussed in Appendix C.1.1. The SIA can be increased much more by replacing the top Pt layer by a different material, AlOx, as shown in Figure 10.2(e-f). In fact, H_D has become so large that we cannot quantify it within our setup. Regardless of the in-plane field, the DWs are chiral Néel walls which are pushed coherently in the direction of current flow, hence opposite to conventional STT. A small linear effect of the in-plane field on the efficiencies appears to be present, which is either an experimental artifact or caused by mechanisms beyond our simplified 1D model, and could not be explained by incorporating the Rashba effect into our model. Crucially, these results suggest that our Pt/Co/AlOx is not fundamentally different from Pt/Co/Pt, but only has a higher built-in chiral field due to the increased asymmetry.

10.3 Probing the DW structure by DW resistance

Although the results presented so far here and by other authors [204–206,235,236] match well with a SHE-induced torque dictated by the DW angle ϕ, it is not at all trivial that the DW indeed has the structure that these experiments suggest. In fact, the

[‡]In retrospect, we might also identify a small such shift in Figure 9.3(a) of the previous Chapter, which had similar Pt thicknesses but was measured with a higher noise level.

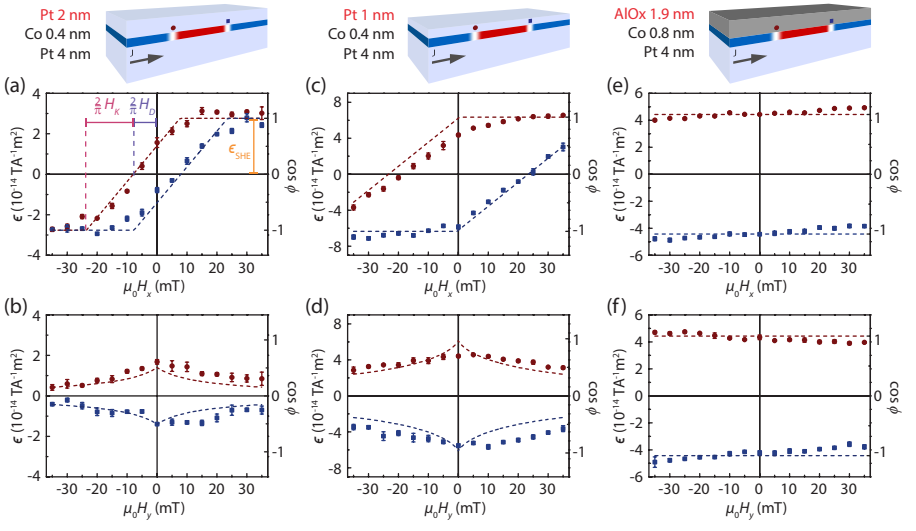

Figure 10.2 | Depinning efficiency ϵ under in-plane fields in systems with varying SIA. (a) in almost symmetric Pt(4)/Co(0.4)/Pt(2), $\epsilon(H_x)$ shows a small opening between the two DWs (red discs and blue squares) of opposite polarity, indicative of a DMI field H_D. The slope of the transition from $\epsilon = 0$ to its saturation level ϵ_{SHE} is characterized by the DW anisotropy H_K. To determine these parameters, a global fit (dashed lines) is performed together with the H_y-data in (b). (c,d) Increasing the stack asymmetry by reducing the top Pt layer to 1 nm gives a higher DMI opening. (e,f) Replacing the top Pt layer by AlOx, the DMI opening becomes too large to measure in our setup. The DMI is so strong that the DW angle ϕ is hardly influenced by H_x and H_y.

transition from a Bloch-like to a Néel state by an in-plane field was to our knowledge not measured before. We believe that using DW resistance as a probe for the DW structure is much more direct than using the DW mobility, since the resistance does not rely on any of the spin torques. Therefore, we have performed measurements of the DW resistance as a function of in-plane field. When the resistance of a Bloch wall is measured (Figure 10.3(a)), the dominant contribution comes from the intrinsic resistance $R_{\mathrm{LZ}} \sim 1/\lambda$[§] dictated by the Levy-Zhang model [171] for which we recently found experimental evidence [23,238] (see Chapter 8). However, when the magnetization within the DW obtains a component parallel to the current flow (Figure 10.3(b)), an additional contribution R_{AMR} from anisotropic magnetoresistance arises [207], simply proportional to $\lambda \cos^2 \phi$. Looking at the measured DW resistance in Pt(4)/Co(0.5)/Pt(2) as a function of H_x (open orange diamonds in Figure 10.3(c)), we indeed see an increase when the in-plane field increases, owing to the transformation to a Néel wall. However, beyond $H_x = 30$ mT, the measured DW resistance starts to decrease again. This decrease is seen over the entire

[§]Note that here, it is convenient to speak in terms of the DW *resistance*, which scales as $1/\lambda$, whereas in Chapter 8 we mostly discussed the DW *resistivity* $\propto 1/\lambda^2$.

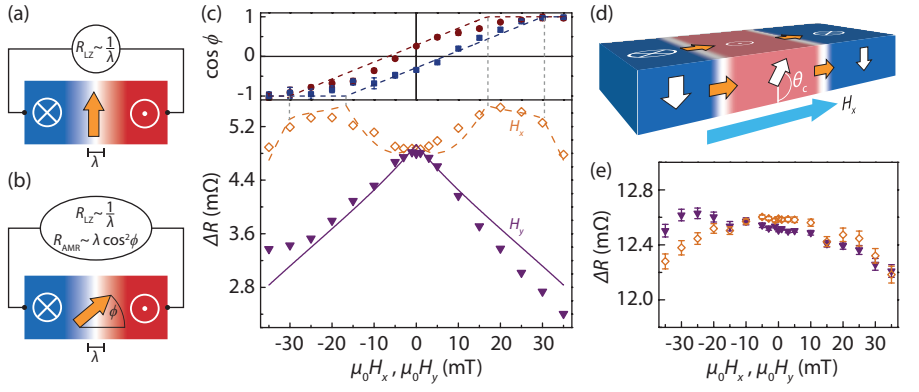

Figure 10.3 | Bloch-Néel transition revealed by DW resistance measurements. (a) A Bloch wall yields only an intrinsic contribution R_{LZ} to the DW resistance. (b) As ϕ approaches 0 (Néel wall), an additional contribution from the AMR effect arises. (c) (top) Depinning efficiency as a function of H_x, and (bottom) Resistance change induced by 20 DWs of alternating polarity, as a function of H_x (open diamonds) and H_y (filled triangles), measured on the same Pt(4)/Co(0.5)/Pt(2) sample. The dashed orange and solid purple line are a fit including the two resistance contributions, in which H_K and H_D have been taken from the fit of the depinning data. The DW resistance peaks around $H_x = 20\,\text{mT}$ due to the transition from Bloch to Néel. A decreasing background signal is present in both the H_y and the H_x data due to canting of the magnetization in the irradiated domain (d), leading to a lower intrinsic contribution R_{LZ}. (e) DW resistance in Pt/Co/AlOx does not show the Bloch-Néel transition since Néel walls are highly stable.

H_y-field range (purple triangles), which can be regarded as a kind of background measurement. We attribute this to a change of R_{LZ} related to the domain structure. Since the anisotropy in one of the domains is reduced strongly by the Ga irradiation treatment [82], this region tends to be pulled in plane, modifying the DW profile as sketched in (Figure 10.3(d)). This has a strong effect on R_{LZ}, and also a small effect on R_{AMR} (see Appendix C.2 for details of the model). From the DW-depinning data (top pane of Figure 10.3(c)), we can deduce $\phi(H_x, H_y)$, and use this as input in our resistance model. The best-fit to this model is presented as the dashed orange and solid purple lines in Figure 10.3(c)), where the free parameters are the anisotropy in the irradiated domain, the AMR resistivity, and the strength of the intrinsic DWR. The model reproduces the measurements, apart from two kinks at each field polarity (when the angles of either the 'red' or the 'blue' DWs saturate, compare to top panel). It is not surprising that these sharp features from the 1D model become smooth in reality, especially since we measure the sum of 20 DWs, each with slightly different local properties.

Looking at the DW resistance measurements in Pt/Co/AlOx in Figure 10.3(e)), only minor changes as a function of in-plane field are observed, and there is no clear difference between the H_x and H_y data. Similar to the DW-depinning results, this suggests a highly stable Néel state which is hardly influenced by the in-plane

fields. The background due to magnetization canting is largely absent here, because the anisotropy in the irradiated domain is much higher. Although any change as a function of in-plane field is relatively small compared to the Pt(4)/Co(0.5)/Pt(2) sample, a small asymmetry appears in the H_y data, which may have the same unknown origin as the slight asymmetry in the DW depinning data in Figure 10.2(f).

10.4 Discussion & conclusion

We now briefly discuss the origin of the unexpected chiral effective fields in Pt/Co/Pt. It was recently calculated [239] that a significant DMI can arise in a Pt/Co bilayer, leading to a effective chiral field of several 100 mT. Since the chiral field in Pt/Co/Pt is the result of two canceling interfaces, we should stress that an imbalance between the DMI at the top and bottom interface of only a few percent is enough to achieve the measured magnitude. Ryu *et al.* [206] argued that DW motion in the direction of current flow implies that the bottom interface dominates. Due to growth-related phenomena, it is known that the top and bottom interface can have different characteristics, for example evidenced by a different contribution to the effective PMA [240]. Apparently, the DMI at the top interface decreases when reducing the top layer thickness, such that the net DMI increases. It is worth noting that although the DMI at the top layer appears to decrease, the PMA constant increases for thinner Pt top layers (see Table C.1). In an inverted Pt(2)/Co/(0.5)/Pt(4) sample (Appendix C, Figure C.1), it was found that the DMI almost vanishes, but does not change sign, thus the interfaces appear to become more symmetric for thick capping layers. This indeed suggests that interface characteristics are key, rather than the thickness of the layers themselves. Reasons for the top interface to vary with thickness can be changes to the mode of growth, different interdiffusion [240] or even slight oxidation at the top Co/Pt interface in case of thin capping layers.

To summarize, the effective chiral magnetic field in Pt/Co systems turns out to be tunable by varying the top layer thickness and material. The effect scales with the degree of structural inversion asymmetry and leads to a gradual change of the stable wall type from Bloch to Néel. Furthermore, by using the DW resistance as an independent measurement of the internal DW structure, a change of the internal structure from Bloch-like to Néel under longitudinal fields was evidenced, and correlated to the high efficiency of DW motion of Néel walls. These findings firmly establish SHE and DMI as a tandem for efficient and coherent DW motion.

10.5 Methods

Sample fabrication: All samples consisted of 1.5 µm wide strips fabricated on Si/SiO_2 substrates by Electron-Beam lithography, DC sputtering, and lift-off. The Pt(4)/Co(0.8)/Al(1.5) samples were oxidized in a 15 W, 0.1 mbar O_2 plasma for 10 minutes to obtain Pt/Co/AlOx. These samples were annealed for 20 minutes at 573 K. The Pt/Co/Pt samples did not undergo an annealing treatment. The samples were designed to form an on-sample Wheatstone bridge configuration to be able to measure resistance changes accurately (for details see Chapter 8 [238]). The samples were locally irradiated with a 30 keV Ga FIB to make it possible to create a stable domain pattern with a well-defined number of DWs. At

the same time, the edges of the irradiation boundaries acted as pinning sites, to enable the well-controlled depinning measurements. The Ga doses were chosen to ensure that all DWs are stable during DWR measurements and amounted to 1.13×10^{13} ions/cm^2 on Pt/Co/AlOx, 0.50×10^{13} ions/cm^2 on Pt(4)/Co(0.5)/Pt(2) and Pt(4)/Co(0.4)/Pt(2), and 0.81×10^{13} ions/cm^2 on Pt(4)/Co(0.4)/Pt(1). Table C.1 (in Appendix C) provides the material parameters (PMA constant and M_s) obtained by SQUID magnetometry on unpatterned films.

DW depinning measurements: Very low DC current densities in the range $\pm 2 \times 10^{10}$ A/m^2 were used to exclude significant effects from Joule heating and Oersted fields. The current and in-plane field are kept constant, while the z-field is being ramped up until both DWs have depinned which is automatically detected by an image analysis routine. This is repeated at least 10 times for each current point to obtain sufficient signal to noise. Table C.1 presents the fit parameters of the 1D model (H_K, H_D and ϵ_{SHE}) for each used material composition, and compares the latter to the expected efficiency ϵ_{calc} based on the layer thicknesses.

DW resistance measurements: Our measurement routine is very similar to what we described in Chapter 8. We use a combination of an on-sample Wheatstone bridge and a lock-in technique to measure the resistance change due to the presence of DWs. The in-plane field is applied constantly, and first the strip is saturated (zero DWs) by a negative H_z, and the lock-in voltage at $H_z \approx -1$ mT is recorded. Then, the DWs are created by a positive H_z, the field is reduced to $H_z \approx 1$ mT and the lock-in voltage is recorded again. The difference is presented in Figure 10.3 as ΔR, and represents the resistance change due to all the DWs (20 or 18 for Pt/Co/Pt and Pt/Co/AlOx, respectively). Since the background voltage is recorded at the same in-plane field as the voltage in the presence of DWs, AMR effects from magnetization canting in the bulk of the domains is automatically filtered out, leaving only resistance changes in the DW region. We always check the number of DWs present in the sample by real-time comparison to a Kerr-microscopy image. The small H_z during measurements serves to ensure the DW pattern remains stable during measurements. An AC probe current of 1 mA (0.75 mA) at 500 Hz was sent through two parallel Pt(4)/Co(0.5)/Pt(2) (Pt(4)/Co(0.8)/AlOx) strips and it was verified that a lower amplitude does not significantly alter the results. Note that a sample with slightly thicker $t_{\mathrm{Co}} = 0.5$ nm had to be used, because the samples with $t_{\mathrm{Co}} = 0.4$ turned out to be very easily switched by the SHE from the probe current. Therefore, much lower probe currents have to be used, and the thinner magnetic Co layer further deteriorates the signal/noise. Details on the modeling of in-plane field effects on the measured DW resistance are presented in Appendix C.2, and the individual contributions to the modeled resistance are plotted in Figure C.2.

As mentioned at several points, Appendix C provides valuable additional information to this Chapter.

Conclusion & outlook

Conclusion

In the introduction of this thesis, we formulated two general aims: to explore various approaches to DW pinning (Part I), and to identify the main mechanisms that dominate the controversial current-induced DW motion in PMA materials (Part II).

Regarding DW pinning, we found that engineering the DW pinning potential by acting directly on the anisotropy parameter works reliably in PMA materials (Chapter 2). In particular, focused ion beams enable the design of an as-desired energy landscape at the length scale of the DW. The demonstration of a ratchet DW shift register in Chapter 3 by making use of irradiation gradients, underlines this point. Although perfect for laboratory prototypes, focused ion beams are less suitable for use in mass production. In that sense, modifying the anisotropy through a voltage gate (Chapter 5) might be more promising, since its fabrication is more conventional, and the pinning can be toggled even after device fabrication.

Regarding current-induced DW motion, we found that spin-dependent transport through our ultrathin Co layers gives rise to a DW resistance depending on the DW width (Chapter 8), but the dominant driving force of DW *motion* actually arises from the adjacent Pt layers. The spin Hall effect in Pt leads to a perpendicular spin current that exerts a strong torque on Néel walls in the Co layer (Chapter 9). In fact, it has been suggested that the potential efficiency of SHE-induced DW motion is at least an order of magnitude bigger than conventional DW motion [193], and indeed, very high velocities of several 100 m/s have already been reported [206]. The fact that Néel walls of fixed chirality are stabilized in systems with asymmetric interfaces [204–206], which is surprisingly also observed in Pt/Co/Pt with asymmetric layer thicknesses (Chapter 10), is a beautiful coincidence that brings racetrack memory a step closer to becoming reality.

Outlook

Although we found strong indications that DW motion is dominated by the spin Hall effect in our materials, the discussion is still on-going, because in some materials grown by other groups a strong Rashba-like torque is still measured. Notably, Garello *et al.* [232] recently proposed a new measurement scheme for spin-orbit torques, and identified novel anisotropic contributions to the field-like and

Slonczewski-like torques, of which the relative strength depended on fabrication details. This definitely requires further experiments and the development of a more complete theory.

Regarding direct follow-up work to this thesis, some outlook was already provided in each of the individual Chapters. The most important outstanding question is the precise mechanism behind the Dzyaloshinskii-Moriya interaction in Pt/Co/Pt, on which we could only make some speculations in Chapter 10. By making more variations to the material system, and by studying the nature of the interfaces using more direct characterization techniques, it may be identified what exactly causes the tunable asymmetry between the top and bottom interface.

Because of the many recent developments such as spin-orbit torques, electric field effects, ratchets, etcetera, it is tempting to make a detailed proposal of how to integrate these phenomena into the ultimate memory chip. But given the rapid succession in which new developments are still reported, such an idea is might already be outdated when this thesis hits the presses. Furthermore, a lot of decisions in device design will have to be made from the point-of-view of expert device engineers with a keen eye on costs and scalability. Still, we can discuss the potential of the various new tools that are now at the disposal of engineers. If we limit ourselves to a racetrack-like geometry, the ratchet that we proposed in Chapter 3 might be interesting. However, device engineers are not too fond of introducing magnetic fields into integrated circuits, so this would require a deviation from standard chip design principles. On the other hand, the ratchet principle can be applied equally well in current-driven DW motion, and in fact we originally thought of using a ratchet to coherently move DWs by the spin Hall effect. Since DMI has emerged as the companion of the spin Hall effect for coherent DW motion, the ability to move DWs in only one direction might be too big a price to pay in exchange for the discretized shift register that the ratchet provides. In that sense, voltage-gated pinning might be an ideal solution: when the voltage is on, the DW will pin at the well-defined position of the gate edge, and when the voltage is removed, the DW can be propagated at a much lower current because, theoretically, there is no pinning at all. On the other hand, this requires an electrode grid which obviously occupies space, hence might turn out not to be practical. In that case, some way of permanent anisotropy modification might still be favorable for creating pinning sites. In any case, the spin Hall effect, either with or without the addition of conventional STTs, seems a very promising way to move the DWs, and provides endless tunability options. In fact, it is not only efficient for DW motion (transporting existing bits), but for magnetization switching (writing a new bit) as well, so that clever schemes can be devised in which all data operations occur via the spin Hall effect. Furthermore, it was recently suggested that it might be advantageous to use chiral vortex-like spin textures called skyrmions for data representation in a racetrack[241], and the SHE is likely also capable of efficiently moving these.

To conclude, developments in spintronics are evolving at a fast pace. The GMR and TMR effects provide an excellent example of how quickly scientific discoveries can be put to use in consumer devices. Let us hope this will continue to happen with current worldwide research efforts, to which this thesis made a small contribution.

Supplementary information on Chapter 6

A

A.1 Stray field calculation

As known from elementary electromagnetism, a magnetized object generates bound currents. A simple way to calculate the stray fields of such an object is to find the magnetic field generated by those currents. In a uniformly magnetized pillar, the bound volume current $\mathbf{J}_b = \nabla \times \mathbf{M}$ vanishes, but there remains a bound surface current $\mathbf{K}_b = \mathbf{M} \times \hat{n} = M_s \hat{\phi}$. So, a total current of $M_s \times h$ flows over the curved cylinder surface, with h the cylinder height. We calculate the field produced by this current by dividing the cylinder into N tiny slices, each of which is a current loop with $I = \frac{M_s \cdot h}{N}$. Starting from the Biot-Savart law, the following expression can be derived for the position-dependent r- and z-components of the magnetic field produced by a single current loop of radius a [242],

$$H_r(r,z) = H_0 \frac{\gamma}{\pi\sqrt{Q}} \left(E(k^2) \frac{1+\tilde{a}^2+\tilde{z}^2}{Q-4\tilde{a}} - K(k^2) \right), \tag{A.1}$$

$$H_z(r,z) = H_0 \frac{1}{\pi\sqrt{Q}} \left(E(k^2) \frac{1-\tilde{a}^2-\tilde{z}^2}{Q-4\tilde{a}} + K(k^2) \right), \tag{A.2}$$

where $\tilde{a} = \frac{r}{a}$, $\tilde{z} = \frac{z}{a}$, $\gamma = \frac{z}{r}$, $Q = (1+\tilde{a})^2 + \tilde{z}^2$, $k^2 = \frac{4ar}{(a+r)^2+z^2}$, and $H_0 = \frac{I}{2a}$ (the field in the center of the loop). $K(k^2)$ and $E(k^2)$ furthermore represent the complete elliptical integrals of the first and second kind,

$$K(k^2) = \int_{\vartheta=0}^{\frac{\pi}{2}} \frac{d\vartheta}{\sqrt{1-k^2\sin^2\vartheta}}, \tag{A.3}$$

$$E(k^2) = \int_{\vartheta=0}^{\frac{\pi}{2}} \sqrt{1-k^2\sin^2\vartheta}\, d\vartheta. \tag{A.4}$$

We used a MATLAB script to calculate the field produced by a superposition of N loops. As a simplification, we assume that the DW only senses the z-component of the field, which is, in principle, valid if the DW is very small*. We calculate the field in the plane $d = 2\,\text{nm}$ (the thickness of our Pt cap layer) below the first loop, by summing Eq. (A.2) over all N loops,

$$H_{z,\text{tot}} = \sum_{i=1}^{N} H_z(r, -d - \frac{h}{N}(i + \tfrac{1}{2})). \tag{A.5}$$

Figure A.1 shows 2D plots of $H_{z,\text{tot}}$ for two different pillar heights, magnetized in the $-z$ direction. We choose $M_\text{s} = 100\,\text{kA/m}$, the pillar radius $a = 30\,\text{nm}$, and divided the pillar into $N = 50$ slices. Comparing Figure A.1(a) and (b), it is observed that the smaller pillar produces higher stray fields in a ring around the pillar (white area around the pillar), whereas the taller pillar has higher (negative) stray fields right underneath the pillar (darker black dot in the center). However, this does not directly gives us the minimum and maximum field experienced by the DW *as a whole*. If we assume a 1D profile of the DW that varies only in the x-direction, the DW feels the field strength averaged over its length, which is along the entire width of the strip (500 nm) spanning the y-axis. The average z-field as a function of DW position x is plotted in Figure A.1(c-d). The extrema in Figure A.1(c-d) directly give us the pinning and pulling field as defined in Chapter 6. The results of these calculations as a function of pillar height are shown in Figure 6.3(b).

As discussed, the limitation of this model is the fact that the DW does not fully retain its 1-dimensional character, and the in-plane stray fields also play a role since the DW has finite width. This is exactly what was taken into account in the full micromagnetic simulations in Figure 6.3(b), which give slightly different results.

A.2 Coercive field calculation

Here, we derive an expression for the coercive field of a pillar in a Stoner-Wohlfarth model, assuming that the magnetization in the pillar remains uniform during switching. The two energy terms that play a role are the Zeeman energy due to the interaction of the magnetization with the externally applied magnetic field H_ext, and the shape anisotropy K_s that the pillar exhibits because it is elongated in the z-direction. Hence, the total energy density of the system can be written as

$$u = K_\text{s} \sin^2\theta - \mu_0 M_\text{s} H_\text{ext} \cos(\alpha - \theta), \tag{A.6}$$

where θ is the angle of the magnetization vector and α the angle of the externally applied field, both with respect to the z-axis. Like in the experiment, the external field is applied in the z direction, so $\alpha = 0$. According to the Stoner-Wohlfarth theory, the magnetization direction of a magnetized object reverses upon a sign reversal of the second derivative of the energy density w with respect to θ. Because

*If the DW is infinitely small, the magnetization in the DW strip does not have any in-plane regions, and therefore the Zeeman energy due to in-plane fields does not depend on the position of the DW and does not contribute to DW pinning.

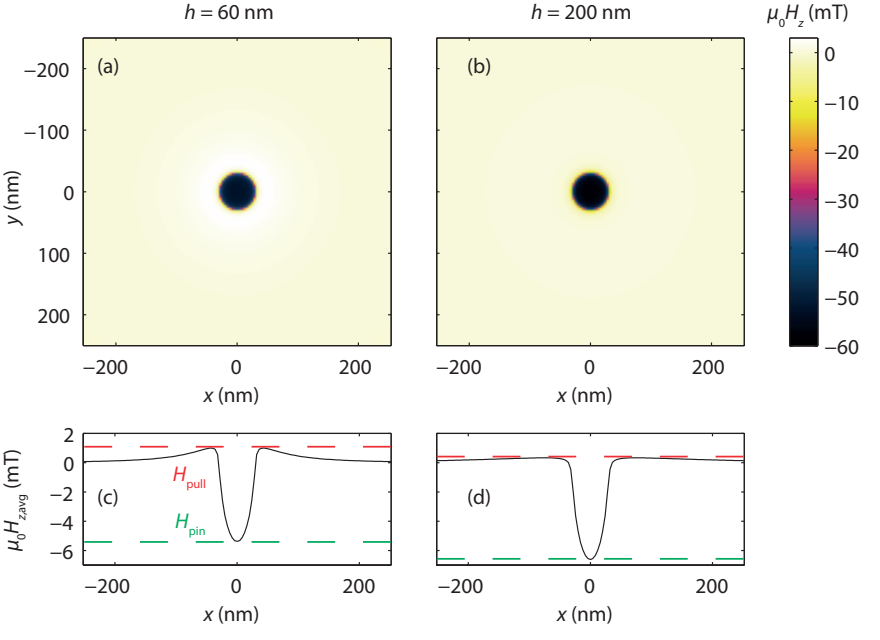

Figure A.1 | Calculated z-stray fields of pillars with height 60 nm (a) and 200 nm (b). (c) and (d) show the same data averaged over the y-direction. The minimum and maximum are defined as H_{pin} and H_{pull}, respectively.

of symmetry considerations, any angle other than $\theta = 0$ or π is unstable, hence $\theta = 0$ at the moment the switch occurs. Hence, the switching condition reads

$$\left.\frac{\partial^2 w}{\partial \theta^2}\right|_{\theta=0} = 2K_s + \mu_0 M_s H_{\text{ext}} = 0, \tag{A.7}$$

yielding

$$\mu_0 H_{\text{ext}} = \frac{-2K_s}{M_s}. \tag{A.8}$$

The remaining task is to find an expression for the shape anisotropy constant K_s. For simple shapes like ellipsoids, the shape anisotropy of a magnetized object scales with the difference between the demagnetizing factors along the easy and hard axis, or more explicitly[157]:

$$K_s = \frac{\mu_0 M_s^2}{2}(N_x - N_z) = \frac{\mu_0 M_s^2}{4}(1 - 3N_z), \tag{A.9}$$

where N_x and N_z represent the demagnetizing factors in respectively the x (hard axis) and z (easy axis) direction. Note that also $N_x + N_y + N_z = 1$ and $N_x = N_y$ have

been used to rewrite the expression. To calculate N_z, we use the expression for the magnetometric demagnetizing factor of a uniformly magnetized cylinder from [156]:

$$N_z = 1 - \frac{2}{2\pi p}\left\{(1+p^2)^{\frac{1}{2}} \times \left[p^2 K(k) + (1-p^2)E(k)\right] - 1\right\}, \tag{A.10}$$

with $k = \left(1+p^2\right)^{-1}$ and $p = \frac{h}{2a}$ the aspect ratio of the pillar. $K(k)$ and $E(k)$ again represent the complete elliptic integrals of the first and second kind defined in (A.3) and (A.4).

Finally, to find values for the coercive field of a pillar, we combine equations (A.8), (A.9) and (A.10). The coercive field as a function of pillar aspect ratio p was shown in Figure 6.5.

Supplementary information on Chapter 9

B

B.1 Predicted ϵ from the nonadiabatic torque

In Chapter 9, we have shown that the conventional torques are of negligible influence on the depinning. However, the role of both the adiabatic and nonadiabatic spin transfer torques has been well-established, especially in in-plane materials, and the present research does not exclude the existence of these torques. Here, we will briefly discuss the expected influence of the nonadiabatic torque, since high DW velocities are usually ascribed to this torque.

ϵ can be related to β via the 1D framework developed by Thiaville *et al.* [10]

$$\epsilon = \frac{\beta P \hbar}{2 e M_s \lambda}, \tag{B.1}$$

which yields $\epsilon \approx 0.75\beta$, using $P = 0.4$, $M_s = 1.4 \times 10^6\,\mathrm{Am}^{-1}$, $\lambda = 1.5 \times 10^{-8}\,\mathrm{m}$, $A = 6.5\,\mathrm{nm} \times 1.5\,\mu\mathrm{m}^2$. Here, we have overestimated the expected value of β, since a constant current density is assumed ($\sim$ 8% through Co), whereas the current density in Co is expected to be lower ($\sim$ 3%) [216], as argued in Chapter 8. Since the dynamics of both DWs differ only by the sign of their magnetization gradient, the contribution of β to ϵ can be estimated by the difference in responses (ϵ_{DW1} and ϵ_{DW2}) of the 2 DWs:

$$\epsilon_\beta = \frac{\epsilon_{\mathrm{DW1}} - \epsilon_{\mathrm{DW2}}}{2}. \tag{B.2}$$

No consistent ϵ_β was found in our data. However, ϵ_β of the order 0.1 ($\beta \approx 0.13$) would fall within the uncertainty of our experiment.

B.2 Pinning field as a function of in-plane field

As was shown in Figure 9.2, at zero current, the pinning field is dependent on both H_x and the perpendicular magnetization direction. This behavior is probably caused by the local energy landscape of the depinning center, and differs per pinning site and nanostrip in a nonsystematic way. Figure B.1 shows the observed values of H_{pin} as a function of H_x, without applied current, measured on two nominally equal Pt (2 nm) / Co (0.5 nm) / Pt (4 nm) nanostrips that were grown in one run on the

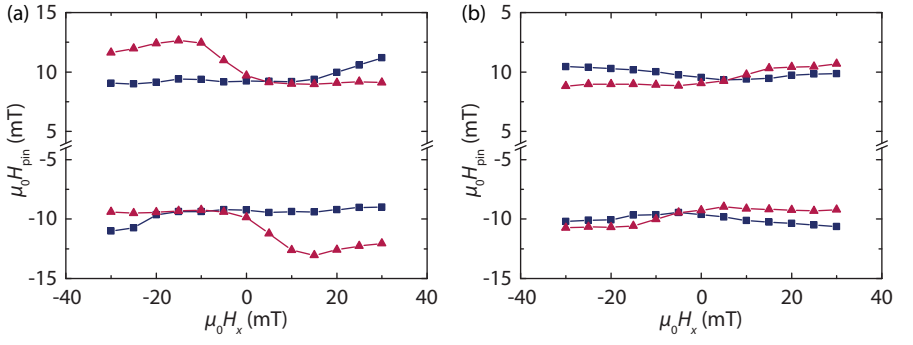

Figure B.1 | Typical measurements of pinning field without current as a function of H_x. (a) and (b) are two nanostrips on the same Pt (2 nm) / Co (0.5 nm) / Pt (4 nm) sample. The red triangles and the blue squares denote the two walls of a single domain, analogous to Figure 9.2. No correlation between nanostrips or pinning sites in the behavior of H_{pin} without current as a function of H_x could be found; the dependence is governed by the local defect structure near the pinning centers.

same sample. As can be seen, the observed behavior of H_{pin} as a function of H_x does not reproduce, and no correlation can be found between depinning sites.

Note that, in a sample without disorder or defects, $|H_{\text{pin}}|$ at zero current should have even more symmetry than is observed in Figure B.1: it should be an even function of H_x, and independent of the perpendicular magnetization direction of the domain. In the experimental data, there is an additional symmetry breaking factor that breaks the symmetry under 180° rotation of the magnetization around the z-axis and 180° rotation around the x-axis. This symmetry breaking can be explained by considering that the ferromagnetic layers, although macroscopically symmetric under these rotations, have an internal defect structure, which influences the magnetization, and can therefore explain the observed symmetries in Figure B.1. This may also be related to the structural inversion asymmetry that causes a small DMI in Chapter 10. Apart from this unpredictable variation of offsets, the current-induced behavior of ϵ is highly reproducible, as one can readily see in the similar behavior of the two DWs in Figure 9.3.

B.3 Micromagnetic simulations

To study the depinning behavior of a DW subjected to a Slonczewski torque, we have performed 1D micromagnetic simulations, based on (9.2). In this section, we will present more details on these simulations.

The extended LLG equation (9.2) has been solved on a 1D grid of 100 sites with 4 nm spacing. The exchange interactions and perpendicular anisotropy are included as effective fields. Since the conventional torques do not give a significant contribution to ϵ in our experiments, they are not included in the simulations. The demagnetization fields in the x direction are determined at each timestep by

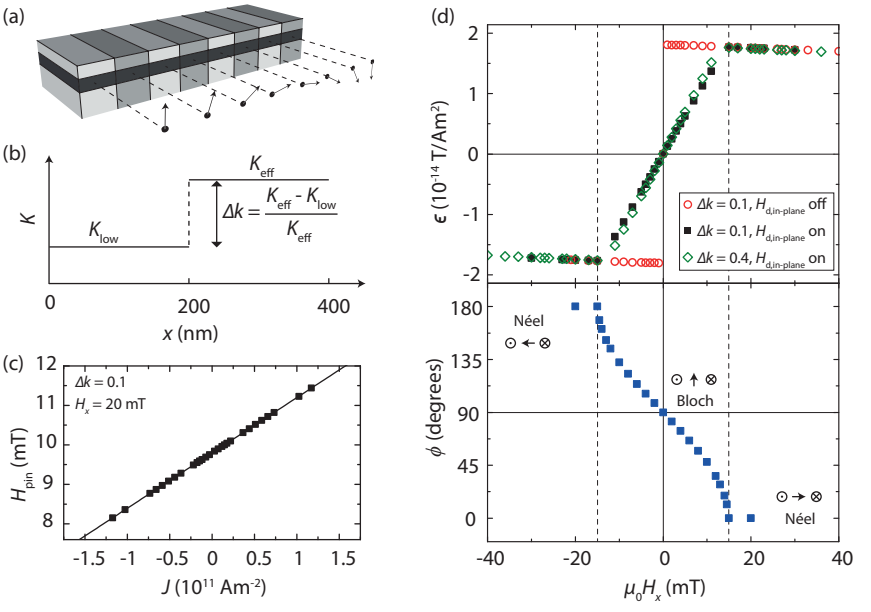

Figure B.2 | ϵ as a function of H_x as determined by micromagnetic simulations. (a) Cartoon of the discretization of the magnetization, used for the micromagnetic simulations of the depinning behavior; (b) The change in anisotropy is modeled as a step in the effective anisotropy K_{eff} at the center of the simulation region. (c) Simulation results of the dependence of H_{pin} on the current density in a Pt (4 nm)/Co (0.5 nm)/Pt (2 nm) film. The red line is a linear fit of the data points. (d) Results of micromagnetic simulations: in the top graph, ϵ is plotted as a function of H_x, for two step heights and once without the in-plane demagnetization fields. The bottom graph shows the in-plane angle of a DW in equilibrium without SHE or anisotropy steps.

calculating the field of the magnetic surface charges between the sites. The demagnetization fields in the y direction were neglected, since a very wide nanostrip was assumed. The demagnetization fields in the z direction are included as a uniform shape-anisotropy correction to the perpendicular anisotropy, which holds in the limit of an infinitely thin film. To check the validity of our simulations, we have verified that we can reproduce the standard DW profiles, as well as the current-driven behavior by the conventional torques, including the Walker breakdown transition.

The strength of the effective perpendicular anisotropy, was lowered on one side of the grid to simulate the Ga-irradiated region, as can be seen in Figure B.2(b). On the right side, the effective anisotropy is unchanged, with $K_{\text{eff}} = 0.268\,\text{MJ}\,\text{m}^{-3}$. On the left side, the anisotropy is decreased by a relative factor Δk, so that the effective anisotropy on the left side equals $K_{\text{low}} = (1 - \Delta k)K_{\text{eff}}$.

To calculate the pinning field for a fixed H_x and Slonczewski torque, the DW is first allowed to relax without a perpendicular H_z field for 30 ns. Then, H_z is incremented in steps of 10^{-5} T, and the magnetization is again allowed to relax

for 15 ns in between these increments. After each increment of H_z, the state of the spins in the right region is inspected. If the perpendicular component of the magnetization direction is reversed in this region, the current H_z field is saved as the pinning field H_{pin}. This procedure is repeated for different values of H_x and Slonczewski torque magnitude.

To calculate the net spin Hall current, we have used the spin Hall angle of Pt, $\theta_{\text{SH}} = 0.068$ from ref[185]. In the same article, the thickness dependence of the spin Hall current on the Pt layer thickness is experimentally studied in the range 2-10 nm, from which one can deduce that the net spin Hall current is only $\nu = 35\%$ of the bulk value for Pt/Co/Pt stacks with 2 nm and 4 nm thick Pt layers via (9.1). The resulting torque is added to the LLG equation as described by (9.2), with the prefactor:

$$\tau_{\text{SL}}^{\text{SHE}} = \nu \frac{\gamma \hbar \theta_{\text{SH}}}{2eM_s t} J,$$

with e the electron charge, t the Co layer thickness, μ_0 the permeability of free space, J the current density and $\hbar$ the reduced Planck's constant. The other simulation parameters that were used are the exchange stiffness constant $A = 1.6 \times 10^{-11}\,\text{Jm}^{-1}$, the saturation magnetization $M_s = 1.4 \times 10^6\,\text{Am}^{-1}$, and a Gilbert damping constant of $\alpha = 0.1$.

Analogous to the experimental results, the calculated H_{pin} has a linear dependence on the current density, as can be seen in Figure B.2(c), where H_{pin} is plotted as a function of the current density at an in-plane field of $\mu_0 H_x = 20\,\text{mT}$. Finally, in Figure B.2(d), the dependence of ϵ versus the in-plane field is depicted. A gradual change in the internal angle of the DW was visible in the simulations. At $\mu_0 H_x = 0\,\text{mT}$, the DW is of the Bloch type, and there is no influence of the current on H_{pin}. At higher H_x, the internal angle of the DW aligns with the H_x, and at approximately $\mu_0|H_x| = 15\,\text{mT}$, the Néel wall is stabilized and ϵ levels off. To see the correspondence between ϵ and the DW structure, in the bottom pane of Figure B.2(d), the internal angle of the DW, without a spin Hall current or anisotropy step, is plotted as a function of H_x. A clear correspondence can be observed between the saturation of the in-plane DW angle and the saturation of ϵ. Furthermore, the calculations have been repeated without the in-plane demagnetization fields, which leads to a step in ϵ as a function of H_x, because the DW is now free to align with the applied H_x field.

To study the influence of the anisotropy step height Δk, the calculations have been repeated for multiple step heights (open diamonds and solid squares in Figure B.2(d)). As can be seen in Figure B.2(d), the behavior of ϵ is hardly influenced by the step height, hence the field-current equivalency is robust against variations in the pinning strength. Therefore, although the offset in H_{pin} is much lower in experiments compared to simulations due to thermal activation and a more gradual anisotropy transition, the measured slopes are very well comparable to this model.

B.4 Magnitude of Rashba contributions

In Pt/Co/AlOx, it was proposed that a strong Rashba field in the y-direction (H_{R}) can be induced by a current running in the x direction, due to the lack of structural

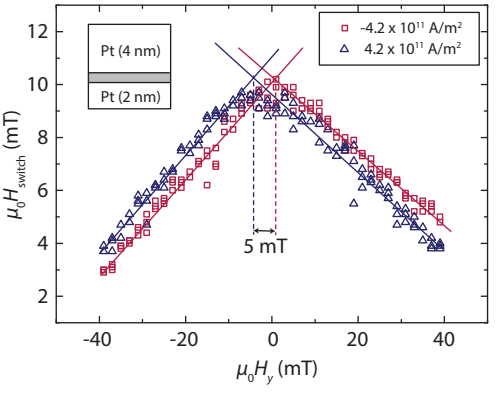

Figure B.3 | Switching field of a Pt (2 nm) / Co (0.5 nm) / Pt (4 nm) strip as a function of in-plane current. Inverting the sign of the current yields only a 5 ± 3 mT shift in the graphs, indicating that the H_y field generated by the current is much lower than that for typical Rasbha fields observed in Pt/Co/AlOx. The lines are guides to the eye.

inversion symmetry. This field scales linearly with the current, with a prefactor $\mu_0 H_R/J$ of $1 \pm 0.1 \times 10^{-12}$ Tm^{2}A^{-1} [172]. Nonadiabatic contributions from H_R have been predicted to have the same symmetry as the Slonczewski-like torque from the SHE, although such effects have never been measured in a separate experiment before. Like discussed in Chapter 7, in Pt/Co/AlOx there has been a discussion on whether these nonadiabatic contributions of H_R could contribute to the switching that was observed with an H_x field and an in-plane current [84]. Here, we will show experimentally that these contributions are very small and that Rashba effects are negligible in our Pt/Co/Pt structures.

The existence of a net H_R can only arise in structurally asymmetric layers. In Pt/Co/Pt structures, the Co is enclosed between two similar interfaces, and no significant influences from a net Rashba field are expected. Indeed, the existence of a net Rashba field in Pt (3 nm) / Co (0.6 nm) / Pt (3 nm) nanostrips was already refuted by Miron *et al.* [172]. Small Rashba effects could in principle arise from second-order contributions, such as growth-related differences in the interface or unequal current densities at the interfaces [29].

To study the magnitude of H_R due to these effects in Pt/Co/Pt structures with unequal Pt thickness, we have studied the dependence of the switching field H_{switch} on the in-plane field H_y for different current directions. Generally, the switching field of perpendicularly magnetized materials is lowered when in-plane fields are applied, an effect which was also exploited by Miron *et al.* [172]. When an H_R is induced, it will enhance or oppose the applied H_y field, resulting in a shift in the dependence of H_{switch} on H_y.

Figure B.3 shows the dependence of H_{switch} as a function of H_y for a Pt (2 nm) / Co (0.5 nm) / Pt (4 nm) nanostrip. Note that the current densities here are $\sim 20\times$ higher than used to study the DW depinning. Still, the observed shift between

the positive and negative current direction is very small, 5 ± 3 mT, corresponding to a prefactor $\mu_0 H_R/J \approx 1.2 \times 10^{-14}$ T/m^2, almost two orders of magnitude lower than that observed in Pt/Co/AlOx by Miron [172]. Such a small direct Rashba field would yield an even smaller nonadiabatic Rashba effect. Furthermore, these current-induced fields in the y-direction can also be explained by considering the Oersted fields generated by the current.

B.5 Magnetization reversal of $(4,2)$ and $(2,4)$ stacks

The magnetization switching experiments on $(4,2)$ nanostrips have been repeated on Pt $(2,4)$ and Pt $(3,3)$. For the Pt $(3,3)$, no switching was observed, which we ascribe to an almost perfect cancelation of the two spin currents. The Pt $(2,4)$ does switch under the application of current pulses, with a sign of the stable magnetization direction opposite tot that observed for the Pt $(4,2)$ stack, as can be seen Figure B.4.

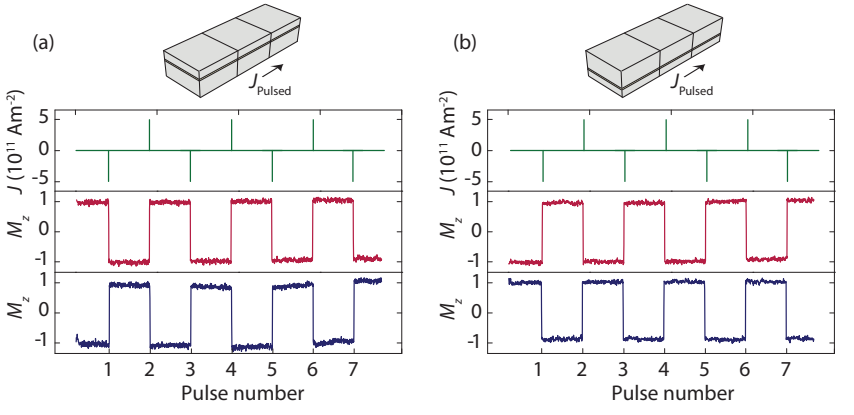

Figure B.4 | SHE-driven magnetization switching of (a) Pt (4 nm) / Co (0.5 nm) / Pt (2 nm) and (b) Pt (2 nm) / Co (0.5 nm) / Pt (4 nm). The effect reverses, analogous to the sign reversal of the DW depinning that was shown in Figure 9.3. The red (middle) and blue (bottom) lines denote the perpendicular component of the magnetization for $H_x = -20$ mT and $H_x = 20$ mT, respectively, after injection of alternating pulses.

Supplementary information on Chapter 10

C

C.1 Material parameters

	M_s MA/m	K_{eff} MJ/m^3	$\mu_0 H_D$ mT	$\mu_0 H_K$ mT	ϵ_{SHE} 10^{-14} TA^{-1}m^2	ϵ_{calc}	ν
$Pt_4/Co_{0.36}/Pt_1$	1.01(5)	0.39(2)	37(1)	37(1)	6.4(2)	6.7	0.68
$Pt_4/Co_{0.36}/Pt_2$	1.08(5)	0.27(1)	12.5(4)	24.6(5)	2.76(6)	3.2	0.34
$Pt_4/Co_{0.8}/AlOx_{1.9}$	1.17(5)	0.28(1)	$\gg 40$	?	4.43(6)	3.4	0.89
$Pt_4/Co_{0.5}/Pt_2$	1.07(5)	0.28(1)	11(2)	37(1)	2.4(1)	2.3	0.34
$Pt_2/Co_{0.5}/Pt_4$	1.18(5)	0.22(1)	3(1)	19(2)	-1.8(1)	-2.1	-0.34

Table C.1 | Fit parameters and material properties of various compositions.

Table C.1 summarizes the measured material properties. M_s and K_{eff} have been measured by VSM-SQUID magnetometry of unpatterned films. The samples labeled with a Co thickness of 0.4 nm in the text for convenience, were actually 0.36 nm thick. $\mu_0 H_D$, $\mu_0 H_K$, and ϵ_{SHE} have been obtained by fits of the DW depinning data like in Figure 10.2. The inverted stack Pt(2)/Co(0.5)/Pt(4) also has an inverted ϵ_{SHE}, as we already explained in Chapter 9[233]. Figure C.1 provides a new measurement of the depinning efficiency as a function of H_x on this layer system, similar to Figure 9.3(c) but with slightly better accuracy, in order to reveal the presence of DMI. There is a very small opening visible, indicative of a H_D with the same sign as the inverted composition. Actually, it seems like one of the DWs has zero H_D (crosses through the origin), whereas the other one has a small but finite H_D. In any case, this suggests that the DMI, unlike the SHE, is not a result of the Pt layer thicknesses themselves, but rather the effect of increasing asymmetry between the top and bottom interface properties when the top layer is varied.

Since both DMI and PMA are expectedly interface effects, it is interesting to look for correlations between the parameters H_D and K_{eff}. For the Pt/Co/Pt samples, there is indeed a positive correlation between H_D and K_{eff}. However, Pt/Co/AlOx breaks this trend: it has a much stronger H_D than any other sample whereas K_{eff} is similar, so the two parameters are definitely not always directly related. Given that the DW motion is in the direction of current flow, we know that the DMI at the

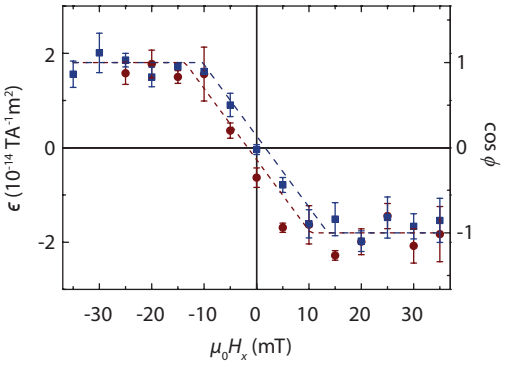

Figure C.1 | Depinning efficiency as a function of H_x on the inverted stack Pt(2)/Co(0.5)/Pt(4).

bottom interface must be dominant over the DMI from the top interface [206]. So in fact, the DMI at the top interface must *decrease* when the top layer is made thinner, whereas the anisotropy contribution from this interface is actually seen to *increase*. So there appears to be a *negative* correlation between the anisotropy and DMI at the top interface, leading to a *positive* correlation between the anisotropy and the total DMI which is dominated by the bottom Pt/Co interface.

C.1.1 Spin Hall amplitudes

In the last two columns of Table C.1, we have calculated the expected loss factor ν of the spin Hall effect, and the accompanying depinning efficiency of Néel walls in the 1D model [204],

$$\epsilon_{\mathrm{calc}} = \frac{\pi\hbar\nu\,\theta_{\mathrm{SH}}}{4eM_{\mathrm{s}}t}. \tag{C.1}$$

The calculation of ν is straightforward, as discussed in section 9.2; the net spin Hall current due to a *single* thin Pt layer with thickness t_{Pt} is given by [191]

$$J_{\mathrm{s}}(t_{\mathrm{Pt}}) = \theta_{\mathrm{SH}}J\left(1-\mathrm{sech}\left(\frac{t_{\mathrm{Pt}}}{\lambda_{\mathrm{sf}}}\right)\right), \tag{C.2}$$

with $\lambda_{\mathrm{sf}} \approx 1.4\,\mathrm{nm}$ the spin diffusion length of Pt [185] and $\theta_{\mathrm{SH}} = 0.07$ the spin Hall angle of Pt [185]. For a Co layer sandwiched between two Pt layers, two of these spin currents with opposite polarization are injected, yielding a net spin current

$$J_{\mathrm{s}}^{\mathrm{eff}} = \nu\,\theta_{\mathrm{SH}}J = \left(\mathrm{sech}\left(\frac{t_{\mathrm{t}}}{\lambda_{\mathrm{sf}}}\right) - \mathrm{sech}\left(\frac{t_{\mathrm{b}}}{\lambda_{\mathrm{sf}}}\right)\right)\theta_{\mathrm{SH}}J. \tag{C.3}$$

Comparing the calculated ϵ_{calc} to the measured ϵ_{SHE} in Table C.1, we observe close agreement. The largest deviation is found in Pt/Co/AlOx which measures a slightly higher ϵ_{SHE} than expected. We should note that this is the only sample that has

undergone an annealing treatment, hence it might have different properties compared to the other ones. There might also be a contribution from conventional STT to ϵ_{SHE} in Pt/Co/AlOx, but since conventional STT would oppose the SHE torque, this should reduce the measured ϵ_{SHE} compared to the model, whereas the difference we observe is opposite.

C.2 DW resistance model

In this section, we propose a model to describe the two dominant contributions to the DW resistance. We first apply the Levy-Zhang model of the intrinsic resistivity to the expected DW profile in the sample. Then, we discuss the contribution from anisotropic magnetoresistance (AMR). Finally, an expression is given for the measured resistance change in an actual Pt/Co/Pt layer, where current shunts through the Pt layers. This expression is fitted to the experimental data.

C.2.1 Levy-Zhang model for arbitrary DW profiles

The Levy-Zhang model describes the contribution to DW resistance due to spin mistracking [171]. In their original derivation, they assume a simplified DW profile of the form $\theta(x) = \pi x/d$. However, in reality the DW has the more complicated Bloch profile, and when magnetization canting due to an in-plane field starts to play a role, the actual profile is even more complex. We therefore first derive an expression valid for any DW profile, and then insert an approximated 'canted' profile to find an expression for R_{LZ} as a function of in-plane field.

The original result of DW resistivity by Levy and Zhang for a current perpendicular to the DW was presented before as (8.3),

$$\rho_{\mathrm{LZ}} = C\left(\frac{\pi}{\lambda}\right)^2, \tag{C.4}$$

with λ the DW width and C a prefactor given by

$$C = \frac{\hbar^4 k_{\mathrm{F}}^2 \rho_0}{80\, m^2 J^2}\left(\frac{\rho_\uparrow}{\rho_\downarrow} - 2 + \frac{\rho_\downarrow}{\rho_\uparrow}\right)\left(3 + \frac{10\sqrt{\rho_\uparrow/\rho_\downarrow}}{\rho_\uparrow/\rho_\downarrow + 1}\right), \tag{C.5}$$

with $\hbar$ Planck's constant, $k_{\mathrm{F}} \approx 1^{-1}$ the Fermi wavevector, m the electron mass, $J \approx 0.5\,\mathrm{eV}$ the (microscopic) exchange splitting, $\rho_\uparrow/\rho_\downarrow$ the spin asymmetry in the Co layer, and ρ_0 the resistivity of the Co layer.

(C.4) was obtained for the simple DW profile with a constant slope $\mathrm{d}\theta/\mathrm{d}x = \pi/\lambda$. For a real DW in which this slope is not constant, the resistivity is position-dependent within the DW. Therefore, a more general form of the DW resistivity is

$$\rho_{\mathrm{LZ}} = C\left(\frac{\mathrm{d}\theta(x)}{\mathrm{d}x}\right)^2. \tag{C.6}$$

The DW resistance is found by integrating the resistivity over the entire DW profile,

$$R_{\mathrm{LZ}}(x) = \frac{1}{S}\int_{-\infty}^{\infty} C\left(\frac{\mathrm{d}\theta(x)}{\mathrm{d}x}\right)^2 \mathrm{d}x, \tag{C.7}$$

with S the cross-sectional area of the magnetic layer.

As explained briefly in Chapter 10, we expect at high in-plane fields a DW profile that rotates from $\theta = 0$ in the non-irradiated region, to $\theta_c(H_x) < \pi$ in the Ga-irradiated region, where the anisotropy has decreased so much that the magnetization is significantly pulled in-plane. We assume a scaled version of the Bloch profile (2.7) that takes into account this smaller final angle of the DW,

$$\theta(x) = \frac{2}{\pi}\theta_c(H_x)\arctan\left(e^{x/\lambda}\right), \tag{C.8}$$

where we use $\lambda = \sqrt{A/K_{low}}$ with $A = 16\,\mathrm{pJ/m}$ and K_{low} the effective anisotropy in the irradiated region (a fit parameter), which is seen to determine the DW width in micromagnetic simulations. From the Stoner-Wohlfarth model, it is straightforward to derive that the magnetization canting as a function of in-plane field is given by

$$\theta_c(H_x) = \pi - \arcsin\left(\frac{H_x M_s}{2K_{low}}\right). \tag{C.9}$$

Plugging the DW profile of (C.8) into the expression for the resistance (C.7) yields

$$R_{LZ}(H_x) = \frac{2C}{S}\frac{\left(\pi - \arcsin\left(\frac{H_x M_s}{2K_{low}}\right)\right)^2}{\pi^2\lambda}. \tag{C.10}$$

Note that we used H_x in the expressions above, but the same expressions hold for H_y, since the LZ resistivity does not depend on the internal angle of the DW.

C.2.2 AMR contribution

The AMR resistivity within the DW scales with the square of the projection of the magnetization on the x-axis, hence

$$\rho_{DWAMR}(x) = \rho_{AMR}\cos^2\phi\sin^2\theta(x), \tag{C.11}$$

where ρ_{AMR} is the AMR resistivity parameter of Co. We will assume that the angle ϕ does not vary within the DW (which is supported by micromagnetic simulations). $\phi = 0$ represents a Néel wall, giving the highest AMR.

If there is no DW present and no canting of the magnetization, the additional AMR contribution in the presence of DWs is found by integrating (C.11). However, if one of the domains is canted in the x-direction, there is a large contribution form this domain to the AMR. This is however not the experimental situation, because the subtracted background signal is recorded at the same in-plane field, hence AMR from the domains is not included in the presented DW resistance. Since we do not have an analytical expression for this background, we start from the original Bloch profile which rotates from 0 to π so that the integral to infinity converges, and multiply (C.11) by a correction factor $\cos^2\theta_c(H_x)$ which is not analytical but at least correct in the center of the DW,

$$\rho_{DWAMR}(x) = \rho_{AMR}\cos^2\phi\sin^2\theta(x)\cos^2\theta_c(H_x). \tag{C.12}$$

Now we only need to integrate the resistivity to get the AMR contribution to the DW resistance,

$$R_{\mathrm{AMR}} = \frac{1}{S}\int_{-\infty}^{\infty} \rho_{\mathrm{DWAMR}}\mathrm{d}x = \frac{1}{S}\frac{\rho_{\mathrm{AMR}}\lambda\left(4K_{\mathrm{low}}^2 - H_x^2 M_{\mathrm{s}}^2\right)\cos^2\phi}{2K_{\mathrm{low}}^2}. \tag{C.13}$$

C.2.3 Converting to actually measured resistance change

The actually measured resistance change is reduced strongly by current shunting through the Pt layers. Assuming only a fraction $p \approx 0.03$ of the current runs through the Co layer in Pt/Co/Pt based on a Fuch-Sondheimer model[238], the resistance of the strip R_{strip} can be described as the result of two parallel resistors $R_{\mathrm{Co}} = \frac{R_{\mathrm{strip}}}{p}$ and $R_{\mathrm{Pt}} = \frac{R_{\mathrm{strip}}}{1-p}$. The occurrence of N DWs only trigger a resistance change of the Co layer ΔR_{Co},

$$\Delta R_{\mathrm{Co}} = N(R_{\mathrm{LZ}} + R_{\mathrm{AMR}}). \tag{C.14}$$

In the parallel resistor model, it is easy to show that this leads to a resistance change of the whole strip of

$$\Delta R = \frac{Np^2(R_{\mathrm{LZ}} + R_{\mathrm{AMR}})R_{\mathrm{strip}}}{R_{\mathrm{strip}} - N(p-1)p(R_{\mathrm{LZ}} + R_{\mathrm{AMR}})}. \tag{C.15}$$

In the Pt(4)/Co(0.5)/Pt(2) strip, $R_{\mathrm{strip}} = 1.3\,\mathrm{k\Omega}$ and $N = 20$, whereas in the Pt/Co/AlOx strip, $R_{\mathrm{strip}} = 1.8\,\mathrm{k\Omega}$ and $N = 18$.

This model for ΔR has been fitted to the DWR data in Figure 10.3, with ρ_{AMR}, C, and K_{low} as free parameters. The value for ρ_0 in the prefactor C was calculated as $R_{\mathrm{Co}}\,S/L$, with L the length of the strip. Note that a dependence on the DW angle ϕ enters in the model via R_{AMR}. The value of ϕ at each H_x and H_y are described by minimization of (10.2), where H_D and H_K are extracted from the DW depinning data (see Table C.1). The best fit was obtained with parameters $\rho_{\mathrm{AMR}} = 2.9\times10^{-9}\,\Omega\mathrm{m}$, $C = 2.25\times10^{-24}\,\Omega\mathrm{m}^3$, $K_{\mathrm{low}} = 29.8\,\mathrm{kJ/m^3}$. The value of the prefactor C implies via (C.5) that $\rho_\uparrow/\rho_\downarrow \approx 15$, which is reasonable according to the original paper by Levy and Zhang[171]. The value for K_{low} at a dose of 0.50×10^{13} ions/cm^2 is somewhat lower than we measured before in Figure 2.7, which could relate to some of the assumptions in our modeling, such as the chosen values of the fixed parameters or the assumption that the DW width does not depend on in-plane field. Note that we did not have to include additional magnetoresistance effects such as the geometric size effect or the anisotropic interface magnetoresistance[220] to obtain a reasonable fit. The presence of such an effect could alter the fit parameters, but our main conclusion that Bloch walls transform to Néel walls is robust simply because of the very different response to x and y fields, regardless of the precise relative magnitude of the effects that are responsible for the measured changes.

In Figure C.2, we have plotted the various contributions that make up the fitted curves in Figure 10.3(c). The purple solid line indicates the intrinsic DW resistance as a function of in-plane field, which gives the same result for H_x and H_y fields. The dark blue dotted line shows the modeled contribution from the AMR effect under

the influence of H_x fields. The light blue dash-dotted line shows a calculation of what the AMR effect would look like if we would not take into account the magnetization canting: the AMR resistance simply saturates at high H_x. The contribution from AMR as a function of H_y (dashed green curve) is quite small, and reduces at higher in-plane fields since the DW loses its slight Néel character. Note that, since we always measure DWs of both polarities in experiment, the modeled AMR under H_x fields is a superposition of two curves, mutually shifted by the chiral field $\frac{2}{\pi}H_D$.

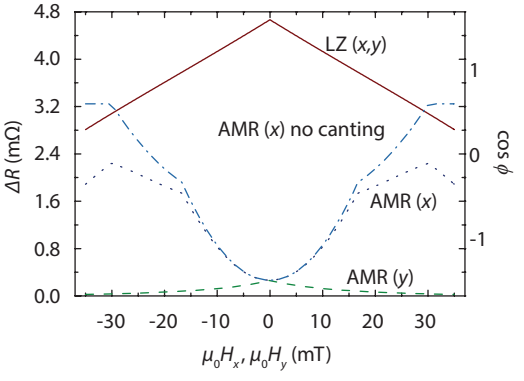

Figure C.2 | Contributions of the various DW resistance effects as a function of in-plane field. Plotted are the intrinsic Levy-Zhang contribution (solid red line), the DW AMR as a function of H_y (dashed green line) and H_x (dotted dark-blue line), and the (hypothetical) DW AMR contribution as a function of H_x in the absence of magnetization canting (dash-dotted light-blue line). The kinks occur when one of the two present DW types reach the Néel state, and there are two of them on both sides because they are shifted in opposite directions by the effective chiral fields.

Summary

Domain walls shift gears
Novel ways to control magnetic domain-wall motion

Magnetic domains are widely used as data storage entities in magnetic hard disk drives. Each individual domain represents one bit, and the domains are separated by transition regions known as domain walls (DWs). For memory and logic devices of the future, it has been proposed to transport information by shifting these DWs through a magnetic nanostrip. This has led to the establishment of a quickly evolving field of research investigating the mechanisms by which DWs can be moved. These mechanisms include the use of an externally applied magnetic field, or sending electric currents through the nanostrips in which the DWs reside. Perpendicularly magnetized materials are particularly interesting for device applications, and new physics is being discovered in these materials since current-driven domain-wall motion exhibits unexpected behavior that cannot be explained by the conventional mechanism of spin-transfer-torque.

This thesis contains several contributions which are right at the heart of recent developments on domain wall physics in perpendicularly magnetized materials such as Pt/Co/Pt and Pt/Co/AlOx. The first part of the thesis focuses on controlling the motion of DWs by introducing well-defined positions where DWs tend to reside after each shifting operation, which is crucial for robust device operation. In particular, it is shown that by irradiating parts of a Pt/Co/Pt nanostrip by a focused ion beam of either Ga or He ions, the perpendicular magnetic anisotropy is altered in such a way that DWs experience a pinning barrier at the edge of the irradiated regions. Furthermore, it is found that the pinning strength is highly tunable by varying both the irradiation dose and the sharpness of the beam. These new insights inspire the proposal and fabrication of a prototype field-driven DW ratchet device, in which multiple DWs can be moved coherently from site to site by applying an AC magnetic field. Furthermore, as a side-step from domain-wall motion, it is shown by micromagnetic simulations that a stationary domain wall pinned at an irradiation barrier exhibits precession when excited by a DC current, which could be used as an efficient nano-scale source of RF signals in integrated circuits. As an alternative to using focused ion beam irradiation for creating pinning sites, the stray magnetic fields of external objects are used, in the form of magnetic nanopillars grown by

electron-beam induced deposition. The pinning strength is found to depend on the height and the magnetic state of the pillar, and this fact is employed to measure the switching field of the nanopillars using the DW dynamics as a probe. Finally, a third DW pinning technique is developed which uses a voltage gate to locally and reversibly alter the anisotropy within a nanostrip, leading to a tunable pinning site at the edge of the gate. This scheme allows the device functionality to be changed even after fabrication is finished, offering an additional degree of freedom in device design.

In the second part of the thesis, the technology of the first part is employed to identify the physical mechanisms responsible for the interaction between DWs and electric current, a topic on which controversial results have been reported in recent years. Firstly, ion irradiation is used to create a well-defined number of DWs in a nanostrip, which allows for a measurement of the intrinsic electrical resistivity that DWs exhibit. It is found that the DW resistivity scales with the inverse square of the DW width, providing experimental evidence of this feature predicted by the Levy-Zhang model. Secondly, the current-assisted DW depinning is studied as a function of applied in-plane field and the symmetry of the material stack. Based on the results, it is concluded that the spin Hall effect arising in the Pt layers is the dominant driving force for DW motion in Pt/Co/Pt, in contrast to the conventional spin-transfer-torque or current-induced Rashba field that was previously asserted. It is found that only DWs of the Néel type can be moved by the spin Hall effect, and the direction of their motion depends on their chirality, set by the applied in-plane field. Finally, it is found that Néel walls of fixed chirality can also occur in the absence of external field, owing to the Dzyaloshinskii-Moriya interaction (DMI) which relates to the stack asymmetry. The strength of the DMI is found to depend strongly on details of the material such as thickness and composition of the capping layer. DW resistance measurements as a function of in-plane field are used as a probe of the internal structure of the DW, and confirm that the combined influence of DMI and spin Hall effect is responsible for the motion of DWs.

Curriculum vitae

Jeroen Franken was born on November 25, 1985 in Roosendaal, the Netherlands. After finishing his gymnasium studies cum laude in 2004 at Norbertuscollege in Roosendaal, he studied Applied Physics at Eindhoven University of Technology. In 2008 he obtained his Bachelor degree cum laude, after performing a final project in the group Theoretical and Polymer Physics under supervision of dr. Paul van der Schoot and dr. Peter Bobbert, where he wrote a Monte Carlo simulation code for nematic interactions on a spherical surface. His focus shifted to experimental physics during his Master studies at the same university, as he carried out an external traineeship in the group of dr. Mathias Kläui at the University of Konstanz on single-shot optical detection of magnetization switching in Permalloy nanostrips. He obtained his Master degree cum laude in 2010 within the group Physics of Nanostructures (FNA). The topic of his Master thesis was domain-wall motion in perpendicularly magnetized ultrathin Pt/CoFeB/Pt films, and this work was carried out under supervision of ir. Reinoud Lavrijsen and prof.dr.ir. Henk Swagten. Afterwards, he continued research in this field by accepting a PhD position in the FNA group, of which the results are presented in this dissertation.

In his free time, Jeroen has been active as a bass player in several bands, playing mostly rock music. He also likes to play squash, to go for a swim, and to play soccer with FNA's futsal team "Spin 'm d'r in". He is also an enthusiastic programmer of websites and other applications.

List of publications

Controlled domain-wall injection in perpendicularly magnetized strips.
R. Lavrijsen, J. H. Franken, J. T. Kohlhepp, H. J. M. Swagten, and B. Koopmans.
*Applied Physics Letters **96**, 222502 (2010)*.

Precise control of domain wall injection and pinning using helium and gallium focused ion beams.
J. H. Franken, M. Hoeijmakers, R. Lavrijsen, J. T. Kohlhepp, H. J. M. Swagten, B. Koopmans, E. van Veldhoven, and D. J. Maas.
*Journal of Applied Physics **109**, 07D504 (2011)*.

Tunable magnetic domain wall oscillator at an anisotropy boundary.
J. H. Franken, R. Lavrijsen, J. T. Kohlhepp, H. J. M. Swagten, and B. Koopmans.
*Applied Physics Letters **98**, 102512 (2011)*.

Domain-wall pinning by local control of anisotropy in Pt/Co/Pt strips.
J. H. Franken, M. Hoeijmakers, R. Lavrijsen, and H. J. M. Swagten.
*Journal of Physics: Condensed Matter **24**, 024216 (2012)*.

Tunable resistivity of individual magnetic domain walls.
J. H. Franken, M. Hoeijmakers, H. J. M. Swagten, and B. Koopmans.
*Physical Review Letters **108**, 037205 (2012)*.

Electric-field control of domain wall motion in perpendicularly magnetized materials.
A. J. Schellekens, A. van den Brink, J. H. Franken, H. J. M. Swagten, and B. Koopmans.
*Nature Communications **3**, 847 (2012)*.

Asymmetric Pt/Co/Pt-stack induced sign-control of current-induced magnetic domain-wall creep.
R. Lavrijsen, P. P. J. Haazen, E. Murè, J. H. Franken, J. T. Kohlhepp, H. J. M. Swagten, and B. Koopmans.
*Applied Physics Letters **100**, 262408 (2012)*.

Shift registers based on magnetic domain wall ratchets with perpendicular anisotropy.
J. H. Franken, H. J. M. Swagten, and B. Koopmans.
*Nature Nanotechnology **7**, 499 (2012)*.

Domain wall depinning governed by the spin Hall effect.
P. P. J. Haazen, E. Murè, J. H. Franken, R. Lavrijsen, H. J. M. Swagten, and B. Koopmans.
*Nature Materials **12**, 299 (2013)*.

Magnetic states in low-pinning high-anisotropy material nanostructures suitable for dynamic imaging.
F. Büttner, C. Moutafis, A. Bisig, P. Wohlhüter, C. M. Günther, J. Mohanty, J. Geilhufe, M. Schneider, C. V. Korff Schmising, S. Schaffert, B. Pfau, M. Hantschmann, M. Riemeier, M. Emmel, S. Finizio, G. Jakob, M. Weigand, J. Rhensius, J. H. Franken, R. Lavrijsen, H. J. M. Swagten, H. Stoll, S. Eisebitt, and M. Kläui.
*Physical Review B **87**, 134422 (2013)*.

Voltage-gated pinning in a magnetic domain-wall conduit.
J. H. Franken, Y. Yin, A. J. Schellekens, A. van den Brink, H. J. M. Swagten, and B. Koopmans.
*Applied Physics Letters **103**, 102411 (2013)*.

Beam-induced Fe nanopillars as tunable domain-wall pinning sites.
J. H. Franken, M. A. J. van der Heijden, T. Ellis, R. Lavrijsen, C. Daniels, D. McGrouther, H. J. M. Swagten, and B. Koopmans.
Accepted for publication in Advanced Functional Materials.

Tunable chiral spin texture in magnetic domain-walls.
J. H. Franken, M. Herps, H. J. M. Swagten, B. Koopmans.
Under review at Nature Communications.

Dankwoord

Een proefschrift wordt ook wel oneerbiedig ‘een nietje door je publicaties’ genoemd. Toch zijn er nog vele, soms nachtelijke, uurtjes nodig gebleken om dit nietje door de stapel papier heen te wurmen. Ik hoop van harte dat het een enigszins begrijpelijk verhaal is geworden, en zo niet, dan op zijn minst een ‘schoon boekske’.

En daarmee kom ik meteen bij de eerste persoon die ik wil bedanken: mijn promotor Henk Swagten. Want zonder jouw fenomenale gevoel voor didactiek en jouw immer constructieve commentaar hadden de teksten in dit boekje nooit dit niveau kunnen bereiken. Ondanks alle drukte wist je altijd tijd vrij te maken voor een goede discussie, zowel met mij als met de studenten. Ook ben ik dankbaar voor de grote mate van vrijheid die je mij geboden hebt, die zich uiteindelijk denk ik zeker uitbetaald heeft. Maar bovenal ben je gewoon een ongelofelijk toffe vent. Al in mijn eerste week als afstudeerder bij FNA was ik getuige van (medeplichtig aan?) feestbeest Henk, die losging in de mochepit tijdens de immer legendarische FOM Veldhoven afterparty. Tel daar de ultrafast dancing dynamics van Bert bij op en ik wist dat ik de juiste vakgroep had gekozen. Maar nog meer waardering heb ik voor jou als begripvolle luisteraar wanneer ik ergens mee zat, zowel binnen het werk als daarbuiten. Bedankt Henk!

Daarnaast was het een groot genoegen om te werken met mijn tweede promotor, bovengenoemde Bert Koopmans. Ik bewonder jouw onvermoeibare positivisme en energie. Altijd vrolijk met een big smile door de gangen struinend, ook al heb je veel te veel werk om handen. Hoe je aan moeilijke zaken, zoals de gedwongen verhuizing uit ons oude gebouw N-laag, altijd een positieve draai weet te geven. Hoe je het altijd weer voor elkaar krijgt om de noodzakelijke financiering binnen te slepen. Daarnaast ben ik altijd weer verwonderd over jouw fysisch inzicht: ook al ben je met 1000 zaken tegelijk bezig, je weet altijd meteen de juiste vragen te stellen en interessante balletjes op te werpen, wat het onderzoek zeker op een hoger plan heeft gebracht.

Voorts had dit boekje niet tot stand kunnen komen zonder het goede werk van de studenten die ik mocht begeleiden bij hun master- of bachelorstage. Mark Hoeijmakers, onze samenwerking heeft naast 3 artikelen de basis gelegd voor veel van het andere werk in dit proefschrift, en het was een waar genoegen met jou samen te werken. Pascal Haazen, je was in alle opzichten extreem: extreem eigenwijs, extreem fanatiek, extreem onnavolgbaar, maar vooral extreem goed, dus

uiteindelijk was je extreem hoge cijfer zeer verdiend. Mark van der Heijden, je bent een zeer prettig persoon om mee samen te werken, en mooi dat ons knotsgekke pilaren experiment een paar jaar na dato toch nog een mooie publicatie heeft opgeleverd. Jan Cortenbach, jij hebt je ontpopt tot een ontzettende doorzetter: volgens mij heeft niemand in de geschiedenis van de groep zo veel samples gegroeid, en uiteindelijk heeft dit ook zeer mooie resultaten opgeleverd. Yuxiang Yin, thanks for your great work, it's an amazing achievement that you got those junctions to work given all the experimental issues. Mark Herps, het was denk ik niet makkelijk als part-timer, met begeleiders die steeds in nieuwe onderwerpen geïnteresseerd raakten; je mag zeer trots zijn dat je al je werk hebt weten te combineren in een imposant verslag.

Verder wil ik alle collega's bij FNA bedanken voor de prettige samenwerking en de gezellige sfeer. In het bijzonder Reinoud Lavrijsen: van jou als afstudeerbegeleider heb ik ontzettend veel geleerd. Ik heb veel bewondering voor jouw just-do-it mentaliteit en de ijzeren vuist waarmee je over het lab heerst. Zonder jouw eerdere werk binnen de groep had dit boekje er heel anders uitgezien. Veel dank ook voor mijn vrolijke roomies, Sjors Schellekens en Feng Zhu: het was gezellig! Verder veel dank voor Karin Jansen, voor het telkens weer regelen van administratieve zaken en het organiseren van vele activiteiten. Ook veel dank voor naamgenoot en technicus Jeroen Francke: als je jou iets vraagt weet je dat het goed geregeld wordt, en petje af voor hoe je de verhuizing in goede banen hebt geleid. Gerrie, bedankt voor het maken van gezellig veel herrie. Beatriz en Wytze, bedankt voor het telkens weer oplappen van het zeer robuuste stukje high-tech dat dual-beam heet... Verder bedank ik alle andere groepsleden die in de loop der jaren bij FNA langs zijn gekomen: Paul, Koen, Matthijs, Arno, Elena, June, Aurelie, Nidhi, Timothy, Wim, Jürgen, Oleg, Jef, Daowei, Francisco, Wiebe, Geerit, Tim, Christian, alle andere studenten, en wie ik verder nog vergeten ben.

Verder wil ik iedereen van andere groepen waarmee ik heb samengewerkt bedanken. Thijs Meijer, bedankt voor de prettige samenwerking. Dank aan Diederik Maas en Emile van Veldhoven voor het zeer geslaagde gebruik van de Helium ionenmicroscoop bij TNO Delft. Thanks to Felix Büttner and Chistoforos Moutafis for the successful collaboration on bubble dynamics. Thanks to Daniel McGrouther for the nice TEM imaging together with our student Carsten. Thanks to the guys at Evico magnetics for the support on their nice Kerr microscope. Dank aan de clean-room staff voor het draaiende houden van alle apparatuur.

Uiteraard ook veel dank aan mijn vrienden, onder wie paranimfen Jan en Matthijs, voor alle gezellige momenten die het leven leuk maken. Bedankt ook mijn lieve familie, pa, ma, Carlijn, Erik, Laura, en hun aangetrouwd en kroost voor al hun steun en interesse. Een speciaal woord van dank voor mijn neefje Julien, wiens speelgoed ik uit de wieg heb ontvreemd om de kaftfoto te maken (sorry!). En natuurlijk, dank aan mijn lieve Joey voor alle gezellige, grappige, vrolijke en verdrietige momenten die we gedeeld hebben.

Bibliography

[1] G. E. Uhlenbeck and S. Goudsmit, *Spinning electrons and the structure of spectra*, Nature **117**, 264 (1926).

[2] M. Baibich, J. Broto, A. Fert, and F. V. Dau, *Giant magnetoresistance of (001) Fe/(001) Cr magnetic superlattices*, Phys. Rev. Lett. **61**, 2472 (1988).

[3] G. Binasch, P. Grünberg, F. Saurenbach, and W. Zinn, *Enhanced magnetoresistance in layered magnetic structures with antiferromagnetic interlayer exchange*, Phys. Rev. B **39**, 4828 (1989).

[4] L. Berger, *Exchange interaction between ferromagnetic domain wall and electric current in very thin metallic films*, J. Appl. Phys. **55**, 1954 (1984).

[5] L. Berger, *Emission of spin waves by a magnetic multilayer traversed by a current*, Phys. Rev. B **54**, 9353 (1996).

[6] J. Slonczewski, *Current-driven excitation of magnetic multilayers*, J. Magn. Magn. Mater. **159**, L1 (1996).

[7] S. S. P. Parkin, M. Hayashi, and L. Thomas, *Magnetic domain-wall racetrack memory*, Science **320**, 190 (2008).

[8] M. Kläui, *Head-to-head domain walls in magnetic nanostructures*, J. Phys. Condens. Matter **20**, 313001 (2008).

[9] S. Zhang and Z. Li, *Roles of Nonequilibrium Conduction Electrons on the Magnetization Dynamics of Ferromagnets*, Phys. Rev. Lett. **93**, 127204 (2004).

[10] A. Thiaville, Y. Nakatani, J. Miltat, and Y. Suzuki, *Micromagnetic understanding of current-driven domain wall motion in patterned nanowires*, Europhys. Lett. **69**, 990 (2005).

[11] J. Grollier, P. Boulenc, V. Cros, A. Hamzic, A. Vaurès, A. Fert, and G. Faini, *Switching a spin valve back and forth by current-induced domain wall motion*, Appl. Phys. Lett. **83**, 509 (2003).

[12] M. Kläui, C. A. F. Vaz, J. A. C. Bland, W. Wernsdorfer, G. Faini, E. Cambril, and L. J. Heyderman, *Domain wall motion induced by spin polarized currents in ferromagnetic ring structures*, Appl. Phys. Lett. **83**, 105 (2003).

[13] N. Vernier, D. A. Allwood, D. Atkinson, M. D. Cooke, and R. P. Cowburn, *Domain wall propagation in magnetic nanowires by spin-polarized current injection*, Europhys. Lett. **65**, 526 (2004).

[14] A. Yamaguchi, T. Ono, S. Nasu, K. Miyake, K. Mibu, and T. Shinjo, *Real-Space Observation of Current-Driven Domain Wall Motion in Submicron Magnetic Wires*, Phys. Rev. Lett. **92**, 077205 (2004).

[15] C. K. Lim, T. Devolder, C. Chappert, J. Grollier, V. Cros, A. Vaurès, A. Fert, and G. Faini, *Domain wall displacement induced by subnanosecond pulsed current*, Appl. Phys. Lett. **84**, 2820 (2004).

[16] M. Kläui, P.-O. Jubert, R. Allenspach, A. Bischof, J. A. C. Bland, G. Faini, U. Rüdiger, C. A. F. Vaz, L. Vila, and C. Vouille, *Direct Observation of Domain-Wall Configurations Transformed by Spin Currents*, Phys. Rev. Lett. **95**, 026601 (2005).

[17] S. E. Barnes and S. Maekawa, *Current-Spin Coupling for Ferromagnetic Domain Walls in Fine Wires*, Phys. Rev. Lett. **95**, 107204 (2005).

[18] G. Meier, M. Bolte, R. Eiselt, B. Krüger, D.-H. Kim, and P. Fischer, *Direct Imaging of Stochastic Domain-Wall Motion Driven by Nanosecond Current Pulses*, Phys. Rev. Lett. **98**, 187202 (2007).

[19] G. Beach, *Current-induced domain wall motion*, J. Magn. Magn. Mater. **320**, 1272 (2008).

[20] M. Hayashi, L. Thomas, R. Moriya, C. Rettner, and S. S. P. Parkin, *Current-controlled magnetic domain-wall nanowire shift register*, Science **320**, 209 (2008).

[21] P. Warin, R. Hyndman, J. Gierak, J. N. Chapman, J. Ferré, J. P. Jamet, V. Mathet, and C. Chappert, *Modification of Co/Pt multilayers by gallium irradiation. Part 2: The effect of patterning using a highly focused ion beam*, J. Appl. Phys. **90**, 3850 (2001).

[22] A. Aziz, S. J. Bending, H. Roberts, S. Crampin, P. J. Heard, and C. H. Marrows, *Artificial domain structures realized by local gallium focused Ion-beam modification of Pt/Co/Pt trilayer transport structure*, J. Appl. Phys. **98**, 124102 (2005).

[23] A. Aziz, S. J. Bending, H. G. Roberts, S. Crampin, P. J. Heard, and C. H. Marrows, *Angular Dependence of Domain Wall Resistivity in Artificial Magnetic Domain Structures*, Phys. Rev. Lett. **97**, 206602 (2006).

[24] R. Lavrijsen, J. H. Franken, J. T. Kohlhepp, H. J. M. Swagten, and B. Koopmans, *Controlled domain-wall injection in perpendicularly magnetized strips*, Appl. Phys. Lett. **96**, 222502 (2010).

[25] O. Boulle, G. Malinowski, and M. Kläui, *Current-induced domain wall motion in nanoscale ferromagnetic elements*, Mat. Sci. Eng. R **72**, 159 (2011).

[26] T. A. Moore, I. M. Miron, G. Gaudin, G. Serret, S. Auffret, B. Rodmacq, A. Schuhl, S. Pizzini, J. Vogel, and M. Bonfim, *High domain wall velocities induced by current in ultrathin Pt/Co/AlOx wires with perpendicular magnetic anisotropy*, Appl. Phys. Lett. **93**, 262504 (2008).

[27] T. A. Moore, I. M. Miron, G. Gaudin, G. Serret, S. Auffret, B. Rodmacq, A. Schuhl, S. Pizzini, J. Vogel, and M. Bonfim, *Erratum: "High domain wall velocities induced by current in ultrathin Pt/Co/AlOx wires with perpendicular magnetic anisotropy"*, Appl. Phys. Lett. **95**, 179902 (2009).

[28] R. Lavrijsen, *Another Spin in The Wall*, Ph.D. thesis, Eindhoven University of Technology (2010).

[29] R. Lavrijsen, P. P. J. Haazen, E. Murè, J. H. Franken, J. T. Kohlhepp, H. J. M. Swagten, and B. Koopmans, *Asymmetric Pt/Co/Pt-stack induced sign-control of current-induced magnetic domain-wall creep*, Appl. Phys. Lett. **100**, 262408 (2012).

[30] I. M. Miron, T. A. Moore, H. Szambolics, L. D. Buda-Prejbeanu, S. Auffret, B. Rodmacq, S. Pizzini, J. Vogel, M. Bonfim, A. Schuhl, et al., *Fast current-induced domain-wall motion controlled by the Rashba effect*, Nat. Mater. **10**, 419 (2011).

[31] L. Liu, O. Lee, T. Gudmundsen, D. Ralph, and R. Buhrman, *Current-Induced Switching of Perpendicularly Magnetized Magnetic Layers Using Spin Torque from the Spin Hall Effect*, Phys. Rev. Lett. **109**, 096602 (2012).

[32] I. Žutić and S. Das Sarma, *Spintronics: Fundamentals and applications*, Rev. Mod. Phys. **76**, 323 (2004).

[33] P. Xu, K. Xia, C. Gu, L. Tang, H. Yang, and J. Li, *An all-metallic logic gate based on current-driven domain wall motion*, Nat. Nanotech. **3**, 97 (2008).

[34] M. Hayashi, L. Thomas, C. Rettner, R. Moriya, and S. S. P. Parkin, *Direct observation of the coherent precession of magnetic domain walls propagating along permalloy nanowires*, Nat. Phys. **3**, 21 (2006).

[35] D. A. Allwood, G. Xiong, M. D. Cooke, C. C. Faulkner, D. Atkinson, N. Vernier, and R. P. Cowburn, *Submicrometer ferromagnetic NOT gate and shift register*, Science **296**, 2003 (2002).

[36] D. Atkinson, D. A. Allwood, G. Xiong, M. D. Cooke, C. C. Faulkner, and R. P. Cowburn, *Magnetic domain-wall dynamics in a submicrometre ferromagnetic structure*, Nat. Mater. **2**, 85 (2003).

[37] K. Shigeto, T. Shinjo, and T. Ono, *Injection of a magnetic domain wall into a submicron magnetic wire*, Appl. Phys. Lett. **75**, 2815 (1999).

[38] L. Thomas, C. Rettner, M. Hayashi, M. G. Samant, S. S. P. Parkin, A. Doran, and A. Scholl, *Observation of injection and pinning of domain walls in magnetic nanowires using photoemission electron microscopy*, Appl. Phys. Lett. **87**, 262501 (2005).

[39] L. San Emeterio Alvarez, K.-Y. Wang, S. Lepadatu, S. Landi, S. J. Bending, and C. H. Marrows, *Spin-Transfer-Torque-Assisted Domain-Wall Creep in a Co/Pt Multilayer Wire*, Phys. Rev. Lett. **104**, 137205 (2010).

[40] C. Burrowes, A. P. Mihai, D. Ravelosona, J. Kim, C. Chappert, L. Vila, A. Marty, Y. Samson, F. Garcia-Sanchez, L. D. Buda-Prejbeanu, et al., *Non-adiabatic spin-torques in narrow magnetic domain walls*, Nat. Phys. **6**, 17 (2010).

[41] O. Boulle, J. Kimling, P. Warnicke, M. Kläui, U. Rüdiger, G. Malinowski, H. J. M. Swagten, B. Koopmans, C. Ulysse, and G. Faini, *Nonadiabatic Spin Transfer Torque in High Anisotropy Magnetic Nanowires with Narrow Domain Walls*, Phys. Rev. Lett. **101**, 216601 (2008).

[42] D. Ravelosona, D. Lacour, J. A. Katine, B. D. Terris, and C. Chappert, *Nanometer scale observation of high efficiency thermally assisted current-driven domain wall depinning*, Phys. Rev. Lett. **95**, 117203 (2005).

[43] J. Fassbender and J. McCord, *Magnetic patterning by means of ion irradiation and implantation*, J. Magn. Magn. Mater. **320**, 579 (2008).

[44] R. Hyndman, P. Warin, J. Gierak, J. Ferré, J. N. Chapman, J. P. Jamet, V. Mathet, and C. Chappert, *Modification of Co/Pt multilayers by gallium irradiation. Part 1: The effect on structural and magnetic properties*, J. Appl. Phys. **90**, 3843 (2001).

[45] C. Chappert, H. Bernas, J. Ferré, V. Kottler, J.-P. Jamet, Y. Chen, E. Cambril, T. Devolder, F. Rousseaux, V. Mathet, et al., *Planar Patterned Magnetic Media Obtained by Ion Irradiation*, Science **280**, 1919 (1998).

[46] T. Devolder, *Light ion irradiation of Co/Pt systems: Structural origin of the decrease in magnetic anisotropy*, Phys. Rev. B **62**, 5794 (2000).

[47] T. Devolder, J. Ferré, C. Chappert, H. Bernas, J.-P. Jamet, and V. Mathet, *Magnetic properties of He-irradiated Pt/Co/Pt ultrathin films*, Phys. Rev. B **64**, 1 (2001).

[48] C. Vieu, J. Gierak, H. Launois, T. Aign, P. Meyer, J. P. Jamet, J. Ferré, C. Chappert, T. Devolder, V. Mathet, et al., *Modifications of magnetic properties of Pt/Co/Pt thin layers by focused gallium ion beam irradiation*, J. Appl. Phys. **91**, 3103 (2002).

[49] J. H. Franken, M. Hoeijmakers, R. Lavrijsen, J. T. Kohlhepp, H. J. M. Swagten, B. Koopmans, E. van Veldhoven, and D. J. Maas, *Precise control of domain wall injection and pinning using helium and gallium focused ion beams*, J. Appl. Phys. **109**, 07D504 (2011).

[50] A. Hubert and R. Schäfer, *Magnetic Domains* (Springer, 1998).

[51] A. Aharoni, *Demagnetizing factors for rectangular ferromagnetic prisms*, J. Appl. Phys. **83**, 3432 (1998).

[52] A. Mougin, M. Cormier, J. P. Adam, P. J. Metaxas, and J. Ferré, *Domain wall mobility, stability and Walker breakdown in magnetic nanowires*, Europhys. Lett. **78**, 57007 (2007).

[53] M. T. Johnson, P. J. H. Bloemen, F. J. A. den Broeder, and J. J. de Vries, *Magnetic anisotropy in metallic multilayers*, Rep. Prog. Phys **59**, 1409 (1996).

[54] J. Stöhr and H. C. Siegmann, *Magnetism, from fundamentals to nanoscale dynamics* (Springer, 2006).

[55] A. P. Malozemoff and J. C. Slonczewski, *Magnetic Domain Walls in Bubble Materials* (Academic Press, 1979).

[56] M. Scheinfein, *LLG micromagnetics simulator*.

[57] E. Fatuzzo, *Theoretical Considerations on the Switching Transient in Ferroelectrics*, Phys. Rev. **127**, 1999 (1962).

[58] Z. Q. Qiu and S. D. Bader, *Surface magneto-optic Kerr effect*, Rev. Sci. Instrum. **71**, 1243 (2000).

[59] R. Schäfer, *Investigation of Domains and Dynamics of Domain Walls by the Magneto-optical Kerr-effect*, Handbook of Magnetism and Advanced Magnetic Materials (2007).

[60] *Evico Magnetics GMBH, http://www.evicomagnetics.de*.

[61] E. C. Stoner and E. P. Wohlfarth, *A Mechanism of Magnetic Hysteresis in Heterogeneous Alloys*, Phil. Trans. Roy. Soc. London. Ser. A, Math. Phys. Sc. **240**, 599 (1948).

[62] D. P. Rosenblatt, M. Karpovski, and A. Gerber, *Monitoring magnetization reversal and perpendicular anisotropy by the extraordinary Hall effect and anisotropic magnetoresistance.*, J. Appl. Phys. **108**, 043924 (2010).

[63] N. A. Sinitsyn, *Semiclassical theories of the anomalous Hall effect*, J. Phys. Condens. Matter **20**, 023201 (2008).

[64] J. Ferré, *Dynamics of magnetization reversal: from continuous to patterned ferromagnetic films*, Top. Appl. Phys. **83**, 127 (2002).

[65] B. W. Ward, J. A. Notte, and N. P. Economou, *Helium ion microscope: A new tool for nanoscale microscopy and metrology*, J. Vac. Sci. Technol. B **24**, 2871 (2006).

[66] D. Maas, E. van Veldhoven, P. Chen, V. Sidorkin, H. Salemink, E. van Der Drift, and P. Alkemade, *Nanofabrication with a helium ion microscope*, Proc. SPIE **7638**, 763814 (2010).

[67] A. Bisig, L. Heyne, O. Boulle, and M. Kläui, *Tunable steady-state domain wall oscillator with perpendicular magnetic anisotropy*, Appl. Phys. Lett. **95**, 162504 (2009).

[68] J. He and S. Zhang, *Localized steady-state domain wall oscillators*, Appl. Phys. Lett. **90**, 142508 (2007).

[69] T. Ono and Y. Nakatani, *Magnetic Domain Wall Oscillator*, Appl. Phys. Express **1**, 061301 (2008).

[70] D. A. Allwood, G. Xiong, C. C. Faulkner, D. Atkinson, D. Petit, and R. P. Cowburn, *Magnetic domain-wall logic*, Science **309**, 1688 (2005).

[71] N. Hayashi, H. Chang, L. T. Romankiw, and S. Krongelb, *An analysis of a clear-view angelfish bubble-domain shift register*, IEEE Trans. Magn. **8**, 16 (1972).

[72] A. Bobeck, P. Bonyhard, and J. Geusic, *Magnetic bubbles: An emerging new memory technology*, Proc. IEEE **63**, 1176 (1975).

[73] C.-Y. You, I. M. Sung, and B.-K. Joe, *Analytic expression for the temperature of the current-heated nanowire for the current-induced domain wall motion*, Appl. Phys. Lett. **89**, 222513 (2006).

[74] D. A. Allwood, G. Xiong, and R. P. Cowburn, *Domain wall diodes in ferromagnetic planar nanowires*, Appl. Phys. Lett. **85**, 2848 (2004).

[75] A. Himeno, S. Kasai, and T. Ono, *Depinning fields of a magnetic domain wall from asymmetric notches*, J. Appl. Phys. **99**, 08G304 (2006).

[76] M. T. Bryan, T. Schrefl, and D. A. Allwood, *Symmetric and asymmetric domain wall diodes in magnetic nanowires*, Appl. Phys. Lett. **91**, 142502 (2007).

[77] A. Pérez-Junquera, V. Marconi, A. Kolton, L. Álvarez Prado, Y. Souche, A. Alija, M. Vélez, J. Anguita, J. Alameda, J. Martín, et al., *Crossed-Ratchet Effects for Magnetic Domain Wall Motion*, Phys. Rev. Lett. **100**, 037203 (2008).

[78] A. Yamaguchi, T. Kishimoto, and H. Miyajima, *Asymmetric Domain Wall Propagation in a Giant Magnetoresistance-Type Wire with Oscillating Interlayer Exchange Coupling*, Appl. Phys. Express **3**, 093004 (2010).

[79] H.-G. Piao, H.-C. Choi, J.-H. Shim, D.-H. Kim, and C.-Y. You, *Ratchet effect of the domain wall by asymmetric magnetostatic potentials*, Appl. Phys. Lett. **99**, 192512 (2011).

[80] L. O'Brien, D. Petit, E. Lewis, R. Cowburn, D. Read, J. Sampaio, H. Zeng, and A.-V. Jausovec, *Tunable Remote Pinning of Domain Walls in Magnetic Nanowires*, Phys. Rev. Lett. **106**, 087204 (2011).

[81] C.-Y. You, *Another method for domain wall movement by a nonuniform transverse magnetic field*, Appl. Phys. Lett. **92**, 152507 (2008).

[82] J. H. Franken, M. Hoeijmakers, R. Lavrijsen, and H. J. M. Swagten, *Domain-wall pinning by local control of anisotropy in Pt/Co/Pt strips*, J. Phys. Cond. Matter **24**, 024216 (2012).

[83] S. Lemerle, J. Ferré, C. Chappert, V. Mathet, T. Giamarchi, P. Le Doussal, J. F. E, and P. L. Doussal, *Domain Wall Creep in an Ising Ultrathin Magnetic Film*, Phys. Rev. Lett. **80**, 849 (1998).

[84] I. M. Miron, K. Garello, G. Gaudin, P.-J. Zermatten, M. V. Costache, S. Auffret, S. Bandiera, B. Rodmacq, A. Schuhl, and P. Gambardella, *Perpendicular switching of a single ferromagnetic layer induced by in-plane current injection*, Nature **476**, 189 (2011).

[85] L. Liu, C.-F. Pai, Y. Li, H. W. Tseng, D. C. Ralph, and R. A. Buhrman, *Spin-Torque Switching with the Giant Spin Hall Effect of Tantalum*, Science **336**, 555 (2012).

[86] A. J. Schellekens, A. van den Brink, J. H. Franken, H. J. M. Swagten, and B. Koopmans, *Electric-field control of domain wall motion in perpendicularly magnetized materials*, Nat. Commun. **3**, 847 (2012).

[87] A. Ehresmann, D. Lengemann, T. Weis, A. Albrecht, J. Langfahl-Klabes, F. Göllner, and D. Engel, *Asymmetric Magnetization Reversal of Stripe-Patterned Exchange Bias Layer Systems for Controlled Magnetic Particle Transport*, Adv. Mater. **23**, 5568 (2011).

[88] E. Rapoport and G. S. D. Beach, *Dynamics of superparamagnetic microbead transport along magnetic nanotracks by magnetic domain walls*, Appl. Phys. Lett. **100**, 082401 (2012).

[89] P. Metaxas, J. Jamet, A. Mougin, M. Cormier, J. Ferré, V. Baltz, B. Rodmacq, B. Dieny, and R. Stamps, *Creep and Flow Regimes of Magnetic Domain-Wall Motion in Ultrathin Pt/Co/Pt Films with Perpendicular Anisotropy*, Phys. Rev. Lett. **99**, 217208 (2007).

[90] D. Houssameddine, U. Ebels, B. Delaët, B. Rodmacq, I. Firastrau, F. Ponthenier, M. Brunet, C. Thirion, J.-P. Michel, L. Prejbeanu-Buda, et al., *Spin-torque oscillator using a perpendicular polarizer and a planar free layer*, Nat. Mater. **6**, 441 (2007).

[91] M. Tsoi, A. G. M. Jansen, J. Bass, W. C. Chiang, V. Tsoi, and P. Wyder, *Generation and detection of phase-coherent current-driven magnons in magnetic multilayers*, Nature **406**, 46 (2000).

[92] S. I. Kiselev, J. C. Sankey, I. N. Krivorotov, N. C. Emley, R. J. Schoelkopf, R. A. Buhrman, and D. C. Ralph, *Microwave oscillations of a nanomagnet driven by a spin-polarized current*, Nature **425**, 380 (2003).

[93] S. Kaka, M. R. Pufall, W. H. Rippard, T. J. Silva, S. E. Russek, and J. A. Katine, *Mutual phase-locking of microwave spin torque nano-oscillators*, Nature **437**, 389 (2005).

[94] E. Saitoh, H. Miyajima, T. Yamaoka, and G. Tatara, *Current-induced resonance and mass determination of a single magnetic domain wall*, Nature **432**, 203 (2004).

[95] L. Thomas, M. Hayashi, X. Jiang, R. Moriya, C. Rettner, and S. Parkin, *Resonant amplification of magnetic domain-wall motion by a train of current pulses*, Science **315**, 1553 (2007).

[96] D. Bedau, M. Kläui, S. Krzyk, U. Rüdiger, G. Faini, and L. Vila, *Detection of Current-Induced Resonance of Geometrically Confined Domain Walls*, Phys. Rev. Lett. **99**, 5 (2007).

[97] S. Lepadatu, O. Wessely, A. Vanhaverbeke, R. Allenspach, A. Potenza, H. Marchetto, T. R. Charlton, S. Langridge, S. S. Dhesi, and C. H. Marrows, *Domain-wall spin-torque resonators for frequency-selective operation*, Phys. Rev. B **81**, 6 (2010).

[98] S.-W. Jung, W. Kim, T.-D. Lee, K.-J. Lee, and H.-W. Lee, *Current-induced domain wall motion in a nanowire with perpendicular magnetic anisotropy*, Appl. Phys. Lett. **92**, 202508 (2008).

[99] P. Carcia, *Ar-sputtered Pt/Co multilayers with large anisotropy energy and coercivity*, IEEE Trans. Magn. **30**, 4395 (1994).

[100] A. Rajanikanth, S. Kasai, N. Ohshima, and K. Hono, *Spin polarization of currents in Co/Pt multilayer and Co-Pt alloy thin films*, Appl. Phys. Lett. **97**, 022505 (2010).

[101] D. Houssameddine, S. H. Florez, J. A. Katine, J.-P. Michel, U. Ebels, D. Mauri, O. Ozatay, B. Delaet, B. Viala, L. Folks, et al., *Spin transfer induced coherent microwave emission with large power from nanoscale MgO tunnel junctions*, Appl. Phys. Lett. **93**, 022505 (2008).

[102] M. K. Niranjan, C.-G. Duan, S. S. Jaswal, and E. Y. Tsymbal, *Electric field effect on magnetization at the Fe/MgO(001) interface*, Appl. Phys. Lett. **96**, 222504 (2010).

[103] F. Bonell, S. Murakami, Y. Shiota, T. Nozaki, T. Shinjo, and Y. Suzuki, *Large change in perpendicular magnetic anisotropy induced by an electric field in FePd ultrathin films*, Appl. Phys. Lett. **98**, 232510 (2011).

[104] Y. Shiota, S. Murakami, F. Bonell, T. Nozaki, T. Shinjo, and Y. Suzuki, *Quantitative Evaluation of Voltage-Induced Magnetic Anisotropy Change by Magnetoresistance Measurement*, Appl. Phys. Express **4**, 043005 (2011).

[105] M. Endo, S. Kanai, S. Ikeda, F. Matsukura, and H. Ohno, *Electric-field effects on thickness dependent magnetic anisotropy of sputtered MgO/Co40Fe40B20/Ta structures*, Appl. Phys. Lett. **96**, 212503 (2010).

[106] T. Maruyama, Y. Shiota, T. Nozaki, K. Ohta, N. Toda, M. Mizuguchi, A. A. Tulapurkar, T. Shinjo, M. Shiraishi, S. Mizukami, et al., *Large voltage-induced magnetic anisotropy change in a few atomic layers of iron*, Nat. Nanotech. **4**, 158 (2009).

[107] T. Nozaki, Y. Shiota, M. Shiraishi, T. Shinjo, and Y. Suzuki, *Voltage-induced perpendicular magnetic anisotropy change in magnetic tunnel junctions*, Appl. Phys. Lett. **96**, 022506 (2010).

[108] S.-S. Ha, N.-H. Kim, S. Lee, C.-Y. You, Y. Shiota, T. Maruyama, T. Nozaki, and Y. Suzuki, *Voltage induced magnetic anisotropy change in ultrathin Fe80Co20/MgO junctions with Brillouin light scattering*, Appl. Phys. Lett. **96**, 142512 (2010).

[109] M. Weisheit, S. Fähler, A. Marty, Y. Souche, C. Poinsignon, and D. Givord, *Electric field-induced modification of magnetism in thin-film ferromagnets*, Science **315**, 349 (2007).

[110] C. Fowley, K. Rode, K. Oguz, H. Kurt, and J. M. D. Coey, *Electric field induced changes in the coercivity of a thin-film ferromagnet*, J. Phys. D Appl. Phys. **44**, 305001 (2011).

[111] T. Seki, M. Kohda, J. Nitta, and K. Takanashi, *Coercivity change in an FePt thin layer in a Hall device by voltage application*, Appl. Phys. Lett. **98**, 212505 (2011).

[112] H. Ohno, D. Chiba, F. Matsukura, T. Omiya, E. Abe, T. Dietl, Y. Ohno, and K. Ohtani, *Electric-field control of ferromagnetism*, Nature **408**, 944 (2000).

[113] M. Zhernenkov, M. R. Fitzsimmons, J. Chlistunoff, J. Majewski, I. Tudosa, and E. E. Fullerton, *Electric-field modification of magnetism in a thin CoPd film*, Phys. Rev. B **82**, 024420 (2010).

[114] D. Chiba, S. Fukami, K. Shimamura, N. Ishiwata, K. Kobayashi, and T. Ono, *Electrical control of the ferromagnetic phase transition in cobalt at room temperature*, Nat. Mater. **10**, 853 (2011).

[115] Y. Shiota, T. Nozaki, F. Bonell, S. Murakami, T. Shinjo, and Y. Suzuki, *Induction of coherent magnetization switching in a few atomic layers of FeCo using voltage pulses*, Nat. Mater. **11**, 39 (2011).

[116] W.-G. Wang, M. Li, S. Hageman, and C. L. Chien, *Electric-field-assisted switching in magnetic tunnel junctions*, Nat. Mater. **11**, 64 (2011).

[117] L. Liu, C.-F. Pai, D. C. Ralph, and R. A. Buhrman, *Gate voltage modulation of spin-Hall-torque-driven magnetic switching*, arxiv **1209.0962** (2012).

[118] J. Dean, M. T. Bryan, T. Schrefl, and D. A. Allwood, *Stress-based control of magnetic nanowire domain walls in artificial multiferroic systems*, J. Appl. Phys. **109**, 023915 (2011).

[119] T.-K. Chung, G. P. Carman, and K. P. Mohanchandra, *Reversible magnetic domain-wall motion under an electric field in a magnetoelectric thin film*, Appl. Phys. Lett. **92**, 112509 (2008).

[120] T. H. E. Lahtinen, K. J. A. Franke, and S. van Dijken, *Electric-field control of magnetic domain wall motion and local magnetization reversal*, Sci. Rep. **2**, 258 (2012).

[121] D. Chiba, M. Kawaguchi, S. Fukami, N. Ishiwata, K. Shimamura, K. Kobayashi, and T. Ono, *Electric-field control of magnetic domain-wall velocity in ultrathin cobalt with perpendicular magnetization*, Nat. Commun. **3**, 888 (2012).

[122] U. Bauer, S. Emori, and G. S. D. Beach, *Voltage-gated modulation of domain wall creep dynamics in an ultrathin metallic ferromagnet*, Appl. Phys. Lett. **101**, 172403 (2012).

[123] U. Bauer, S. Emori, and G. S. D. Beach, *Electric field control of domain wall propagation in Pt/Co/GdOx films*, Appl. Phys. Lett. **100**, 192408 (2012).

[124] A. Bernand-Mantel, L. Herrera-Diez, L. Ranno, S. Pizzini, J. Vogel, D. Givord, S. Auffret, O. Boulle, I. M. Miron, and G. Gaudin, *Electric-field control of domain wall nucleation and pinning in a metallic ferromagnet*, Appl. Phys. Lett. **102**, 122406 (2013).

[125] U. Bauer, M. Przybylski, J. Kirschner, and G. S. D. Beach, *Magnetoelectric charge trap memory*, Nano Lett. **12**, 1437 (2012).

[126] U. Bauer, S. Emori, and G. S. D. Beach, *Voltage-controlled domain wall traps in ferromagnetic nanowires*, Nat. Nanotech. **8**, 411 (2013).

[127] J. H. Franken, H. J. M. Swagten, and B. Koopmans, *Shift registers based on magnetic domain wall ratchets with perpendicular anisotropy*, Nat. Nanotech. **7**, 499 (2012).

[128] A. Manchon, C. Ducruet, L. Lombard, S. Auffret, B. Rodmacq, B. Dieny, S. Pizzini, J. Vogel, V. Uhlir, M. Hochstrasser, et al., *Analysis of oxygen induced anisotropy crossover in Pt/Co/MOx trilayers*, J. Appl. Phys. **104**, 043914 (2008).

[129] J. Kimling, T. Gerhardt, A. Kobs, A. Vogel, S. Wintz, M.-Y. Im, P. Fischer, H. Peter Oepen, U. Merkt, and G. Meier, *Tuning of the nucleation field in nanowires with perpendicular magnetic anisotropy*, J. Appl. Phys. **113**, 163902 (2013).

[130] X. Jiang, L. Thomas, R. Moriya, and S. S. P. Parkin, *Discrete domain wall positioning due to pinning in current driven motion along nanowires*, Nano Lett. **11**, 96 (2011).

[131] M. A. Bruk, E. N. Zhikharev, E. I. Grigor'ev, A. V. Spirin, V. A. Kal'nov, and I. E. Kardash, *Focused electron beam-induced deposition of iron- and carbon-containing nanostructures from triiron dodecacarbonyl vapor*, High Energy Chem. **39**, 65 (2005).

[132] A. Fernández-Pacheco, L. Serrano-Ramón, J. M. Michalik, M. R. Ibarra, J. M. De Teresa, L. O'Brien, D. Petit, J. Lee, and R. P. Cowburn, *Three dimensional magnetic nanowires grown by focused electron-beam induced deposition*, Sci. Rep. **3**, 1492 (2013).

[133] R. R. Kunz and T. M. Mayer, *Catalytic growth rate enhancement of electron beam deposited iron films*, Appl. Phys. Lett. **50**, 962 (1987).

[134] M. Takeguchi, M. Shimojo, K. Mitsuishi, M. Tanaka, R. Che, and K. Furuya, *Fabrication of nanostructures with different iron concentration by electron beam induced deposition with a mixture gas of iron carbonyl and ferrocene, and their magnetic properties*, J. Mater. Sci. **41**, 4532 (2006).

[135] I. Utke, P. Hoffmann, and J. Melngailis, *Gas-assisted focused electron beam and ion beam processing and fabrication*, J. Vac. Sci. Technol. B **26**, 1197 (2008).

[136] A. Fernández-Pacheco, J. M. De Teresa, R. Córdoba, M. R. Ibarra, D. Petit, D. E. Read, L. O'Brien, E. R. Lewis, H. T. Zeng, and R. P. Cowburn, *Domain wall conduit behavior in cobalt nanowires grown by focused electron beam induced deposition*, Appl. Phys. Lett. **94**, 192509 (2009).

[137] M. Takeguchi, M. Shimojo, R. Che, and K. Furuya, *Fabrication of a nano-magnet on a piezo-driven tip in a TEM sample holder*, J. Mater. Sci. **41**, 2627 (2006).

[138] W. F. van Dorp, B. van Someren, C. W. Hagen, P. Kruit, and P. A. Crozier, *Approaching the resolution limit of nanometer-scale electron beam-induced deposition*, Nano Lett. **5**, 1303 (2005).

[139] M. Takeguchi, M. Shimojo, and K. Furuya, *Fabrication of magnetic nanostructures using electron beam induced chemical vapour deposition*, Nanotechnology **16**, 1321 (2005).

[140] M. Gavagnin, H. D. Wanzenboeck, D. Belić, and E. Bertagnolli, *Synthesis of*, ACS Nano **7**, 777 (2013).

[141] W. Zhang, M. Shimojo, M. Takeguchi, R.-C. Che, and K. Furuya, *Generation Mechanism andin situ Growth Behavior of α-Iron Nanocrystals by Electron Beam Induced Deposition*, Adv. Eng. Mater. **8**, 711 (2006).

[142] W. F. van Dorp and C. W. Hagen, *A critical literature review of focused electron beam induced deposition*, J. Appl. Phys. **104**, 081301 (2008).

[143] M. T. Bryan, J. Dean, T. Schrefl, F. E. Thompson, J. Haycock, and D. A. Allwood, *The effect of trapping superparamagnetic beads on domain wall motion*, Appl. Phys. Lett. **96**, 192503 (2010).
[144] M. Donolato, M. Gobbi, P. Vavassori, M. Leone, M. Cantoni, V. Metlushko, B. Ilic, M. Zhang, S. X. Wang, and R. Bertacco, *Nanosized corners for trapping and detecting magnetic nanoparticles.*, Nanotechnology **20**, 385501 (2009).
[145] E. Rapoport, D. Montana, and G. S. D. Beach, *Integrated capture, transport, and magneto-mechanical resonant sensing of superparamagnetic microbeads using magnetic domain walls.*, Lab Chip **12**, 4433 (2012).
[146] P. Vavassori, V. Metlushko, B. Ilic, M. Gobbi, M. Donolato, M. Cantoni, and R. Bertacco, *Domain wall displacement in Py square ring for single nanometric magnetic bead detection*, Appl. Phys. Lett. **93**, 203502 (2008).
[147] R. Lavrijsen, R. Córdoba, F. J. Schoenaker, T. H. Ellis, B. Barcones, J. T. Kohlhepp, H. J. M. Swagten, B. Koopmans, J. M. De Teresa, C. Magén, et al., *Fe:O:C grown by focused-electron-beam-induced deposition: magnetic and electric properties*, Nanotechnology **22**, 025302 (2011).
[148] R. Córdoba, R. Lavrijsen, A. Fernández-Pacheco, M. R. Ibarra, F. Schoenaker, T. Ellis, B. Barcones-Campo, J. T. Kohlhepp, H. J. M. Swagten, B. Koopmans, et al., *Giant anomalous Hall effect in Fe-based microwires grown by focused-electron-beam-induced deposition*, J. Phys. D. Appl. Phys. **45**, 035001 (2012).
[149] C. W. Sandweg, N. Wiese, D. McGrouther, S. J. Hermsdoerfer, H. Schultheiss, B. Leven, S. McVitie, B. Hillebrands, and J. N. Chapman, *Direct observation of domain wall structures in curved permalloy wires containing an antinotch*, J. Appl. Phys. **103**, 093906 (2008).
[150] J. Chapman, *The investigation of magnetic domain structures in thin foils by electron microscopy*, J. Phys. D. Appl. Phys. **17**, 623 (1984).
[151] P. J. Metaxas, P.-J. Zermatten, J.-P. Jamet, J. Ferré, G. Gaudin, B. Rodmacq, A. Schuhl, and R. L. Stamps, *Periodic magnetic domain wall pinning in an ultrathin film with perpendicular anisotropy generated by the stray magnetic field of a ferromagnetic nanodot array*, Appl. Phys. Lett. **94**, 132504 (2009).
[152] S.-M. Ahn, K.-W. Moon, C.-G. Cho, and S.-B. Choe, *Control of domain wall pinning in ferromagnetic nanowires by magnetic stray fields*, Nanotechnology **22**, 085201 (2011).
[153] V. L. Mironov, O. L. Ermolaeva, E. V. Skorohodov, and A. Y. Klimov, *Field-controlled domain wall pinning-depinning effects in a ferromagnetic nanowire-nanoislands system*, Phys. Rev. B **85**, 144418 (2012).
[154] M. Vázquez, G. Basheed, G. Infante, and R. Del Real, *Trapping and Injecting Single Domain Walls in Magnetic Wire by Local Fields*, Phys. Rev. Lett. **108**, 037201 (2012).
[155] L. OâĂŹBrien, A. Beguivin, A. Fernandez-Pacheco, D. Petit, D. E. Read, and R. P. Cowburn, *Magnetic domain wall induced, localized nanowire reversal*, Appl. Phys. Lett. **101**, 062415 (2012).
[156] R. I. Joseph, *Ballistic Demagnetizing Factor in Uniformly Magnetized Cylinders*, J. Appl. Phys. **37**, 4639 (1966).
[157] M. Cyrot and E. de Lacheisserie, *Magnetism: Fundamentals* (Springer, 2007).
[158] H.-B. Braun, *Thermally activated Magnetization Reversal in Elongated Ferromagnetic Particles*, Phys. Rev. Lett. **71**, 3557 (1993).
[159] M. Donolato, P. Vavassori, M. Gobbi, M. Deryabina, M. F. Hansen, V. Metlushko, B. Ilic, M. Cantoni, D. Petti, S. Brivio, et al., *On-chip manipulation of protein-coated magnetic beads via domain-wall conduits*, Adv. Mater. **22**, 2706 (2010).
[160] D. L. Graham, H. A. Ferreira, and P. P. Freitas, *Magnetoresistive-based biosensors and biochips*, Trends Biotechnol. **22**, 455 (2004).
[161] S. Wang and G. Li, *Advances in Giant Magnetoresistance Biosensors With Magnetic Nanoparticle Tags: Review and Outlook*, IEEE Trans. Magn. **44**, 1687 (2008).
[162] N. Kikuchi, S. Okamoto, O. Kitakami, Y. Shimada, and K. Fukamichi, *Sensitive detection of irreversible switching in a single FePt nanosized dot*, Appl. Phys. Lett. **82**, 4313 (2003).
[163] G. Tatara, H. Kohno, and J. Shibata, *Theory of Domain Wall Dynamics under Current*, J. Phys. Soc. Japan **77**, 031003 (2008).
[164] N. L. Schryer and L. R. Walker, *The motion of 180 degree domain walls in uniform DC magnetic fields*, J. Appl. Phys. **45**, 5406 (1974).
[165] A. Thiaville and Y. Nakatani, *Domain wall motion by spin-polarized current: a micromagnetic study*, J. Appl. Phys. **95**, 7049 (2004).
[166] G. Tatara and H. Kohno, *Theory of Current-Driven Domain Wall Motion: Spin Transfer versus Momentum Transfer*, Phys. Rev. Lett. **92**, 86601 (2004).

[167] J. Xiao, A. Zangwill, and M. D. Stiles, *Spin-transfer torque for continuously variable magnetization*, Phys. Rev. B **73**, 054428 (2006).
[168] A. Vanhaverbeke and M. Viret, *Simple model of current-induced spin torque in domain walls*, Phys. Rev. B **75**, 024411 (2007).
[169] G. Tatara, H. Kohno, and J. Shibata, *Microscopic approach to current-driven domain wall dynamics*, Phys. Rep. **468**, 213 (2008).
[170] C. H. Marrows, *Spin-polarised currents and magnetic domain walls*, Adv. Phys. **54**, 585 (2005).
[171] P. M. Levy and S. Zhang, *Resistivity due to Domain Wall Scattering*, Phys. Rev. Lett. **79**, 5110 (1997).
[172] I. M. Miron, G. Gaudin, S. Auffret, B. Rodmacq, A. Schuhl, S. Pizzini, J. Vogel, and P. Gambardella, *Current-driven spin torque induced by the Rashba effect in a ferromagnetic metal layer*, Nat. Mater. **9**, 230 (2010).
[173] A. Yu and E. I. Rashba, *Properies of a 2d electron gas with lifted spectral degeneracy*, JETP Lett. **39**, 78 (1984).
[174] A. Manchon, *Spin Hall effect versus Rashba torque: a Diffusive Approach*, arXiv **1204.4869** (2012).
[175] P. P. J. Haazen, *Domain wall motion induced by the spin Hall effect in ultrathin Pt/Co/Pt films*, Master thesis, Eindhoven University of Technology (2012).
[176] X. Wang and A. Manchon, *Diffusive Spin Dynamics in Ferromagnetic Thin Films with a Rashba Interaction*, Phys. Rev. Lett. **108**, 117201 (2012).
[177] E. V. D. Bijl and R. Duine, *Current-induced torques in textured Rashba ferromagnets*, Phys. Rev. B **86**, 094406 (2012).
[178] M. I. Dyakonov and V. I. Perel, *Current-induced spin orientation of electrons in semiconductors*, Phys. Lett. A **35A**, 459 (1971).
[179] M. I. Dyakonov and V. I. Perel, *Possibility of orienting electron spins with current*, JETP Lett. **13**, 467 (1971).
[180] J. Hirsch, *Spin Hall Effect*, Phys. Rev. Lett. **83**, 1834 (1999).
[181] Y. Kato, R. Myers, A. Gossard, and D. Awschalom, *Observation of the spin Hall effect in semiconductors*, Science **306**, 1910 (2004).
[182] J. Wunderlich, B. Kaestner, J. Sinova, and T. Jungwirth, *Experimental Observation of the Spin-Hall Effect in a Two-Dimensional Spin-Orbit Coupled Semiconductor System*, Phys. Rev. Lett. **94**, 047204 (2005).
[183] T. Kimura, Y. Otani, T. Sato, S. Takahashi, and S. Maekawa, *Room-Temperature Reversible Spin Hall Effect*, Phys. Rev. Lett. **98**, 156601 (2007).
[184] L. Vila, T. Kimura, and Y. Otani, *Evolution of the Spin Hall Effect in Pt Nanowires: Size and Temperature Effects*, Phys. Rev. Lett. **99**, 1 (2007).
[185] L. Liu, R. A. Buhrman, and D. C. Ralph, *Review and Analysis of Measurements of the Spin Hall Effect in Platinum*, arXiv **1111.3702** (2011).
[186] C.-F. Pai, L. Liu, Y. Li, H. W. Tseng, D. C. Ralph, and R. A. Buhrman, *Spin transfer torque devices utilizing the giant spin Hall effect of tungsten*, Appl. Phys. Lett. **101**, 122404 (2012).
[187] L. Berger, *Side-jump mechanism for the Hall effect of ferromagnets*, Phys. Rev. B **2**, 4559 (1970).
[188] J. Smit, *The spontaneous Hall effect in ferromagnetics II*, Physica **24**, 39 (1958).
[189] M. Gradhand, D. V. Fedorov, P. Zahn, I. Mertig, Y. Otani, Y. Niimi, L. Vila, and A. Fert, *Perfect Alloys for Spin Hall Current-Induced Magnetization Switching*, Spin **02**, 1250010 (2012).
[190] A. Manchon and S. Zhang, *Theory of nonequilibrium intrinsic spin torque in a single nanomagnet*, Phys. Rev. B **78**, 212405 (2008).
[191] L. Liu, T. Moriyama, D. C. Ralph, and R. A. Buhrman, *Spin-Torque Ferromagnetic Resonance Induced by the Spin Hall Effect*, Phys. Rev. Lett. **106**, 036601 (2011).
[192] K.-W. Kim, S.-M. Seo, J. Ryu, K.-J. Lee, and H.-W. Lee, *Magnetization dynamics induced by in-plane currents in ultrathin magnetic nanostructures with Rashba spin-orbit coupling*, Phys. Rev. B **85**, 180404(R) (2012).
[193] A. V. Khvalkovskiy, V. Cros, D. Apalkov, V. Nikitin, M. Krounbi, K. A. Zvezdin, A. Anane, J. Grollier, and A. Fert, *Matching domain-wall configuration and spin-orbit torques for efficient domain-wall motion*, Phys. Rev. B **87**, 020402 (2013).
[194] M. Stiles and J. Miltat, *Spin-transfer torque and dynamics*, Spin dynamics in confined magnetic structures III, Topics in Applied Physics **101**, 225 (2006).
[195] A. Manchon, *Manipulating the voltage dependence of tunneling spin torques*, arXiv **1207.5231** (2012).

[196] P. Anderson, *Antiferromagnetism. Theory of Superexchange Interaction*, Phys. Rev. **79**, 350 (1950).

[197] I. Dzyaloshinsky, *A thermodynamic theory of 'weak' ferromagnetism of antiferromagnetics*, J. Phys. Chem. Solids **4**, 241 (1958).

[198] T. Moriya, *New mechanism of anisotropic superexchange interaction*, Phys. Rev. Lett. **4**, 228 (1960).

[199] A. Fert, *Magnetic and Transport Properties of Metallic Multilayers*, Mater. Sci. Forum **59-60**, 439 (1990).

[200] M. Bode, M. Heide, K. von Bergmann, P. Ferriani, S. Heinze, G. Bihlmayer, A. Kubetzka, O. Pietzsch, S. Blügel, and R. Wiesendanger, *Chiral magnetic order at surfaces driven by inversion asymmetry*, Nature **447**, 190 (2007).

[201] M. Heide, G. Bihlmayer, and S. Blügel, *Dzyaloshinskii-Moriya interaction accounting for the orientation of magnetic domains in ultrathin films: Fe/W(110)*, Phys. Rev. B **78**, 140403 (2008).

[202] S. Mühlbauer, B. Binz, F. Jonietz, C. Pfleiderer, A. Rosch, A. Neubauer, R. Georgii, and P. Böni, *Skyrmion lattice in a chiral magnet*, Science **323**, 915 (2009).

[203] X. Z. Yu, Y. Onose, N. Kanazawa, J. H. Park, J. H. Han, Y. Matsui, N. Nagaosa, and Y. Tokura, *Real-space observation of a two-dimensional skyrmion crystal*, Nature **465**, 901 (2010).

[204] A. Thiaville, S. Rohart, E. Jué, V. Cros, and A. Fert, *Dynamics of Dzyaloshinskii domain walls in ultrathin magnetic films*, Europhys. Lett. **100**, 57002 (2012).

[205] S. Emori, U. Bauer, S.-M. Ahn, E. Martinez, and G. S. D. Beach, *Current-driven dynamics of chiral ferromagnetic domain walls*, Nat. Mater. **12**, 611 (2013).

[206] K.-S. Ryu, L. Thomas, S.-H. Yang, and S. Parkin, *Chiral spin torque at magnetic domain walls*, Nat. Nanotechnol. **8**, 527 (2013).

[207] T. Koyama, D. Chiba, K. Ueda, K. Kondou, H. Tanigawa, S. Fukami, T. Suzuki, N. Ohshima, N. Ishiwata, Y. Nakatani, et al., *Observation of the intrinsic pinning of a magnetic domain wall in a ferromagnetic nanowire*, Nat. Mater. **10**, 194 (2011).

[208] M. Viret, D. Vignoles, D. Cole, J. M. D. Coey, W. Allen, D. S. Daniel, and J. F. Gregg, *Spin scattering in ferromagnetic thin films*, Phys. Rev. B **53**, 8464 (1996).

[209] D. Ravelosona, A. Cebollada, F. Briones, C. Diaz-Paniagua, M. A. Hidalgo, and F. Batallan, *Domain-wall scattering in epitaxial FePd ordered alloy films with perpendicular magnetic anisotropy*, Phys. Rev. B **59**, 4322 (1999).

[210] M. Viret, Y. Samson, P. Warin, A. Marty, F. Ott, E. Sondergard, O. Klein, and C. Fermon, *Anisotropy of domain wall resistance*, Phys. Rev. Lett. **85**, 3962 (2000).

[211] C. H. Marrows and B. C. Dalton, *Spin Mixing and Spin-Current Asymmetry Measured by Domain Wall Magnetoresistance*, Phys. Rev. Lett. **92**, 097206 (2004).

[212] G. Tatara and H. Fukuyama, *Resistivity due to a Domain Wall in Ferromagnetic Metal*, Phys. Rev. Lett. **78**, 3773 (1997).

[213] R. P. van Gorkom, A. Brataas, and G. E. W. Bauer, *Negative Domain Wall Resistance in Ferromagnets*, Phys. Rev. Lett. **83**, 4401 (1999).

[214] U. Ebels, A. Radulescu, Y. Henry, L. Piraux, and K. Ounadjela, *Spin accumulation and domain wall magnetoresistance in 35 nm Co wires*, Phys. Rev. Lett. **84**, 983 (2000).

[215] E. Šimánek, *Spin accumulation and resistance due to a domain wall*, Phys. Rev. B **63**, 224412 (2001).

[216] M. Cormier, A. Mougin, J. Ferré, A. Thiaville, N. Charpentier, F. Piéchon, R. Weil, V. Baltz, and B. Rodmacq, *Effect of electrical current pulses on domain walls in Pt/Co/Pt nanotracks with out-of-plane anisotropy: Spin transfer torque versus Joule heating*, Phys. Rev. B **81**, 024407 (2010).

[217] R. Danneau, P. Warin, J. P. Attané, I. Petej, C. Beigné, C. Fermon, O. Klein, A. Marty, F. Ott, Y. Samson, et al., *Individual Domain Wall Resistance in Submicron Ferromagnetic Structures*, Phys. Rev. Lett. **88**, 157201 (2002).

[218] P. J. Metaxas, J. P. Jamet, A. Mougin, M. Cormier, J. Ferré, V. Baltz, B. Rodmacq, B. Dieny, and R. L. Stamps, *Creep and Flow Regimes of Magnetic Domain-Wall Motion in Ultrathin Pt/Co/Pt Films with Perpendicular Anisotropy*, Phys. Rev. Lett. **99**, 217208 (2007).

[219] B. A. Lilley, *Energies and widths of domain boundaries in ferromagnetics*, Phil. Mag. **(7)41**, 792 (1950).

[220] A. Kobs, S. Hesse, W. Kreuzpaintner, G. Winkler, D. Lott, P. Weinberger, A. Schreyer, and H. P. Oepen, *Anisotropic Interface Magnetoresistance in Pt/Co/Pt Sandwiches*, Phys. Rev. Lett. **106**, 217207 (2011).

[221] Y. Zhang, W. S. Zhao, D. Ravelosona, J.-O. Klein, J. V. Kim, and C. Chappert, *Perpendicular-magnetic-anisotropy CoFeB racetrack memory*, J. Appl. Phys. **111**, 093925 (2012).
[222] H. Honjo, S. Fukami, T. Suzuki, R. Nebashi, N. Ishiwata, S. Miura, N. Sakimura, T. Sugibayashi, N. Kasai, and H. Ohno, *Domain-wall-motion cell with perpendicular anisotropy wire and in-plane magnetic tunneling junctions*, J. Appl. Phys. **111**, 07C903 (2012).
[223] S. S. P. Parkin, *US Patent 6834005* (2004).
[224] K.-J. Kim, J.-C. Lee, S.-J. Yun, G.-H. Gim, K.-S. Lee, S.-B. Choe, and K.-H. Shin, *Electric Control of Multiple Domain Walls in Pt/Co/Pt Nanotracks with Perpendicular Magnetic Anisotropy*, Appl. Phys. Express **3**, 083001 (2010).
[225] J. Heinen, O. Boulle, K. Rousseau, G. Malinowski, M. Kläui, H. J. M. Swagten, B. Koopmans, C. Ulysse, and G. Faini, *Current-induced domain wall motion in Co/Pt nanowires: Separating spin torque and Oersted-field effects*, Appl. Phys. Lett. **96**, 202510 (2010).
[226] I. M. Miron, P.-J. Zermatten, G. Gaudin, S. Auffret, B. Rodmacq, and A. Schuhl, *Domain Wall Spin Torquemeter*, Phys. Rev. Lett. **102**, 137202 (2009).
[227] M. I. Dyakonov and V. I. Perel, *Current-induced spin orientation of electrons in semiconductors*, Phys. Lett. A **35**, 459 (1971).
[228] V. E. Demidov, S. Urazhdin, E. R. J. Edwards, and S. O. Demokritov, *Wide-range control of ferromagnetic resonance by spin Hall effect*, Appl. Phys. Lett. **99**, 172501 (2011).
[229] Y. Kajiwara, K. Harii, S. Takahashi, J. Ohe, K. Uchida, M. Mizuguchi, H. Umezawa, H. Kawai, K. Ando, K. Takanashi, et al., *Transmission of electrical signals by spin-wave interconversion in a magnetic insulator*, Nature **464**, 262 (2010).
[230] S.-M. Seo, K.-W. Kim, J. Ryu, H.-W. Lee, and K.-J. Lee, *Current-induced motion of a transverse magnetic domain wall in the presence of spin Hall effect*, Appl. Phys. Lett. **101**, 022405 (2012).
[231] S.-G. Je, D.-H. Kim, S.-C. Yoo, B.-C. Min, K.-J. Lee, and S.-B. Choe, *Asymmetric magnetic domain-wall motion by the Dzyaloshinskii-Moriya interaction*, Phys. Rev. B **88**, 214401 (2013).
[232] K. Garello, I. M. Miron, C. O. Avci, F. Freimuth, Y. Mokrousov, S. Blügel, S. Auffret, O. Boulle, G. Gaudin, and P. Gambardella, *Symmetry and magnitude of spin-orbit torques in ferromagnetic heterostructures*, Nat. Nanotechnol. **8**, 587 (2013).
[233] P. P. J. Haazen, E. Murè, J. H. Franken, R. Lavrijsen, H. J. M. Swagten, and B. Koopmans, *Domain wall depinning governed by the spin Hall effect*, Nat. Mater. **12**, 299 (2013).
[234] T. Koyama, H. Hata, K.-J. Kim, T. Moriyama, H. Tanigawa, T. Suzuki, Y. Nakatani, D. Chiba, and T. Ono, *Current-Induced Magnetic Domain Wall Motion in a Co/Ni Nanowire with Structural Inversion Asymmetry*, Appl. Phys. Express **6**, 033001 (2013).
[235] S. Emori, E. Martinez, and U. Bauer, *Spin Hall torque magnetometry of Dzyaloshinskii domain walls*, arXiv **1308.1432** (2013).
[236] J. Torrejon, J. Kim, J. Sinha, M. Yamanouchi, S. Mitani, M. Hayashi, and H. Ohno, *Interface control of the magnetic chirality in TaN|CoFeB|MgO heterosctructures*, arXiv **1308.1751** (2013).
[237] G. Chen, J. Zhu, A. Quesada, J. Li, A. T. N'Diaye, Y. Huo, T. P. Ma, Y. Chen, H. Y. Kwon, C. Won, et al., *Novel Chiral Magnetic Domain Wall Structure in Fe/Ni/Cu(001) Films*, Phys. Rev. Lett. **110**, 177204 (2013).
[238] J. H. Franken, M. Hoeijmakers, H. J. M. Swagten, and B. Koopmans, *Tunable Resistivity of Individual Magnetic Domain Walls*, Phys. Rev. Lett. **108**, 037205 (2012).
[239] F. Freimuth, S. Blügel, and Y. Mokrousov, *Berry phase theory of Dzyaloshinskii-Moriya interaction and spin-orbit torques*, arXiv **1308.5983** (2013).
[240] S. Bandiera, R. R. Sousa, B. B. Rodmacq, and B. Dieny, *Asymmetric Interfacial Perpendicular Magnetic Anisotropy in Pt/Co/Pt Trilayers*, IEEE Magn. Lett. **2**, 3000504 (2011).
[241] A. Fert, V. Cros, and J. Sampaio, *Skyrmions on the track*, Nat. Nanotechnol. **8**, 152 (2013).
[242] D. B. Montgomery and J. Terrell, *Some useful information for the design of air-core solenoids*, Air Force Contract AF **19**, 7344 (1961).